Thèse présentée en vue de l'obtention du diplôme de

Doctorat en sciences en : Physique

Option : physique des matériaux

THEME

Mécanismes de croissance de nanostructures à base du sulfure de nickel pour les supercondensateurs

Présenté Par : Abd Elouahab GAHTAR

SOUTENU LE: 18 / 02 / 2021

Devant le jury composé de :

Dr. Saïd LAKEL	**Prof**	**Univ. Mohamed KHIDER- Biskra**	**Président**
Dr. Said BENRAMACH	**Prof**	**Univ. Mohamed KHIDER- Biskra**	**Rapporteur**
Dr. Miloud IBRIR	**Prof**	**Univ. Mohamed BOUDIAF- M'sila**	**Examinateur**
Dr. Mohammed El Hadi ATTIA	**M.C.A**	**Univ. Hamma LAKHDAR- El Oued**	**Examinateur**

Année universitaire 2020-2021

<u>Acknowledgements</u>

Imagination is more important than knowledge. Knowledge is limited. Imagination encircles the world [Albert Einstein].

<u>Dedications</u>

I dedicate this work as a sign of respect and appreciation:

To my dear father and mother for their affection and love...

May God watch over and protect them

To my brothers : Boulakras, Balgacem, Haider, Malek, Rafik...

To my sisters : Saida, Rawya and Samira.

To my wife : Souad

To my children : Anwaar Redha and Afnane

To all my friends

To my colleagues

Finally, to everyone who contributed to the completion of this work.

Abdelouahab GAHTAR

```
    Science has gone a long way toward helping man to free
himself from the burden of hard labor; yet, science itself is
not a liberator. It creates means, not goals. It is up to men
to utilize those means to achieve reasonable goals [Albert
Einstein].
```

TABLE OF CONTENTS

Chapter III: Effect of temperature on the properties of nickel sulfide films

Chapter IV: Effect of molar concentration on the physical properties of NiS films

Chapter III: Effect of temperature on the properties of nickel sulfide films

Chapter IV: Effect of molar concentration on the physical properties of NiS film

GENERAL

INTRODUCTION

General Introduction

Environment and energy problems are at the top of the list of human concerns. Currently, energy sources such as solar and wind energy are developing rapidly since progress requires intelligent and diverse energy storage in devices. Thus, energy storage is becoming one of the key issues in energy production. The urgent development of efficient, clean and effective energy storage devices is needed [1]. Among efficient energy storage and conversion devices, the supercapacitor is a sustainable charge storage device. Based on the charge storage mechanism, it is classified into electric double layer capacitors (EDLC) and pseudo-capacitors [2]. EDLCs provide electrostatic ion absorption/desorption capability on the surface of the electrode material. Pseudo-capacitors generally provide a higher specific capacity than EDLC due to the rapid redox reactions [3].

Metal oxides and conductive polymers are well known as electrode materials with pseudo-capacitive properties. These pseudo-capacitive materials generally suffer from poor cyclic stability due to their high volume expansion and poor electrical conductivity, which limit their widespread application in practice [4].

Recently, transition metal sulfides such as FeS_2, CuS, MoS_2, NiS_2 and CoS_2 have a promising future in the fields of hydrogen evolution reaction catalysts, sensors, solar cells, lithium-ion batteries and supercapacitors due to their unique optical and electrical properties. Compared to metal oxides, transition metal sulfides have superior conductivity, mechanical and thermal stability and richer redox reactions. As a result, they have a better capacity and potential to be applied to electroactive materials for supercapacitors [5].

Nickel sulfide is an important member in the metal sulfides family [6], due to the variety of its phases and the diversity of applications such as lithium-ion batteries [7], supercapacitors [8] and solar cells [9]. The relatively complex nickel sulfide system was first investigated by Kullard and Yard in 1962 [10]. The nickel sulfide system contains a number of phases including NiS_2, Ni_3S_4, Ni_7S_6, Ni_9S_8, α- $Ni_{3+x}S_2$, Ni_3S_2, NiS, $Ni_{17}S_{18}$ and NiS_2 (Li et al. 2007). Most of the phases are present at low temperatures, which is one of the main advantages of nickel sulfide as a next-generation material.

Nickel sulfide thin films have been deposited by various methods such as spray pyrolysis [11], chemical bath deposition (CBD) [12], hydrothermal [13], successive ion layer adsorption and reaction (SILAR) [14], thermal evaporation [15], electrodeposition [16] and sol-gel [17].

The aim of this thesis is to prepare nickel sulfide thin films by the spray pyrolysis technique and to study the effect of different experimental parameters on the fundamental properties of nickel sulfide films. The parameters investigated are (substrate temperature and molarity) to understand the effects of these parameters on the properties of this material and to optimize their performance for use in optoelectronic devices such as supercapacitor electrodes. Developed layers have undergone morphological, structural, optical and electrical characterizations.

- **Outline of This Thesis**

The thesis is structured in four chapters. It begins by an introduction and it is concluded by recommendations for future research.

Chapter I: State of the art of supercapacitors and the nickel sulfide material

Chapter II: Experimental Techniques: Preparation and Characterization

Chapter III: Effect of temperature on the properties of nickel sulfide thin films

Chapter IV: Effect of molar concentration on the physical properties of nickel sulfide thin films.

References

[1]   L. Zhang, D. Shi, T. Liu, M. Jaroniec, J. Yu, Nickel-based materials for supercapacitors, Materials Today, vol. 25, pp. 35-65, 2019.

[2]   S.-W. Chou, J.-Y. Lin, Cathodic deposition of flaky nickel sulfide nanostructure as an electroactive material for high-performance supercapacitors, Journal of the Electrochemical Society, vol. 160, pp. D178, 2013.

[3]   W. Hu, R. Chen, W. Xie, L. Zou, N. Qin, D. Bao, CoNi2S4 nanosheet arrays supported on nickel foams with ultrahigh capacitance for aqueous asymmetric supercapacitor applications, ACS applied materials & interfaces, vol. 6, pp. 19318-19326, 2014.

[4]   Y. Tan, M. Liang, P. Lou, Z. Cui, X. Guo, W. Sun, X. Yu, In situ fabrication of CoS and NiS nanomaterials anchored on reduced graphene oxide for reversible lithium storage, ACS applied materials & interfaces, vol. 8, pp. 14488-14493, 2016.

[5]   J.-C. Xing, Y.-L. Zhu, Q.-W. Zhou, X.-D. Zheng, Q.-J. Jiao, Fabrication and shape evolution of CoS2 octahedrons for application in supercapacitors, Electrochimica Acta, vol. 136, pp. 550-556, 2014.

[6]   R.D. Tilley, D.A. Jefferson, The synthesis of nickel sulfide nanoparticles on graphitized carbon supports, The Journal of Physical Chemistry B, vol. 106, pp. 10895-10901, 2002.

[7]   L. Mi, Q. Ding, W. Chen, L. Zhao, H. Hou, C. Liu, C. Shen, Z. Zheng, 3D porous nano/micro nickel sulfides with hierarchical structure: controlled synthesis, structure characterization and electrochemical properties, Dalton Transactions, vol. 42, pp. 5724-5730, 2013.

[8]   T. Zhu, H.B. Wu, Y. Wang, R. Xu, X.W. Lou, Formation of 1D hierarchical structures composed of Ni3S2 nanosheets on CNTs backbone for supercapacitors and photocatalytic H2 production, Advanced Energy Materials, vol. 2, pp. 1497-1502, 2012.

[9]   W.S. Chi, J.W. Han, S. Yang, D.K. Roh, H. Lee, J.H. Kim, Employing electrostatic self-assembly of tailored nickel sulfide nanoparticles for quasi-solid-state dye-sensitized solar cells with Pt-free counter electrodes, Chemical Communications, vol. 48, pp. 9501-9503, 2012.

[10] G. Kullerud, R.A. Yund, The Ni-S system and related minerals, Journal of Petrology, vol. 3, pp. 126-175, 1962.

[11] A. Boukhachem, O. Kamoun, C. Mrabet, C. Mannai, N. Zouaghi, A. Yumak, K. Boubaker, M. Amlouk, Structural, optical, vibrational and photoluminescence studies of Sn-doped MoO3 sprayed thin films, Materials Research Bulletin, vol. 72, pp. 252-263, 2015.

[12] M.S. Sonawane, M.S. Shinde, R.S. Patil, Characterization of nickel sulphide thin films prepared by modified chemical method, (2015).

[13] W. Cui, C. Ge, Z. Xing, A.M. Asiri, X. Sun, NixSy-MoS2 hybrid microspheres: One-pot hydrothermal synthesis and their application as a novel hydrogen evolution reaction electrocatalyst with enhanced activity, Electrochimica Acta, vol. 137, pp. 504-510, 2014.

[14] S. Sartale, C. Lokhande, Preparation and characterization of nickel sulphide thin films using successive ionic layer adsorption and reaction (SILAR) method, Materials Chemistry and Physics, vol. 72, pp. 101-104, 2001.

[15] R.K. Singh, J. Narayan, Pulsed-laser evaporation technique for deposition of thin films: Physics and theoretical model, Physical review B, vol. 41, pp. 8843, 1990.

[16] M. Uplane, S. Mujawar, A. Inamdar, P. Shinde, A. Sonavane, P. Patil, Structural, optical and electrochromic properties of nickel oxide thin films grown from electrodeposited nickel sulphide, Applied surface science, vol. 253, pp. 9365-9371, 2007.

[17] B. Bräuer, D.R. Zahn, T. Rüffer, G. Salvan, Deposition of thin films of a transition metal complex by spin coating, Chemical physics letters, vol. 432, pp. 226-229, 2006.
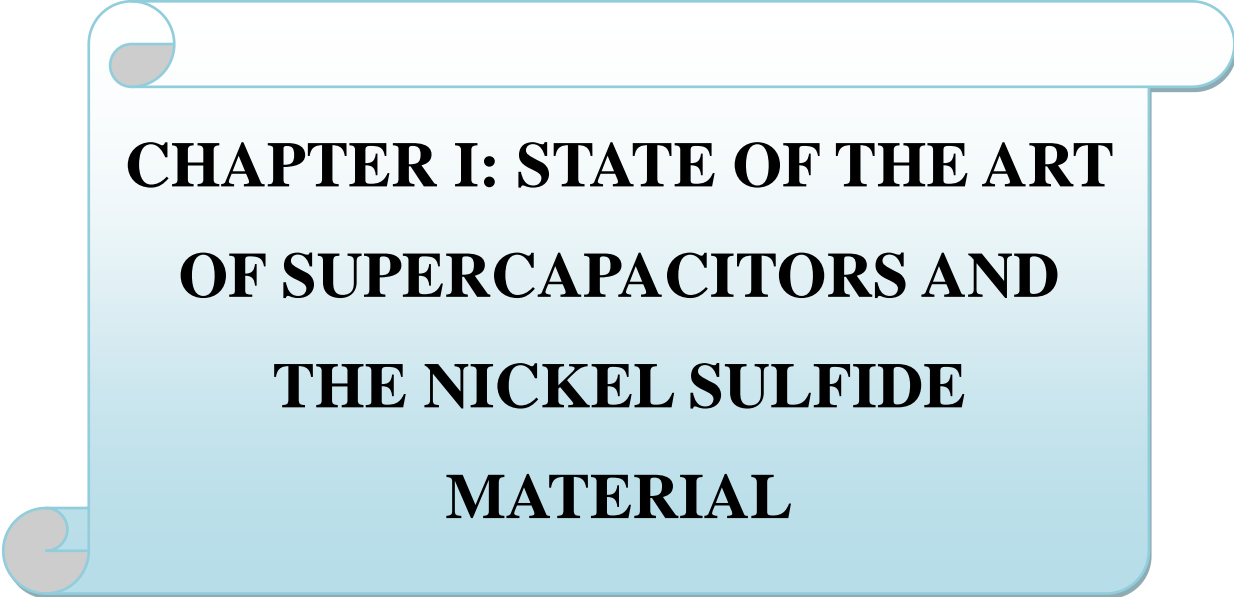
CHAPTER I: STATE OF THE ART OF SUPERCAPACITORS AND THE NICKEL SULFIDE MATERIAL

I.1. Introduction

Along this chapter, we will be limited to discuss some concepts related to the topic. We will start by defining supercapacitors; their types and fields of application will be determined and we will briefly review the various studies carried out in the near past on nanostructured nickel sulfide. Finally, we will present the material nickel sulfide (NiS), namely its crystal structure, its electrical and optical properties and their application.

I.2. History of Supercapacitor

According to Rael, Davat [1], the first patent for supercapacitors was granted to Becker (for the General Electric Company) in 1957. The invention concerned a method of storing electrostatic energy based on the electric double layer developed at the interface between a porous carbonaceous material and an aqueous electrolyte (sulfuric acid) with which it was impregnated. In 1969, Sohio filed another patent for a supercapacitor with a non-aqueous electrolyte allowing higher voltages. Supercapacitors were not marketed until the 1970s, by the companies NEC and Matsushita. These components with activated carbon electrode and aqueous or organic electrolytes are of low capacity (some Farad) and low power. The components with higher power and high specific energy only appeared in the 1990s.

I.2.1. Supercapacitor definition

Supercapacitors also called ultracapacitors and electric double layer capacitors (EDLC) are capacitors with capacitance values greater than any other capacitor type available today. Capacitance values reaching up to 800 Farads in a single standard case size are available. Supercapacitors have the highest capacitive density available today with densities so high that these capacitors can be used normally to applications reserved for batteries. Supercapacitors are not as volumetrically efficient and are more expensive than batteries but they do have other advantages over batteries making the preferred choice in applications requiring a large amount of energy storage to be stored and delivered in bursts repeatedly [1].

I.2.2. Types of supercapacitors

supercapacitors can be divided into three general classes: electrochemical doublelayer capacitors, pseudocapacitors, and hybrid capacitors [2]. Each class is characterized by its unique mechanism for storing charge. These are, respectively, non-Faradaic, Faradaic, and a combination of the two. Faradaic processes, such as oxidation-reduction reactions, involve the transfer of charge between electrode and electrolyte. A nonFaradaic mechanism, by contrast, does not use a chemical mechanism. Rather, charges are distributed on surfaces by physical processes that do not involve the making or breaking of chemical bonds. This section will present an overview of each one of these three classes of supercapacitors and their subclasses, distinguished by electrode material. A graphical taxonomy of the different classes and subclasses of supercapacitors is presented in Figure I.1.
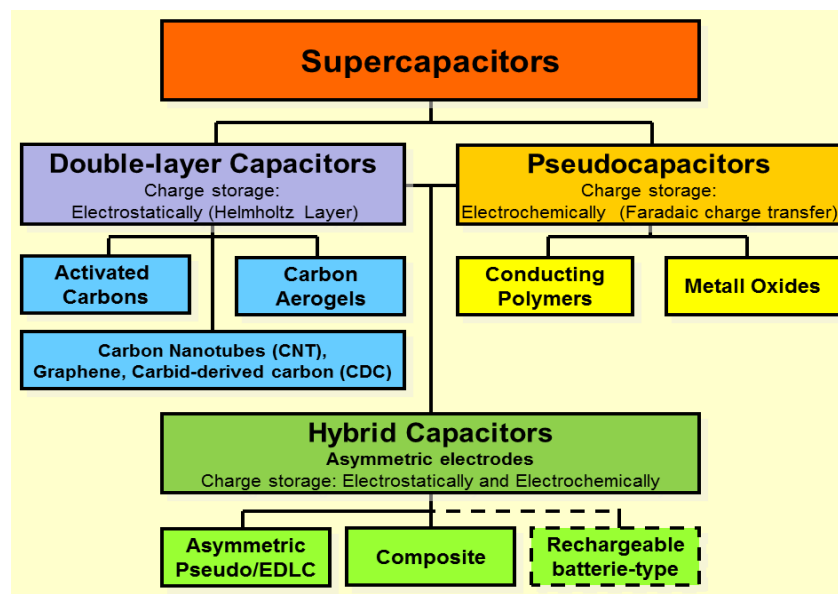
Figure I.1: Types of supercapacitors

1. Double layer capacitors

In EDLC, charge accumulation occurs at the interface of electrode material and the gel electrolyte. This charge accumulation is a non-faradic process responsible for the capacitance of EDLC. During charging, electrons travel from negative to the positive electrodes through external load whereas cations and anions move towards negative and positive electrodes respectively inside the electrolyte. During discharging, the reverse

mechanism happens. There is no transfer or exchange of charges across the interface of the electrode and the electrolyte. The concentration of the electrolyte remains constant during charging and discharging which stores the energy in the EDLC [3].

The schematic diagram showing the charge accumulation in electrochemical double layer capacitor (EDLC) is shown in Figure I.2.
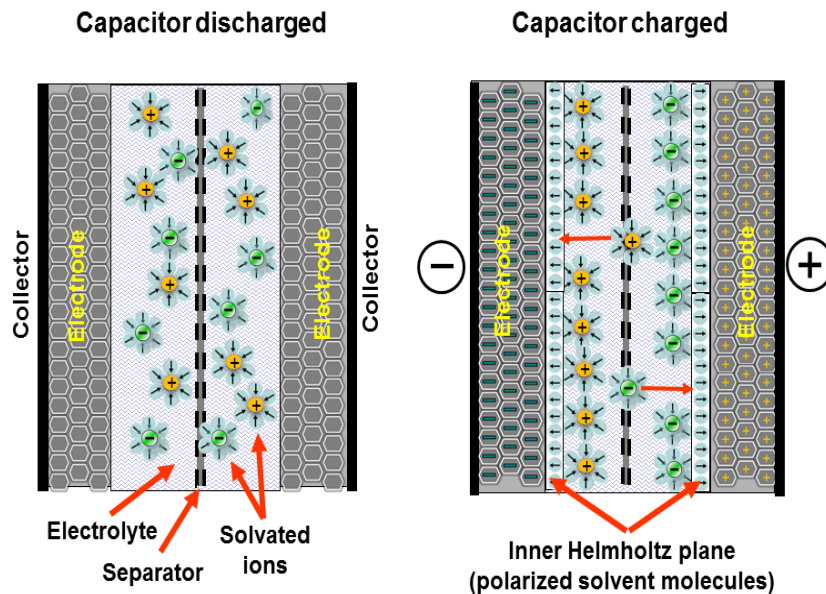
Figure I.2: Charging and discharging process in EDLC supercapacitor [4]

2. Pseudo-capacitors

In contrast to EDLCs, which store charge electrostatically, pseudocapacitors store charge faradaically through the transfer of charge between electrode and electrolyte. This is accomplished through electrosorption, reduction-oxidation reactions, and intercalation processes. These Faradaic processes may allow pseudocapacitors to achieve greater capacitances and energy densities than EDLCs [5].

There are two electrode materials that are used to store charge in pseudocapacitors, conducting polymers and metal oxides. The charge transfer that takes place in these reactions is voltage dependent, so a capacitive phenomenon occurs. There are two types of reactions that can involve a charge transfer that is voltage dependent. One is a redox reaction and another is adsorption of ions. In a redox reaction involving an oxidant, *ox*, and reductant, *red,* of the form:

$$OX + Z\,e^- \leftrightarrow Red \ldots \ldots \ldots \ldots (I.1)$$

The potential, E, is given by the Nernst equation as [6]:

$$E = E_0 + \frac{RT}{ZF} Ln\left(\frac{\check{R}}{1-\check{R}}\right) \ldots \ldots \ldots \ldots \ldots \ldots (I.2)$$

where E_0 is the standard potential, R is the gas constant, T is the absolute temperature, F is the Faraday constant, and $\check{R}$ is defined as *[ox] / ([ox]+[red])*,(where square brackets denote species concentrations). The amount of charge *q* (given by the product *zF*), is therefore a function of the potential *E*. Differentiation of Equation. 2 thus produce a pseudocapacitive relation.

3. Hybrid capacitors

Hybrid capacitors attempt to exploit the relative advantages and mitigate the relative disadvantages of EDLCs and pseudocapacitors to realize better performance characteristics. Utilizing both Faradaic and non-Faradaic processes to store charge, hybrid capacitors have achieved energy and power densities greater than EDLCs without the sacrifices in cycling stability and affordability that have limited the success of pseudocapacitors. The research has focused on three different types of hybrid capacitors, distinguished by their electrode configuration: composite, asymmetric, and battery-type respectively [7].

I.2.3. Materials for Supercapacitor

The critical components of supercapacitors include the electrodes, electrolyte and the separator. The characteristics of electrode materials for supercapacitors include high cyclability, long-term stability, high surface areas, and resistance to electrochemical oxidation/reduction. The focus seems to be, however, on achieving high surface areas with low 'matrix' resistivity. Carbonaceous materials have been particularly popular owing to their large surface areas. High temperature heat-treatment of active carbon precursors such as coconut shells, wood powders, coal tar, resins and resorcinol-formaldehyde and related polymers yield active electrode materials with surfaces ranging between 1000 and 1500m^2/g, that result in capacities as high as 500F/g in alkaline electrolytes. Another class of materials includes modified carbon and carbon-composites such as activated carbonpolyacene, platinized activated carbon, polyoxometallate modified carbon and

carbon-inert particulate material which have led to capacitance values between 150 and 200F/cm^2. Besides, conducting metal oxides such as RuO_2 and IrO_2 yield capacities of the order of 150–250µF/cm^2, which it happens to be several times larger than the carbon-based capacitors. These values arise from pseudocapacitance believed to occur between the surface ruthenium ions and protons. Indeed, substantially high specific capacitance values near 768F/g have been achieved when amorphous (RuO_2. xH_2O) is used as the electrode material [8, 9]. Activated glassy carbon and high surface area gold are planar or extended area electrode materials that provide both high and short pulse charges. The absence of a porous character associated with the electrode structure and/or the absence of any faradaic process is required for short pulse capacitors with their overall capacitance arising from an electrical double-layer. Conducting polymers are complementary material to carbon and metal oxides. A wider voltage window is achieved with derivatized polythiophenes in non-aqueous solutions. However, long-term stability is still a problem. Recently, nitrides of molybdenum, titanium and iron, carbon nanotubes and glutarsonitrile have been reported to yield energy densities of the order of 10Wh/kg when used with carbon electrodes. The electrolytes used are $LiClO_4$, $NaClO_4$, $LiAsF_6$, and quaternary phosphonium salts. The choice of electrolytes demands the requirement for hermetic seals. This has led to the use of solid polymer electrolytes which are usually ionomers. Donor polyether solvents such as polyethylene oxide (PEO), where anions are usually not coordinated to the solvent molecules unless through hydrogen bonding to hydroxyl end groups are quite frequently used along with a plasticizer [10].

I.2.4. Characterization of supercapacitors

The characterization of the supercapacitors is done by analyzing the CV and CD curves which are plotted by the AUTOLAB software. The performance of the supercapacitors can be evaluated by three parameters, specific capacitance, energy density and power density.

- **Specific capacitance:** is calculated from the CD curve by the formula [11]:

$$C = I \left(\frac{\Delta t}{A \, \Delta V}\right) \dots \dots \dots \dots \dots \dots \dots \dots . . (I.3)$$

✓ I is the Current

✓ Δt is the discharging time

✓ A is the area of electrode

✓ ΔV is potential window width.

- **Energy density** E: is calculated by [12]:

$$E = \frac{C.V^2}{2} \dots \dots \dots \dots \dots \dots \dots (I.4)$$

✓ C is the Specific Capacitance.

✓ V is the potential window width.

- **Power density** is calculated by [13]:

$$P = \frac{E}{\Delta t} \dots \dots \dots \dots \dots \dots \dots \dots . (I.5)$$

✓ E is the Energy density.

✓ Δt is the discharge time.

I.2.5. Supercapacitor properties

The properties of a supercapacitor are [14-16]:

✓ a high capacity (from a few Farads to several thousand Farads)

✓ A low voltage resistance limited by the presence of an electrolyte (between 1V in aqueous medium and 3.5V in organic medium).

✓ a specific power between 800 and 2000W.kg^{-1}

✓ an energy density by mass greater than that of capacitors and of the order of 5 to 15Wh.kg^{-1} : 15Wh.kg^{-1} for noble materials and around 5Wh.kg^{-1} for carbonaceous materials

✓ an energy density by volume of between 1 and 10Wh.L^{-1}

✓ A time constant for the weak discharge due to the low displacement of ions in the electrolyte. A supercapacitor is discharged in seconds or even tens of seconds.

I.2.6. Applications of supercapacitors [17, 18]

✓ Flashlight applications

✓ Solar power applications

✓ Supercapacitors are used in electronic devices such as laptop computers, portable media players, handheld devices, and photovoltaic systems to stabilize the power supply.

✓ Supercapacitors are used as temporary energy storage devices for energy harvesting systems.

✓ Supercapacitors are used in defibrillators (an instrument that controls irregular heartbeat by supplying electric current to the chest wall).

I.2.7. Advantage and disadvantage of supercapacitors [19]

➢ **Advantages**

✓ Stores a large amount of charge compared to the conventional capacitors (High capacitance).

✓ Delivers energy or charge very quickly (high power density)

✓ Long lifetime

✓ Low cost

✓ Supercapacitors do not explode like batteries even if it is overcharged.

➢ **Disadvantages**

✓ Low energy density

✓ Very low maximum voltage per cell (2.7V) for activated carbon technology

✓ Hazardous electrolyte (acetonitrile) charge/discharge

✓ components which may contain acetonitrile (flammable and explosive)

✓ Non-linear behaviors of the component

I.3. Nanostructured Nickel Sulfides

I.3.1 Nanomaterials

Nanomaterials are materials processing grain sizes on the order of a billionth of a meter. These materials are often called nanocrystalline materials. The extremely fascinating and useful properties of these materials exploited for a variety of structural and non-structural applications. Nanophase or nanostructured materials, a new branch of

materials research, are attracting a great deal of attention because of their potential applications in areas such as electronics [20], optics [21], catalysis [22], magnetic [23], nanocomposites [24] and biology [25]. The unique properties and the improved performances of nanomaterials are determined by their sizes, surface structures and inter-particle interactions. The nanometer size covers a wide range between several nanometers (nm) and several hundred nanometers. To distinguish nanomaterials from bulk, it is vitally important to demonstrate the unique properties of nanomaterials and their perspective impacts in nanotechnology.

The diversity of nanomaterial's can be found depending on its chemical nature and its synthesis procedures. Nucleation and growth are two important processes in synthesizing particles. Nucleation is a process in which an aggregation of atoms is formed, and is the first step of phase transformation. The growth of nuclei results in the formation of large crystalline particles. Therefore, the study of size-dependent structures and properties of a nanoparticle is key in understanding the nucleation and growth of crystals.

In general, synthesis methods of nanocrystalline materials classified into two groups, the top-down approach and bottom-up approach. The miniaturization of components for the construction of useful devices and machines has been pursued by a top-down approach. An alternative and most-promising strategy to exploit science and technology at the nanometer scale is offered by the bottom-up approach, which starts from nano or sub-nano scale objects (atoms or molecules) to build up nanostructures. The imperfection of the surface structure and defects can be minimized by a bottom-up approach. The main driving force behind the bottom-up approach is the reduction of Gibb's free energy. Therefore, the materials produced are closer to their equilibrium state with more homogeneous chemical composition, better short and long range order.

I.3.2. Inorganic nanomaterials

The field of nanomaterials is loosely organized into organic nanomaterials such as fullerenes, carbon nanotubes and etc., and inorganic nanomaterials based on their elements, such as silicon, transitional metals and etc. Group II-VI members are vital materials for high-performance optoelectronic devices such as light-emitting diodes (LEDs) and laser diodes (LDs) operating in the blue or ultraviolet spectral range. II-VI category includes,

transitional metal oxides (such as ZnO, TiO2 and etc.,), transitional metal sulfides (such as NiS, CuS, PbS and etc.,), metal selenides (such as ZnSe, CdSe and etc.,), metal telluride's (such as ZnTe, SnTe and etc.,) and various other materials. This group of materials includes metallic, semiconducting and insulating nature, which attracts more attention towards application.

A synthesis method plays an important role in the practical uses of inorganic nanomaterials for commercial applications. While inorganic nanomaterials have been generated by physical methods such as laser ablation [26], arc discharge [27] and evaporation [28], Chemical methods have been proved to be more effective as they provide better control of sizes, shapes and functionalization. Chemical synthesis of inorganic nanomaterials has been reviewed by several groups [29] innumerable improvements have been reported continually in the last few years.

Several chemical methods such as wet chemical, chemical bath deposition, sonochemical growth [30], microwave-induced deposition [31], hydrothermal method [32], temperature controlled injection method and etc., have been used to synthesize the nanocrystals. Most of the methods produce irregular shapes, sizes and structures. Out of all the above methods, hydrothermal and temperature controlled injection method has unique advantages controlling the size and shape. It is possible to grow semiconducting as well as metallic quantum dots. Temperature controlled injection method offers greater control over the physical and chemical properties. It is possible to finely control the growth and thus obtain quantum dots with small and narrow size distribution and desired stoichiometry. The growth can be size selective by varying parameters like temperature, precursor's type and concentration, surfactant type and concentration, and the reaction time. Hydrothermal and temperature injection methods have several other advantages such as low cost facilities, possibilities of production of large amounts of material, small size, high crystallinity and formation of surface modifiable nanoparticles.

I.3.3. Transitional metal sulfides

Nanostructured metal sulfides have been extensively studied due to their importance in interpreting quantum size effects and applications in emerging devices, such as solar cells [33, 34], sensors, light-emitting diodes (LED's), fuel cells, nonvolatile memory

devices, thermoelectric devices [35] and lithium-ion batteries [36, 37]. These are the major group of minerals that provide the crystal chemist a rich field for investigation due to their diverse structural types. They are abundant and cheap since they exist as minerals such as heazlewoodite (Ni_3S_2), pyrite (FeS_2), Chalcocite (Cu_2S) and so on.

Zinc sulfide (ZnS) nanostructures have versatile potential applications as optoelectronic devices due to their excellent properties of luminescent and photochemistry. ZnS has a very wide bandgap of ~3.7 eV energy and considered to be one of the well-studied important semiconducting materials [38]. Copper sulfide (Cu_2S) is another important II-VI metal sulfide which has an ideal bandgap of 1.2 eV for the use in solar cells as an extremely thin absorber [39]. A p-type Cu_2S semiconductor has great potential applications as cathode materials for lithium-ion batteries, nonlinear optical materials and solar radiation absorbers [40].

Cobalt sulfide (Co_9S_8) is found to have the highest catalytic activity for dioxygen reduction in acidic solution among a variety of transitional metal sulfides. Because of this property it is promising for the anode material for solid oxide fuel cells (SOFC) [41, 42], dye sensitized solar cells [43], rechargeable lithium-ion batteries [44] and super-capacitors [43]. Magnetic susceptibility results suggest that it is of Pauli paramagnetism used for magnetic devices. Colloidal Lead sulfide (PbS) nanocrystals have been utilized for optical switching and photonic applications [45]. PbS is one of the earliest synthesized and well-studied quantum dots [45, 46]. It is also utilized for IR detector applications.

Nickel sulfide is another metal sulfide. Because of its complications in its phases, it has not studied in detail toward structural control. In this work, I will report a detailed study on nickel sulfide.

I.3.3.1. Nickel sulfide

Nickel sulfide is one of the important elements in the metal sulfide family [47, 48] because of the variety in its phases and diversity in applications such as in lithium-ion batteries, supercapacitors [49], and dye-sensitized solar cells [50]. The relatively complex nickel sulfide system was first investigated by Kullard and Yard in 1962 [51]. Figure I.3 showed the binary nickel sulfide phase diagram. The nickel sulfide system contains a

number of phases including NiS_2, Ni_3S_4, Ni_7S_6, Ni_9S_8, α- $Ni_{3+x}S_2$, Ni_3S_2, NiS, $Ni_{17}S_{18}$ and NiS_2 [52]. Most of the phases are present at low temperature, which is one of the major advantages for nickel sulfide as a next generation material. According to the phase diagram of nickel sulfide, the sulfur-rich part of the system appears to be rather simple with only a few phases compared with the complex nickel-rich phases. In recent years, many research groups have attempted to prepare different nickel sulfide phases for specific applications.
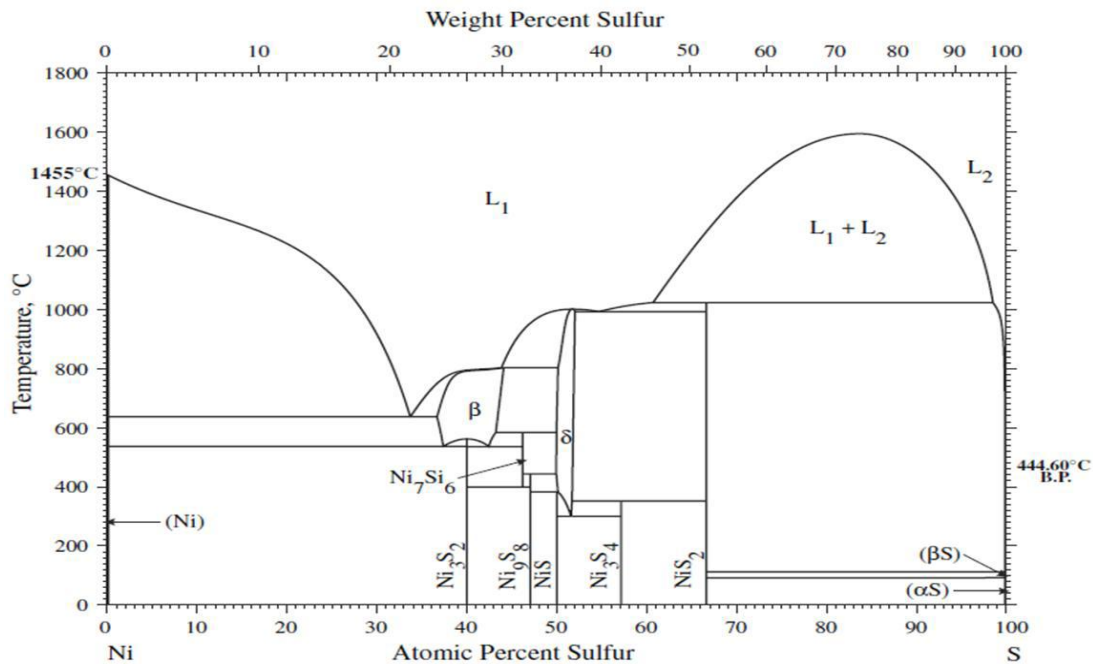
Figure I.3: Binary phase diagram of nickel sulfide (Ni-S) [53]

I.3.3.2. Nickel sulfide properties

I.3.3.2.1. Structural characteristics

The prominent phases exhibited by NiS are two stoichiometric phases: the low temperature rhombohedral (β-NiS, millerite) and high temperature hexagonal (α- NiS) crystal structures and one non-stoichiometric phase hexagonal ($NiS_{1.03}$) crystal structure[54]. The high temperature α- NiS phase is antiferromagnetic and exhibits a metal insulator transition with an abrupt change in magnetic susceptibility when it is cooled below a transition temperature, i.e., Neel temperature T_N=271K. Below transition temperature α- NiS has a magnetic moment of about 1.7 μB; however above the transition the magnetic moment appears negligibly small [55, 56], and Neel suggested that some small antiferromagnetic particles, due to the uncompensated number of spins on two

sublattices, should exhibit superparamagnetism and weak ferromagnetism. Hexagonal NiAs-type $NiS_{1.03}$ catalyst showed very good catalytic properties, and it was found that the formation of this NiAs-like hexagonal $NiS_{1.03}$ structure could be related to the formation of nickel vacancies [57]. Nickel sulphide is the inorganic compound with the formula NiS. It is a black solid with a density 5500 kg/m3. Its melting point is 976ºC and the boiling point is 1388ºC. Its elemental percentage is: Ni =64.67% and S= 35.33% [58, 59]. Solid state structure of nickel sulfide is shown in Figure I.4.
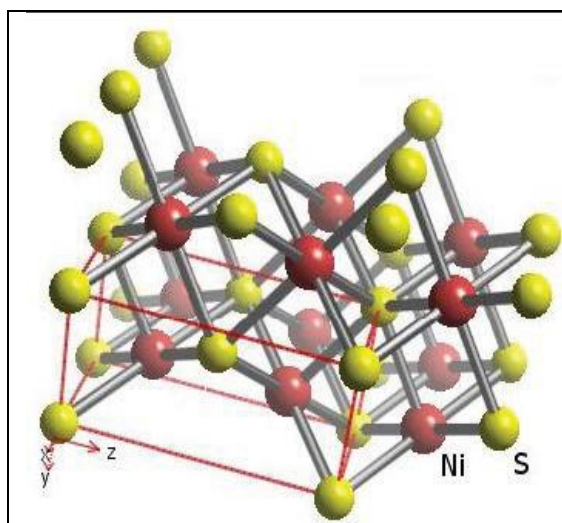
| **Figure I.4: Solid state structure of nickel sulfide** | **Figure I.5: NiAs type structure of nickel sulfide** |

| **Figure I.6: The crystal structure of millerite NiS [60]** | **Figure I.7: The local structural environment of the Ni atom which is penta coordinated with S** |
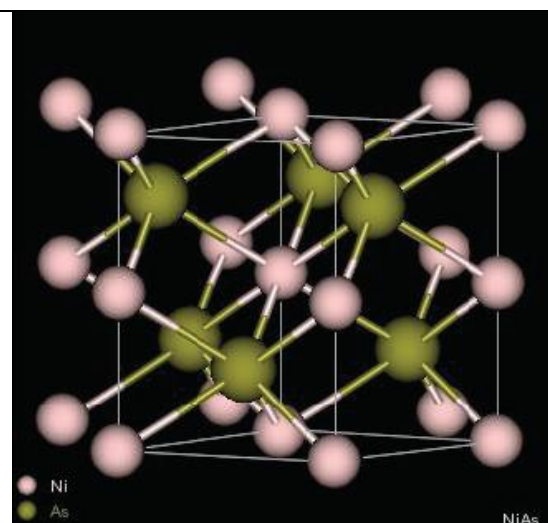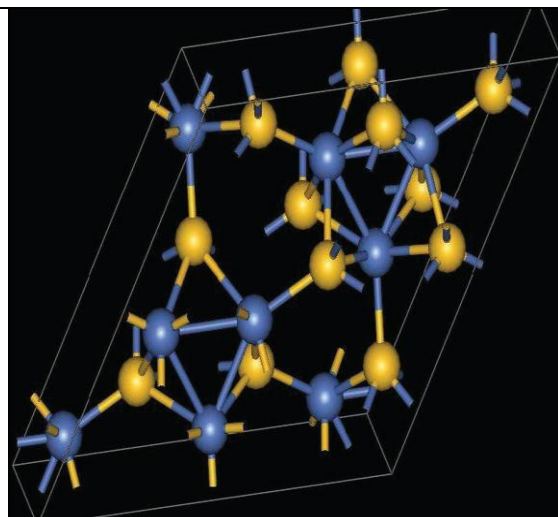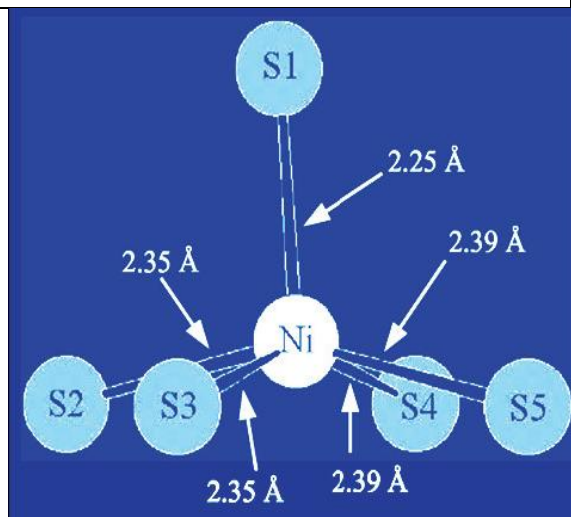
The high temperature phase of nickel sulphide (α- NiS) exhibits a hexagonal NiAs structure, whereas the low temperature phase nickels supplied (β- NiS) rhombohedral

millerite structure. The hexagonal NiAs structure is one of the most important materials in transition metal chemistry. Figure I.5 shows the NiAs-type structure showing the linkage of ions in a unit cell. The metal and anions lie respectively on interpenetrating simple hexagonal and close-packed hexagonal sublattices. The transition metal atoms occupy all the octahedral holes in the closed packed hexagonal array of anions and the anions are surrounded by six transition metal atoms in the trigonal prism. The octahedrals mutually share faces along the c axis, and pairs of octahedral share faces forming trigonal bipyramidal holes.

The NiAs structure has two important features: i) the ability to accommodate additional transition metal atoms in the trigonal bipyramidal holes, and ii) to omit metal atoms, either randomly or on planes perpendicular to the c axis [61, 62]. The crystal structure of millerite NiS is shown in Figure I.6 [60]. Here, the Ni atoms have five nearest neighbor S atoms occupying the corners of the square pyramid.

Figure I.7 shows the local structural environment of the Ni atom which is penta coordinated with S atoms in the millerite NiS. In this pyramid geometry (Figure I.7) the Ni atoms are displaced slightly out of the basal plane, toward the apical sulphur atom [63].

I.3.3.2.2. Synthesis and Chemical Properties

Until now, many methods have been employed to prepare novel structures of NiS. The most traditional method to prepare NiS is solid state synthetic technique at elevated temperature [64]. This process requires intermittent grinding and it gives little control in material stoichiometry. Later, molecular precursors methods [65] including the thermal decomposition of compounds containing a M-S bond, such as dithiolato complex [66] and thiocyanate complex [67] have been used to prepare NiS.

Nickel sulphide has been prepared by vapor phase reaction [54], the elemental reaction in liquid ammonia [68], homogeneous sulphide precipitation followed by a sulphiding procedure and precipitation reaction between metal salts and sulphiding agent, followed by heat treatment in reducing gas [54]. However, the products obtained usually exhibit relatively large grain sizes, small surface areas and irregular morphology, which are disadvantageous for their application.

Various approaches such as ion exchange and precipitation procedures [69], gas phase reaction [70] and thermal decomposition [67] have been developed to fabricate NiS nanocrystals. Among these approaches, many are based on high temperature processes that generally require intricate processing and the use of high temperatures for long period of time, which may make the control of composition and morphology difficult. These difficulties have aroused extensive attention to the low temperature synthesis of nickel sulfides.

In recent years, many low temperature syntheses of nickel sulfides have been developed including templated-mediated process [71], ball milling [72], polycol [73], spark plasma sintering [74], high boiling point solvent [75], solvothermal and hydrothermal [76]. Olivas et al [47] prepared nickel sulphide catalysts by homogeneous precipitation method by varying the homogeneous time and the sulphiding temperature. Structure characterization studies by X-ray diffraction showed the formation of two main crystalline phases ($NiS_{1.03}$, NiS-millerite and Ni_3S_4). The prepared catalysts present shapeless particles with an average size between 100 and 150 μm. The S/Ni atomic ratio measured by EDS was very similar for all catalysts. The average S/Ni ratio was 1.25± 0.13, indicating that the surface of catalysts (with average thickness of approximately 1μm) contains excess sulphur with respect to NiS and especially to Ni_3S_4. The formation of millerite NiS or $NiS_{1.03}$ occurs at the constant sulphiding temperature, when time of homogenization of precursors increases.

I.3.3.2.3. Optical and Electrical Properties

Sartale and Lokhande [77] studied the optical absorption spectra of NiS films at room temperature. Extrapolating the straight line portion of the plot of $(\alpha h\upsilon)^2$ against $h\upsilon$ to the energy axis for zero absorption coefficient (α) gives the band gap equal to 0.45 eV. The room temperature dark electrical resistivity of NiS films deposited onto a glass substrate was found to be of the order of 10 Ωm. The variation of (log ρ) with the inverse of temperature (1000/T) was plotted. The decrease in electrical resistivity with an increase in temperature suggests the semiconducting behavior of NiS films. The activation energy was estimated to be 0.15 eV which represents the average energy of the carriers with respect to Fermi energy, if the carriers can only move at the bottom or top of the well defined band.

Yang et al [78] obtain the photoluminescence (PL) spectrum of NiS nanoparticles embedded in sol-gel silica xerogel. The PL spectrum consists of two emission peaks, one at 440 nm (excitation at 380 nm) and the other at 610 nm (excitation at 490 nm). This novel emission is due to the NiS nanoparticles embedded in the porous silica xerogel.

Kheiw et al [79] studied the UV-Vis-NIR absorption spectra of NiS nanoparticles prepared by the microemulsion technique. The optical bandgap energies of 0.010, 0.050, 0.100 M of NiS nanoparticles have been estimated to be 1.48, 1.15 and 0.99 eV respectively.

Chen et al [80] studied the room temperature photoluminescence spectra of the as grown nickel sulphide nanowires by a Jobin Yvon Labram spectrometer with a He-Cd laser with an excitation wavelength of 332 nm. The peak shows a broad emission at 418 nm. This broad emission suggests that the interaction is not of an excimer, but is rather a consequence of intermolecular exciton strong interactions. NiS particles of 6-10 nm incorporated into mordenite revealed the band edge at 318 nm [81]. A comparison of the absorption edge of bulk NiS with NiS mordenite samples shows a blue shift in the onset of absorption observed in the mordenite samples. This phenomenon has been ascribed to a decrease in particle size. It is well known in the case of semiconductors, the bandgap between the valence and conduction band increases as the size of the particle decreases in the nanosize range.

Sohrabnezad et al [82] studied the absorption spectra of millerite NiS and NiCoS nanoparticles in mordenite zeolite hosts. The samples show blue shifts in the absorption edges. When the Co concentration decreases and correspondingly Ni concentration increases. This phenomenon of blue shift of the absorption edge has been ascribed to a decrease in particle size. The bandgap energy of NiS nanoparticle is found to be 3.53 eV. Furthermore, it is readily seen that when the Ni concentration increases, the peaks corresponding to the ternary systems become asymmetric, indicative of more than one energy band gap associated with particles of different composition.

Pan et al [83] obtained the photoluminescence spectrum of NiS nanostructures measured at room temperature at an excitation wavelength of 325 nm. A sharp emission band peaking at 648 nm, a weak blue band at 482 nm and two red bands at 622 and 674 nm

was observed. The emission at 648 nm may be a frequency doubling peak. The blue band at 482 nm (2.57 eV) was attributed to the band edge emission, with about 0.77 eV blue shift compared to the bulk crystal (1.8 eV) due to the quantum size effect. The red emission at 622 and 674 nm were attributed to the excess S in the products, which might induce a new energy state in the gap.

I.3.3.2.4. Magnetic Properties

Zhang et al [54] studied the magnetic properties of α-NiS nanocrystals. The temperature dependence of magnetization measured under the ZFC and FC processes at an applied field of 100 Gauss. The magnetization of α-NiS increases with decreasing temperature in both zero field cooling (ZFC) and field cooling (FC) processes, indicating a paramagnetic behavior, in contrast to antiferromagnetic from its bulk material. It suggests that the long range antiferromagnetic ordering was destroyed in the nanoscale materials. The paramagnetic behaviour might arise from the so-called finite size effect and/or modification of the bulk state due to surface effect. In addition, the magnetization of the as-prepared nanoscale α-NiS is about five hundred times larger than that of the bulk materials at 5K. Such enhanced magnetization is often observed in nanoscale materials due to the size effect. The hysteresis loop reveals that the α-NiS nanoparticles have a remanent magnetization of 0.00012 emu/g and coercivity of 155 Oe. These results indicate that there are some weak ferromagnetic interactions, which arise from the uncompensated spins in the surface due to the layer surface atoms to bulk atoms, exist at low temperature range.

Wang et al [83] studied the magnetic hysteresis loop of nickel sulphide nanotubes formed by a directional infiltration self assembly route in AAO templates. The nanotubes with 200 nm diameter and about 20 nm thickness of the tube wall exhibit ferromagnetic interactions, which it is even tending to superparamagnetic property at room temperature.

Salavathi Niasari et al [84] studied the magnetization versus applied magnetic field (M-H) curve for the as-synthesized α-NiS nanocrystal. The M-H curve reveals a weak ferromagnetic behavior with remnant magnetization (Mr) and coercivity (Hc) values of 0.0011 emu/g and 154 Oe respectively. Magnetization measurements indicate that the nanoparticles are no longer antiferromagnetic.

Tang et al [85] observed the magnetic properties of flower-like α-NiS nanostructures. They reported the temperature dependence of magnetization of the α-NiS flowers in both zero fields cooling and field cooling processed at an applied field of both 70 and 130 kOe in the temperature range of 5-300K. The α-NiS flower exhibits the transition from paramagnetism to ferromagnetism with the blocking temperature of about 12K, and the M(H) at 5K shows the coexistence of antiferromagnetism and ferromagnetism, and the remnant magnetization has a value of about 0.14 emu/g. The remnant magnetization of the flower-like α-NiS nanostructure is much high at 5K compared to that of bulk α-NiS, indicating strong ferromagnetic interaction, which arise from the uncompensated spins at the surface of the nanoflakes at low temperature.

The nanoflakes constituting the α-NiS flower is very thin, about 20 nm. The nanocrystals composed of nanoflakes are single crystalline with a size of only about 15 nm, and can be regarded as a single magnetic domain structure. The magnetic exchange coupling between the interconnected nanocrystals could contribute to the high remnant magnetization at low temperatures. These observations are consistent with the presence of an antiferromagnetic particle core that is superimposed to a net moment due to the intrinsic weak ferromagnetism and to the nanoscale uncompensated moment at low temperature.

Bala et al [86] reported the hysteresis of the Ni nanoparticles and Ni/ZnS nanocomposites measured at room temperature. The saturated magnetization value (Ms) of Ni nanoparticles is found to be 49 emu/g, and that for Ni/ZnS nanocomposites is 31 emu/g.

I.4. Conclusion

This chapter focused on supercapacitors, their properties, and their areas of use. It attempts also to shed some light on the metal sulfide transition in general, and the nickel sulfide in particular. Recently, Transition Metal Sulfides (TMS) became one of the subjects of great concern to researchers due to their high electrical conductivity, good electrochemical stability, respect for the environment and low cost of production. Some (TMS) such as NiS, CoS, SnS, CuS and ZnS have been widely exploited as new electrode materials for supercapacitors due to their distinctive properties compared to the oxides and hydroxides of these metals.

References

[1]   M. S. Halper and J. C. Ellenbogen, "Supercapacitors: A brief overview," MITRE Nanosystems Group, 2006.

[2]   A. Burke, "Ultracapacitors: why, how, and where is the technology," Journal of Power Sources, vol. 91, pp. 37-50, 2000.

[3]   R. Kötz and M. Carlen, "Principles and applications of electrochemical capacitors," Electrochimica Acta, vol. 45, pp. 2483-2498, 2000.

[4]   V. I. Birss, B. Conway, and J. Wojtowicz, "The role and utilization of pseudocapacitance for energy storage by supercapacitors," 1997.

[5]   I.-H. Kim and K.-B. Kim, "Ruthenium oxide thin film electrodes for supercapacitors," Electrochemical and Solid State Letters, vol. 4, p. A62, 2001.

[6]   K. Aoki, "Nernst equation complicated by electric random percolation at conducting polymer-coated electrodes," Journal of electroanalytical chemistry and interfacial electrochemistry, vol. 310, pp. 1-12, 1991.

[7]   E. Frackowiak, V. Khomenko, K. Jurewicz, K. Lota, and F. Béguin, "Supercapacitors based on conducting polymers/nanotubes composites," Journal of Power Sources, vol. 153, pp. 413-418, 2006.

[8]   K. S. Ryu, K. M. Kim, N.-G. Park, Y. J. Park, and S. H. Chang, "Symmetric redox supercapacitor with conducting polyaniline electrodes," Journal of Power Sources, vol. 103, pp. 305-309, 2002.

[9]   M. Mastragostino, C. Arbizzani, and F. Soavi, "Polymer-based supercapacitors," Journal of Power Sources, vol. 97, pp. 812-815, 2001.

[10]   C. Arbizzani, M. Mastragostino, and L. Meneghello, "Polymer-based redox supercapacitors: A comparative study," Electrochimica Acta, vol. 41, pp. 21-26, 1996.

[11]   A. Allagui, T. J. Freeborn, A. S. Elwakil, M. E. Fouda, B. J. Maundy, A. G. Radwan, Z. Said, and M. A. Abdelkareem, "Review of fractional-order electrical characterization of supercapacitors," Journal of Power Sources, vol. 400, pp. 457-467, 2018.

[12]   F. Barzegar, A. Bello, D. Momodu, M. J. Madito, J. Dangbegnon, and N. Manyala, "Preparation and characterization of porous carbon from expanded graphite for high

energy density supercapacitor in aqueous electrolyte," Journal of Power Sources, vol. 309, pp. 245-253, 2016.

[13] K. R. Prasad and N. Miura, "Electrochemical synthesis and characterization of nanostructured tin oxide for electrochemical redox supercapacitors," Electrochemistry communications, vol. 6, pp. 849-852, 2004.

[14] H. Ibrahim, A. Ilinca, and J. Perron, "Energy storage systems—Characteristics and comparisons," Renewable and sustainable energy reviews, vol. 12, pp. 1221-1250, 2008.

[15] J.-C. Lassègues, Supercondensateurs: Ed. Techniques Ingénieur, 2001.

[16] A. Marquet, C. Levillain, A. Davriu, S. Laurent, and P. Jaud, "Stockage d'électricité dans les systèmes électriques," Techniques de l'ingénieur. Génie électrique, vol. 8, pp. D4030. 1-D4030. 29, 1998.

[17] S. Azib, A. A. Zaidi, and S. Taraft, "Étude d'un Système de Stockage par un Supercondensateur," Université A/Mira de Bejaia, 2017.

[18] N. Devillers, "Caractérisation et modélisation de composants de stockage électrochimique et électrostatique," 2012.

[19] C. Largeot, "Développement de supercondensateurs carbone/carbone: relation entre la taille des ions de l'électrolyte et la taille des pores de la matière active," Université de Toulouse, Université Toulouse III-Paul Sabatier, 2009.

[20] Q. Liu, Z.-F. Li, Y. Liu, H. Zhang, Y. Ren, C.-J. Sun, W. Lu, Y. Zhou, L. Stanciu, and E. A. Stach, "Graphene-modified nanostructured vanadium pentoxide hybrids with extraordinary electrochemical performance for Li-ion batteries," Nature communications, vol. 6, pp. 1-10, 2015.

[21] R. C. Masters, A. J. Pearson, T. S. Glen, F.-C. Sasam, L. Li, M. Dapor, A. M. Donald, D. G. Lidzey, and C. Rodenburg, "Sub-nanometre resolution imaging of polymer–fullerene photovoltaic blends using energy-filtered scanning electron microscopy," Nature communications, vol. 6, pp. 1-9, 2015.

[22] S. M. George, "Introduction: heterogeneous catalysis," Chemical Reviews, vol. 95, pp. 475-476, 1995.

[23] N. A. Frey, S. Peng, K. Cheng, and S. Sun, "Magnetic nanoparticles: synthesis, functionalization, and applications in bioimaging and magnetic energy storage," Chemical Society Reviews, vol. 38, pp. 2532-2542, 2009.

[24] P. Miaudet, A. Derre, M. Maugey, C. Zakri, P. M. Piccione, R. Inoubli, and P. Poulin, "Shape and temperature memory of nanocomposites with broadened glass transition," Science, vol. 318, pp. 1294-1296, 2007.

[25] A. Tzur-Balter, Z. Shatsberg, M. Beckerman, E. Segal, and N. Artzi, "Mechanism of erosion of nanostructured porous silicon drug carriers in neoplastic tissues," Nature communications, vol. 6, p. 6208, 2015.

[26] A. V. Kabashin, M. Meunier, C. Kingston, and J. H. Luong, "Fabrication and characterization of gold nanoparticles by femtosecond laser ablation in an aqueous solution of cyclodextrins," The Journal of Physical Chemistry B, vol. 107, pp. 4527-4531, 2003.

[27] M. Chhowalla and G. A. Amaratunga, "Thin films of fullerene-like MoS 2 nanoparticles with ultra-low friction and wear," Nature, vol. 407, pp. 164-167, 2000.

[28] H. Tang, Z. Ye, L. Zhu, H. He, B. Zhao, Y. Zhang, M. Zhi, and Z. Yang, "Synthesis of radial ZnO nanostructures by a simple thermal evaporation method," Physica E: Low-dimensional systems and nanostructures, vol. 40, pp. 507-511, 2008.

[29] C. Rao, S. Vivekchand, K. Biswas, and A. Govindaraj, "Synthesis of inorganic nanomaterials," Dalton Transactions, pp. 3728-3749, 2007.

[30] K. Rajeshwar, N. R. de Tacconi, and C. Chenthamarakshan, "Semiconductor-based composite materials: preparation, properties, and performance," Chemistry of Materials, vol. 13, pp. 2765-2782, 2001.

[31] J. Zhu, O. Palchik, S. Chen, and A. Gedanken, "Microwave assisted preparation of CdSe, PbSe, and Cu2-x Se nanoparticles," The Journal of Physical Chemistry B, vol. 104, pp. 7344-7347, 2000.

[32] K. Yanagisawa and J. Ovenstone, "Crystallization of anatase from amorphous titania using the hydrothermal technique: effects of starting material and temperature," The Journal of Physical Chemistry B, vol. 103, pp. 7781-7787, 1999.

[33] Y. Wu, C. Wadia, W. Ma, B. Sadtler, and A. P. Alivisatos, "Synthesis and photovoltaic application of copper (I) sulfide nanocrystals," Nano letters, vol. 8, pp. 2551-2555, 2008.

[34] T.-L. Li, Y.-L. Lee, and H. Teng, "CuInS2 quantum dots coated with CdS as high-performance sensitizers for TiO2 electrodes in photoelectrochemical cells," Journal of Materials Chemistry, vol. 21, pp. 5089-5098, 2011.

[35] M. G. Kanatzidis, T. J. McCarthy, T. A. Tanzer, L.-H. Chen, L. Iordanidis, T. Hogan, C. R. Kannewurf, C. Uher, and B. Chen, "Synthesis and thermoelectric properties of the new ternary bismuth sulfides KBi6. 33S10 and K2Bi8S13," Chemistry of materials, vol. 8, pp. 1465-1474, 1996.

[36] X. Xu, W. Liu, Y. Kim, and J. Cho, "Nanostructured transition metal sulfides for lithium ion batteries: progress and challenges," Nano Today, vol. 9, pp. 604-630, 2014.

[37] C.-H. Lai, M.-Y. Lu, and L.-J. Chen, "Metal sulfide nanostructures: synthesis, properties and applications in energy conversion and storage," Journal of Materials Chemistry, vol. 22, pp. 19-30, 2012.

[38] D. Moore and Z. L. Wang, "Growth of anisotropic one-dimensional ZnS nanostructures," Journal of Materials Chemistry, vol. 16, pp. 3898-3905, 2006.

[39] T. Sakamoto, H. Sunamura, H. Kawaura, T. Hasegawa, T. Nakayama, and M. Aono, "Nanometer-scale switches using copper sulfide," Applied Physics Letters, vol. 82, pp. 3032-3034, 2003.

[40] C.-H. Lai, K.-W. Huang, J.-H. Cheng, C.-Y. Lee, B.-J. Hwang, and L.-J. Chen, "Direct growth of high-rate capability and high capacity copper sulfide nanowire array cathodes for lithium-ion batteries," Journal of Materials Chemistry, vol. 20, pp. 6638-6645, 2010.

[41] R. A. Sidik and A. B. Anderson, "Co9S8 as a catalyst for electroreduction of O2: quantum chemistry predictions," The journal of physical chemistry b, vol. 110, pp. 936-941, 2006.

[42] Q. Liu and J. Zhang, "A general and controllable synthesis of Co m S n (Co 9 S 8, Co 3 S 4, and Co 1− x S) hierarchical microspheres with homogeneous phases," CrystEngComm, vol. 15, pp. 5087-5092, 2013.

[43] X. Rui, H. Tan, and Q. Yan, "Nanostructured metal sulfides for energy storage," Nanoscale, vol. 6, pp. 9889-9924, 2014.

[44] W. Shi, J. Zhu, X. Rui, X. Cao, C. Chen, H. Zhang, H. H. Hng, and Q. Yan, "Controlled synthesis of carbon-coated cobalt sulfide nanostructures in oil phase with enhanced Li storage performances," ACS applied materials & interfaces, vol. 4, pp. 2999-3006, 2012.

[45] M. A. Hines and G. D. Scholes, "Colloidal PbS nanocrystals with size-tunable near-infrared emission: observation of post-synthesis self-narrowing of the particle size distribution," Advanced Materials, vol. 15, pp. 1844-1849, 2003.

[46] S. Mourdikoudis and L. M. Liz-Marzán, "Oleylamine in nanoparticle synthesis," Chemistry of Materials, vol. 25, pp. 1465-1476, 2013.

[47] R. D. Tilley and D. A. Jefferson, "The synthesis of nickel sulfide nanoparticles on graphitized carbon supports," The Journal of Physical Chemistry B, vol. 106, pp. 10895-10901, 2002.

[48] Y.-D. Li, H.-W. Liao, Y. Ding, Y.-T. Qian, L. Yang, and G.-E. Zhou, "Nonaqueous synthesis of CdS nanorod semiconductor," Chemistry of materials, vol. 10, pp. 2301-2303, 1998.

[49] T. Zhu, H. B. Wu, Y. Wang, R. Xu, and X. W. Lou, "Formation of 1D hierarchical structures composed of Ni_3S_2 nanosheets on CNTs backbone for supercapacitors and photocatalytic H_2 production," Advanced Energy Materials, vol. 2, pp. 1497-1502, 2012.

[50] W. S. Chi, J. W. Han, S. Yang, D. K. Roh, H. Lee, and J. H. Kim, "Employing electrostatic self-assembly of tailored nickel sulfide nanoparticles for quasi-solid-state dye-sensitized solar cells with Pt-free counter electrodes," Chemical Communications, vol. 48, pp. 9501-9503, 2012.

[51] G. Kullerud and R. A. Yund, "The Ni-S system and related minerals," Journal of Petrology, vol. 3, pp. 126-175, 1962.

[52] H. Li, L. Chai, X. Wang, X. Wu, G. Xi, Y. Liu, and Y. Qian, "Hydrothermal growth and morphology modification of β-NiS three-dimensional flowerlike architectures," Crystal growth & design, vol. 7, pp. 1918-1922, 2007.

[53] S. Stølen, F. Grønvold, E. F. Westrum Jr, and G. R. Kolonin, "Heat capacity and thermodynamic properties of synthetic heazlewoodite, Ni_3S_2, and of the high-temperature phase $Ni_{3\pm x}S_2$," The Journal of Chemical Thermodynamics, vol. 23, pp. 77-93, 1991.

[54] H. Zhang, G. Wu, and X. Chen, "Synthesis and magnetic properties of NiS_{1+x} nanocrystallines," Materials Letters, vol. 59, pp. 3728-3731, 2005.

[55] J. Sparks and T. Komoto, "Metal-to-semiconductor transition at the magnetic ordering temperature of NiS," Physics letters A, vol. 25, pp. 398-399, 1967.

[56] J. Trahan, R. Goodrich, and S. Watkins, "X-ray diffraction measurements on metallic and semiconducting hexagonal NiS," Physical Review B, vol. 2, p. 2859, 1970.

[57] W. Schuele and V. Deetscreek, "Appearance of a weak ferromagnetism in fine particles of antiferromagnetic materials," in Proceedings of the Seventh Conference on Magnetism and Magnetic Materials, 1962, pp. 1136-1137.

[58] J. Mellor, "A Comprehensive Treatise on Inorganic and Theoretical Chemistry," ed: The British Institute of Radiology, 1922.

[59] J. C. Bailar and A. Trotman-Dickenson, Comprehensive Inorganic Chemistry: Vol. 1: Pergamon Press, 1973.

[60] C. S. Hurlbut and C. Klein, Manual of mineralogy (after James D. Dana): Wiley, 1977.

[61] F. Hulliger, "Crystal chemistry of the chalcogenides and pnictides of the transition elements," in Structure and Bonding, ed: Springer, 1968, pp. 83-229.

[62] M. J. Buerger and B. MJ, "Crystal-structure aspects of phase transformations," 1971.

[63] W.-B. Zhang, J. Li, X.-H. Liu, and B.-Y. Tang, "Electronic structure and thermodynamic properties of millerite NiS from first principles: Complex fermi surface and large thermal expansion coefficient," Computational materials science, vol. 83, pp. 412-417, 2014.

[64] M. Upshur, B. Strick, V. McNeill, R. J. Thomson, and F. M. Geiger, "Climate-relevant physical properties of molecular constituents for isoprene-derived secondary organic aerosol material," Atmospheric Chemistry & Physics, vol. 14, 2014.

[65] K. h. Han, D. Spemann, P. Esquinazi, R. Höhne, V. Riede, and T. Butz, "Ferromagnetic spots in graphite produced by proton irradiation," Advanced Materials, vol. 15, pp. 1719-1722, 2003.

[66] T. Krogulec and Z. Galus, "On the electroreduction of thiocyanates bound to Ni (II)," Journal of Electroanalytical Chemistry and Interfacial Electrochemistry, vol. 117, pp. 109-118, 1981.

[67] M. Abboudi and A. Mosset, "Synthesis of d transition metal sulfides from amorphous dithiooxamide complexes," Journal of Solid State Chemistry, vol. 109, pp. 70-73, 1994.

[68] I. Parkin and G. Shaw, "Convenient, room-temperature liquid ammonia routes to metal chalcogenides," Journal of the Chemical Society, Dalton Transactions, pp. 231-236, 1997.

[69] A. Nezamzadeh-Ejhieh and S. Moeinirad, "Heterogeneous photocatalytic degradation of furfural using NiS-clinoptilolite zeolite," Desalination, vol. 273, pp. 248-257, 2011.

[70] M. Nath, A. Govindaraj, and C. N. R. Rao, "Simple synthesis of MoS2 and WS2 nanotubes," Advanced Materials, vol. 13, pp. 283-286, 2001.

[71] M. Salavati-Niasari, F. Davar, and H. Emadi, "Hierarchical nanostructured nickel sulfide architectures through simple hydrothermal method in the presence of thioglycolic acid," Chalcogenide Lett, vol. 7, pp. 647-655, 2010.

[72] S.-C. Han, H.-S. Kim, M.-S. Song, J.-H. Kim, H.-J. Ahn, and J.-Y. Lee, "Nickel sulfide synthesized by ball milling as an attractive cathode material for rechargeable lithium batteries," Journal of alloys and compounds, vol. 351, pp. 273-278, 2003.

[73] J. Wang, S. Y. Chew, D. Wexler, G. Wang, S. H. Ng, S. Zhong, and H.-K. Liu, "Nanostructured nickel sulfide synthesized via a polyol route as a cathode material for the rechargeable lithium battery," Electrochemistry communications, vol. 9, pp. 1877-1880, 2007.

[74] T. Takeuchi, H. Sakaebe, H. Kageyama, K. Handa, T. Sakai, and K. Tatsumi, "Modification of nickel sulfide by surface coating with TiO2 and ZrO2 for improvement of cycle capability," Journal of The Electrochemical Society, vol. 156, pp. A958-A966, 2009.

[75] K. Aso, H. Kitaura, A. Hayashi, and M. Tatsumisago, "Synthesis of nanosized nickel sulfide in high-boiling solvent for all-solid-state lithium secondary batteries," Journal of Materials Chemistry, vol. 21, pp. 2987-2990, 2011.

[76] W. S. Sheldrick and M. Wachhold, "Solventothermal synthesis of solid-state chalcogenidometalates," Angewandte Chemie International Edition in English, vol. 36, pp. 206-224, 1997.

[77] S. Sartale and C. Lokhande, "Preparation and characterization of nickel sulphide thin films using successive ionic layer adsorption and reaction (SILAR) method," Materials Chemistry and Physics, vol. 72, pp. 101-104, 2001.

[78] P. Yang, M. Lü, C. F. Song, G. Zhou, D. Xu, and D. R. Yuan, "Photoluminescence characteristics of NiS nanocrystallites embedded in sol–gel silica xerogel," Journal of Physics and Chemistry of Solids, vol. 63, pp. 2047-2051, 2002.

[79] P. Khiew, N. Huang, S. Radiman, and S. Ahmad, "Synthesis of NiS nanoparticles using a sugar-ester nonionic water-in-oil microemulsion," Materials Letters, vol. 58, pp. 762-767, 2004.

[80] Y. Hu, J.-F. Chen, H.-T. Zhang, T.-W. Li, and X. Xue, "Using silicon dioxide nanosphere gaps to confine growth of single-crystal nickel sulfide nanowires in polyacrylamide gel," Scripta materialia, vol. 55, pp. 131-134, 2006.

[81] M. Sadjadi, A. Pourahmad, S. Sohrabnezhad, and K. Zare, "Formation of NiS and CoS semiconductor nanoparticles inside mordenite-type zeolite," Materials letters, vol. 61, pp. 2923-2926, 2007.

[82] S. Sohrabnezhad, A. Pourahmad, M. Sadjadi, and M. Zanjanchi, "Growth and characterization of NiS and NiCoS nanoparticles in mordenite zeolite host," Materials Science and Engineering: C, vol. 28, pp. 202-205, 2008.

[83] P. Yang, B. Song, R. Wu, Y. Zheng, Y. Sun, and J. Jian, "Solvothermal growth of NiS single-crystalline nanorods," Journal of alloys and compounds, vol. 481, pp. 450-454, 2009.

[84] S. Nagaveena and C. Mahadevan, "Preparation by a facile method and characterization of amorphous and crystalline nickel sulfide nanophases," Journal of alloys and compounds, vol. 582, pp. 447-456, 2014.

[85] P.-F. Yin, C. Zhou, X.-Y. Han, Z.-R. Zhang, C.-H. Xia, and L.-L. Sun, "Shape and phase evolution of nickel sulfide nano/microcrystallines via a facile way," Journal of Alloys and Compounds, vol. 620, pp. 42-47, 2015.

[86] H. Bala, Y. Yu, X. Cao, and W. Fu, "Preparation and characterization of nickel/zinc sulphide: Bifunctional magnetic-optical nanocomposites," Materials Chemistry and Physics, vol. 111, pp. 50-53, 2008.
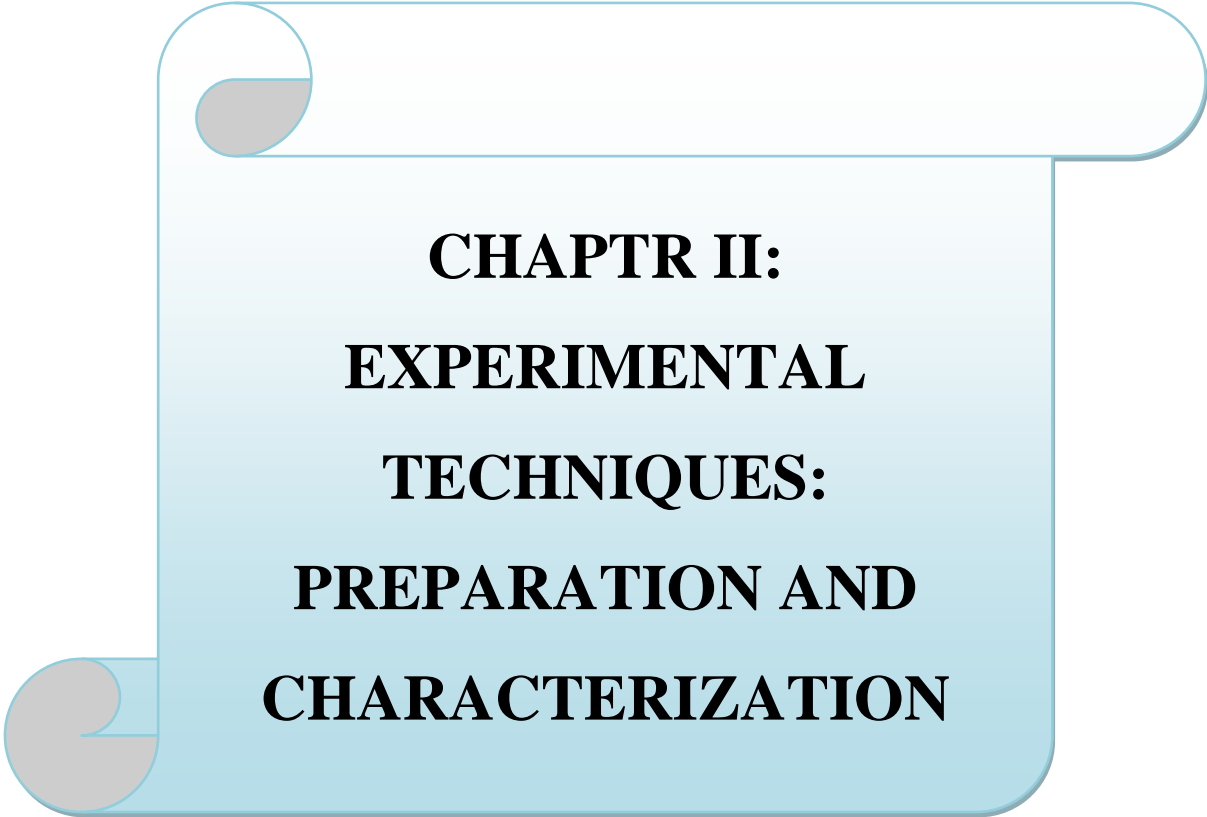
CHAPTR II:
EXPERIMENTAL
TECHNIQUES:
PREPARATION AND
CHARACTERIZATION

II.1. Introduction

Technologies based on the exploitation of the specific properties of thin films were strongly developed at the end of the 20th century. They have become one of the most important avenues of progress both in terms of theoretical understanding of the properties of condensed matter. The thin film deposition is today a key technology for many applications. In this chapter we present all the experimental steps we have carried out to elaborate NiS thin films, starting with the preparation of the experimental deposition set-up, the cleaning of the glass substrates and the preparation of the precursor solutions, then the elaboration using the pyrolysis spray system and finally the tools for the characterization of the layers obtained by the different techniques. As we know that there are many techniques for the elaboration and characterization of thin films, we will only describe the principle and the type of devices used for the characterization of thin films used in this study.

II.2. Elaboration technique for NiS films (Spray Pyrolysis)

There are different types of physical and chemical techniques for depositing thin films and these are classified in Figure II.1. The physical deposition techniques include vapor deposition like resistive heating, flash evaporation, electron beam evaporation, laser evaporation and arc evaporation and different sputtering techniques.

On the other hand the chemical deposition methods comprise of gas phase and solution phase. The gas phase includes chemical vapor deposition (CVD), laser CVD, photo (CVD), plasma enhanced CVD and metal organic chemical while liquid phase includes electro-deposition, chemical bath deposition, SILAR, anodization and spray pyrolysis method. Physical methods are expensive but give relatively more relevant and reproducible results. Physical deposition techniques lead to high quality thin films (control of roughness, crystallinity and thickness etc) with excellent properties, but these methods lack flexibility, and their deposition rate is small ($0.1 \ nmS^{-1}$).

Moreover, physical techniques generally use a vacuum which may raise a number of problems when oxides are concerned. The chemical methods are low cost and easier than

the physical methods. Among the chemical methods, spray pyrolysis is the most popular today because large numbers of conducting and semiconducting thin films can be prepared by this method. Spray pyrolysis is one of the promising methods for the production of metal oxide films [1]. In this method, different substrates like glass, ceramic, metallic etc are used for depositing thin films. Scientists have been studying the preparation of thin films by spray pyrolysis for almost three decades. The effect of various parameters on the film formation process has been studied and reviewed in the literature [1, 2].

```
                    ┌─────────────────────────────────────┐
                    │   Thin film deposition techniques    │
                    └─────────────────────────────────────┘
```

Physical deposition techniques		**Chemical deposition techniques**	
Vacuum evaporation	Sputtering	Gas phase	Solution phase
• Resistive heating	• Glow discharge DC sputtering	• Chemical vapor deposition	• Sol gel
• Flash evaporation	• Triode sputtering	• Laser chemical vapor deposition	• Spin coating
• Electron beam	• Getter sputtering	• photochemical vapor deposition	• Dip coating
• Evaporation	• Magnetron sputtering	• plasma-enhanced chemical vapor deposition	• Electrodeposition
• Laser evaporation	• Ion beam sputtering		• CBD
• Arc evaporation			• Successive ionic layer adsorption and reaction (SILLAR)
• Radio frequency (RF) heating			

Figure II.1: Classification of thin film deposition techniques

In our work, we used the pyrolysis spray technique, for the following reasons:

✓ It is an attractive method for depositing films with good uniformity and over a wide area.

✓ It is a simple technique and can be expensive.

✓ It is a method developed for metal sulphide deposition and optoelectronic applications.

II.2.1 Spray pyrolysis technique (SPT)

Spray pyrolysis is the most popular thin film deposition method because of its applicability to produce a variety of conducting, semiconducting and gas sensing metal sulfide thin films [3]. The basic principle involved in spray pyrolysis is the pyrolytic decomposition of the precursor of a compound to be deposited. When sprayed aerosols reach the surface of a hot substrate they undergo pyrolytic decomposition and the solvent evaporates in the form of vapors and forms well adherent thin films. The substrates provide thermal energy for the thermal decomposition and subsequent recombination of the constituent species, followed by sintering and crystallization of the clusters of crystallites and thereby resulting incoherent film. The thermal energy required is different for the different materials and solvents. The atomization of the spray solution into a spray depends on the geometry of the spraying nozzle, pressure and carrier gas [4].

II.2.2. Constituents of spray pyrolysis machine

The schematic diagram of the spray paralysis technique is shown in Figure II.2. It consists of mainly, (a) spray nozzle, (b) liquid level monitor, (c) hot plate with temperature controlling arrangement, (d) gas regulator valve (e) substrate, etc.

(a) Spray Nozzle: It is made up of glass and consists of the inner solution tube surrounded by the gas tube through which carrier gas flows. With the application of pressure to the carrier gas, a vacuum is created at the tip of the nozzle and the solution is automatically sucked and the spray starts.

(b) Liquid Level Monitor: The spray rate, at a fixed pressure, depends on the height of the solution, measured with reference to the tip of the nozzle and the arrangement for the change in height of the solution, forms liquid level monitor.

(c) Hot Plate: The iron disc, with diameter 20 cm and thickness 1 cm, was supported on the electric heater. A maximum temperature up to 600°C can be obtained with this arrangement. Chromel-alumel thermo-couple was used to measure a temperature of the substrates and is fixed at the center of the iron disc. The temperature of the hot plate was monitored with temperature controller.

(d) Gas Regulator Valve: The gas regulator valve was used to control the pressure of the gas. A coming glass tube of length 25cm and a diameter of 1.5cm were converted into a gas flow meter.
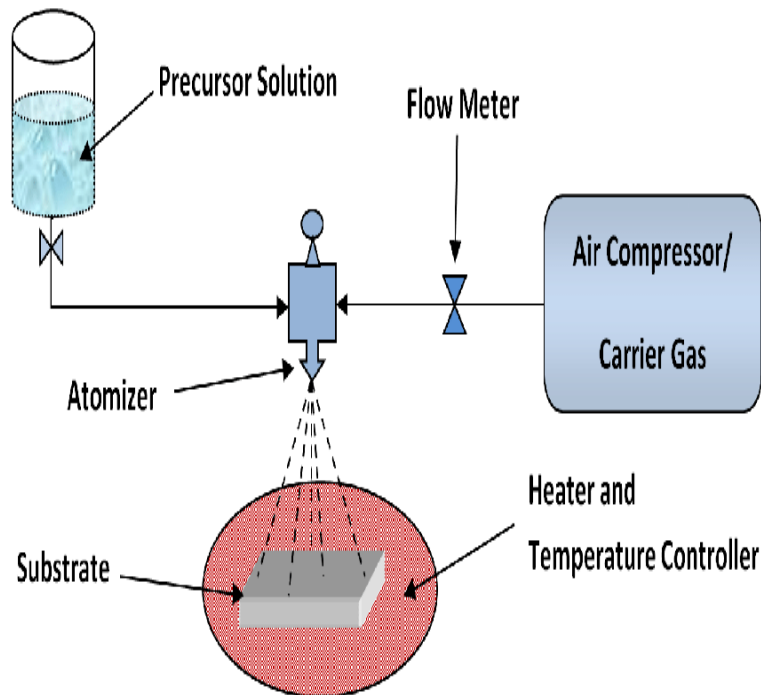
Figure II.2: Schematic representation of spray pyrolysis machine

II.2.3. Critical spray parameters of SPT

Substrate Temperature: The substrate temperature is the most important deposition parameter. At temperatures below 2000C, the droplets deposited are still rich in solvent. This large amount of unreacted precursor solution on the glass plate results in a powdery deposit. Quick drying of this layer results in stresses and subsequent cracking. At very high temperatures (>3500℃), the deposited spray droplets have a very high chance of re-evaporation. Therefore discrete particles are formed on the surface due to slow spreading which gives rise to porous films. This increases the surface roughness. The number of particles on the surface increases with increasing deposition temperature.

Spray Rate: Spray rate is another important parameter that influences the property of films formed. It has been reported that properties like crystallinity, surface morphology, resistivity and thickness are affected by changes in spray rate. It is generally observed that a smaller spray rate favors the formation of better crystalline films. Smaller spray rate

requires higher deposition time obtaining films of the same thickness prepared to higher spray rate. The surface morphology of the films varies with the spray rate. Higher spray rate results in rough films. Also, it is reported that films deposited at smaller spray rates are thinner due to the higher re-evaporation rate.

Precursor Solutions: Precursor solution plays a vital role in the formation of thin films of various compounds. The true solutions, colloidal dispersions, emulsions and sols can be used as aerosol precursors. Aqueous solutions are usually used due to ease of handling safety, low cost and availability of a wide range of water soluble metal salts. The solute must have high solubility, which increases the yield of the process.

Nature of Precursor Solution: Precursors used for spraying is also very important and it affects the film properties to a great extent. Solvent, type of salt, concentration and additives or dopants influence the physical and chemical properties of the films. Usually, de-ionized water which is ideal for a low cost process is used a solvent. The concentration of the precursor solution determines the duration of spraying needed to obtain a uniform film deposition. A low concentration means lengthy spray duration. Higher concentration requires comparatively less spray time, but it can lead to rough and grainy films. Usually the concentration ranges from 0.001 M to 0.1M and it is seen that smooth films are obtained at low concentrations.

Angle and height of spray head: This parameter is also important because it can also influence the properties of deposited films. Each nozzle has a spraying angle. Therefore, the nozzle-substrate distance determines the area coated and deposition rate. The smaller distance between the atomizer and the substrate, to be related to the higher deposition rate and smaller the coated area. Different types of spray heads with different angles produce different spray patterns. The height and angle of the spray head should ensure maximum uniformity and a large area of coverage. In the pressurized spray pyrolysis setup, where the precursor solution is atomized using an air stream there are also other limitations. In this case the minimal nozzle-substrate distance is not limited by the substrate size, but by the cooling effect of air flow. At small distances pronounced cooling of the substrate occurs. Simultaneously, more heat is required from the heating plate, because the droplet mass flow density increases with decreasing distance. A pressure, or

air blast, atomizer uses high speed air in order to generate an aerosol from a precursor solution. Increasing the air pressure causes a direct decrease in the generated mean droplet diameter. Inversely, increasing liquid pressure causes a direct increase in the mean droplet diameter. Perednis showed that all droplets sprayed from an air blast atomizer are contained within a 70° angle spray cone angle, while half are within a narrower 12° angle. It was also determined that the flow rate has a very small influence on the spray characteristics, which can be mostly ignored for modeling.

II.2.4. Scheme of pyrolysis and formation of thin films

In spray pyrolysis, the precursor solution is atomized through a nozzle.

The nozzle converts the solution into small droplets, known as aerosols. These aerosols are allowed to incident onto the preheated substrates. The pyrolytic decomposition of the aerosols depends on the substrate temperature. The formation of thin films with desired properties is possible only at optimum substrate temperature. Various steps during pyrolysis of aerosols are depicted in Figure II.3 and summarized in this section [5]:

1) In the first step, an aqueous precursor solution is converted into aerosols by a spray nozzle.

2) Solvent evaporation takes place in the second step.

3) In this step, the vaporization of the solvent leads to the precipitate formation as the droplets / aerosol approaches the substrate.

4) Pyrolysis of the precipitate occurs in succession before the precipitate reaches the substrate; this constitutes step 4.

5) In step 5, when the precipitate reaches the substrate, nucleation and growth of metal oxide thin films on the substrate surface take place.

6) Finally, the growth of the nuclei leads to the formation of a continuous thin layer of metal oxide (step 6).
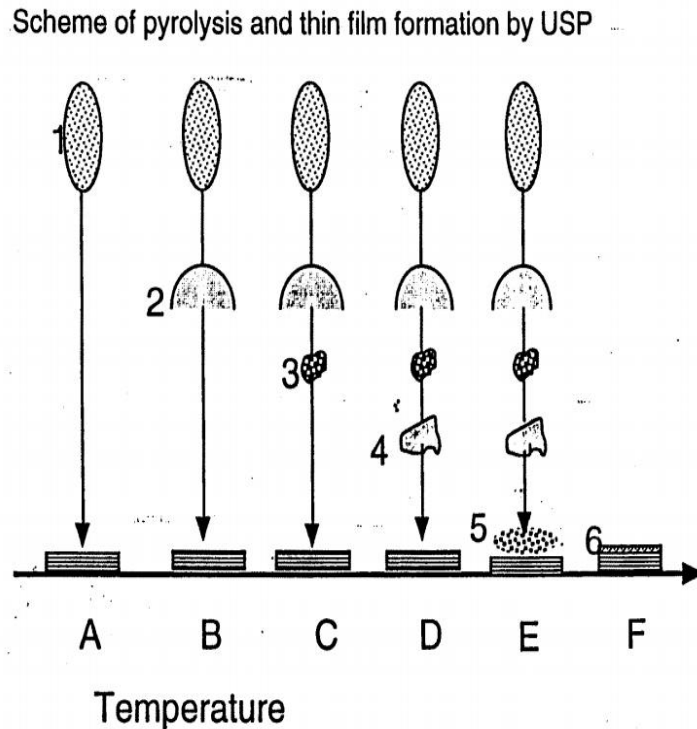
Figure II.3: Scheme of pyrolysis and thin film formation by the spray pyrolysis technique

1. Aerosol of aqueous solution

2. Solvent evaporation

3. Precipitate

4. Pyrolysis of the precipitate

5. Nucleation and growth of thin film

6. Formation of continuous thin layer

II.2.5. Factors affecting the spray pyrolysis

Thin film formation by spray pyrolysis depends upon the following factors

➢ The pressure of carrier gas and geometry of the spray nozzle affects the droplets size and thin film properties.

➢ The solution concentration, substrate material, substrate temperature, spray rate and cooling rate also affect the thin film properties.

➢ The film thickness can be changed by changing the solution concentration, quantity, substrate temperature and distance between the nozzle and substrate.

II.2.6. Substrate cleaning

Substrate cleaning is the process of breaking bonds between substrates and contaminants without damaging the substrates. In thin film deposition process substrate cleaning is an important factor to get reproducible films as it affects the smoothness uniformity, adherence and porosity of the films. The substrate cleaning process depends upon the nature of the substrate; the degree of cleanliness required and nature of contaminants to be removed. The common contaminates are grease, adsorbed water, air borne dust, lint, oil particles etc. The micro slides supplied by Blue Star of dimensions 7.5 cm x 2.2 cm x 0.1 cm have been used as substrates. The following process has been adopted for cleaning of substrates:

1. The substrates were washed with the detergent solution 'Labolene' and then with water.
2. These substrates were boiled in chromic acid for five minutes.
3. Substrates were cleaned with double distilled water.
4. These substrates were kept in NaOH solution to remove the acidic contaminations.
5. The substrates were again washed with distilled water and cleaned ultrasonically.
6. Finally substrates were dried in alcohol vapors.

II.2.7. Advantages and Disadvantages of spray pyrolysis method

In comparison with other thin film deposition techniques, spray pyrolysis has many advantages including:

➢   **advantages of thin films**
- It offers an extremely easy way to dope films with virtually any element in any proportion, by merely adding it in some form to the spray solution.
- Unlike the closed vapor deposition method, spray paralysis does not require high quality targets and / or substrates nor do it require vacuum at any stage, which is a great advantage if the technique is to be scaled up for industrial applications.
- The deposition rate and the thickness of the films can be easily controlled over a wide range by changing the spray parameters, thus eliminating the major

drawbacks of chemical methods such as sol-gel which produce films of limited thickness.

- Operating at moderate temperatures (100-500°C), spray paralysis can produce films on less robust materials.

- Unlike high-power methods such as radiofrequency magnetron sputtering (RFMS), it does not because local over-heating that can be detrimental for materials to be deposited. There are virtually no restrictions on the substrate material, dimension its surface profile.

- By changing composition of the spray solution during the spray process, it can be used to make layered films and films having the composition gradients throughout the thickness.

- It is believed that reliable fundamental kinetic data are more likely to be obtained on particularly well-characterized film surfaces, provided the films are quite compact, uniform and that no side effects from the substrates occur. Spray paralysis offers such an opportunity.

- A major advantage of this method is operating at moderate temperature (100-50000 C), and can produce films on less robust materials. By changing the composition of the spray solution during the spray process, it can be used to make layered films and films having composition gradients throughout the thickness.

  ➢ **Disadvantages of thin films**

- Non-uniformity of film with larger grain size due to uncontrollable spray droplet size
- Wastage of solution i.e. the low ratio of atoms effectively deposited to those supplied
- Low deposition rate.

II.3. Characterization techniques for NiS films

After preparation of (NiS) thin films by spray pyrolysis method on a glass substrate, it is necessary to confirm their phase formation temperature and to evaluate their structural, elemental, functional, morphological and electrical properties. This is done by using the following techniques.

1. X-ray diffraction (XRD)

2. Scanning electron microscopy (SEM)

3. Energy dispersive X-ray (EDX)

4. Atomic force microscopy (AFM)

5. Fourier transform infrared spectroscopy (FT-IR)

6. UV-Visible Spectroscopy

7. DC conductivity measurements (four points)

8. AC impedance measurements

The details of these techniques are discussed in the following sections.

II.3.1. X-ray diffraction (XRD)

XRD is one of the oldest and effective tools for understanding structure of crystalline materials. It provides extensive information about the crystal structure. X-rays are electromagnetic waves with wavelength between 1-100Å. The wavelength of an X-ray is thus of the same order of magnitude as the lattice constant of crystals. When X-rays are incident on a crystal surface, they are reflected from it [6].
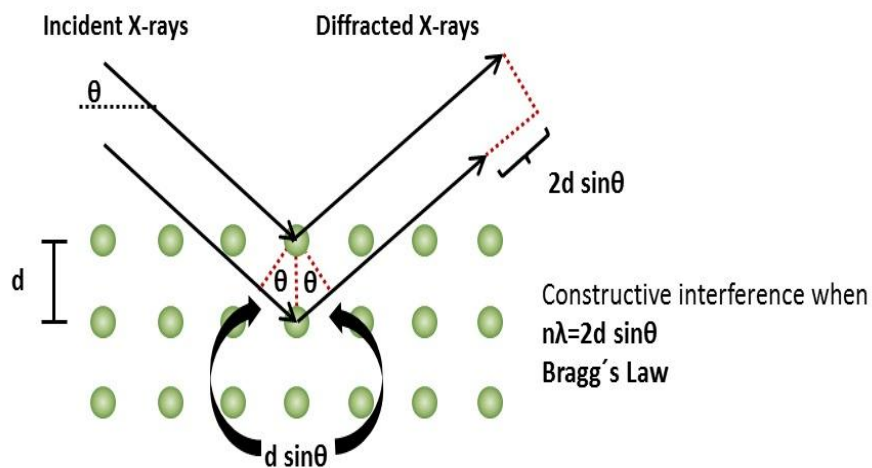
Figure II.4: Schematic diagram of X-ray diffraction process.

The reflection obeys the following Bragg's law.

$$2d \sin\theta = n\lambda \ldots\ldots\ldots\ldots\ldots\ldots..(II.1)$$

where d is the distance between crystal planes, θ is the incident angle of X-ray, λ is the wavelength of the X-ray and n is a positive integer. Bragg's law also suggests that diffraction is only possible when λ< 2d.

XRD is the most specific technique for studying the crystal structure of solids. Generally, it does not require any elaborate sample preparation and is essentially nondestructive to samples [7]. XRD is a suitable tool to determine the crystal structure of any unknown materials, whether the sample is a single crystal or polycrystals [6], either with a random distribution of orientations or with a preferred orientation with respect to the film plane. Thicknesses of surface thin films are about 1000Å and those can be investigated using XRD [8]. Thicker films can be characterized by reflection high-energy electron diffraction (RHEED). Analysis of the diffraction patterns obtained by these techniques and comparison with standard ASTM data can reveal the existence of different crystallographic phases in the film, their relative abundance, the lattice parameters, and any preferred orientations.

II.3.2. Scanning Electron Microscopy (SEM)

Scanning electron microscopy SEM is a type of microscope that form images of the sample surface by scanning it with a high-energy beam of electrons in a raster scan pattern. It is a powerful microscope that uses electrons rather than light to form an image of objects such as fractured metal components, foreign particles and residues, polymers, thin films electronic components, biological samples, and countless others. The shorter wavelength of electrons permits image magnifications of up to 100,000X, as compared to about 2,000X for conventional light microscopy. An SEM also provides a greater depth of field than a light microscope, allowing complex, three-dimensional objects to remain sharp and in focus. In a typical SEM, an electron beam is thermoionically emitted from an electron gun fitted with a tungsten filament cathode. Other types of electron emitters include lanthanum hexaboride cathodes, which can be used in a standard tungsten filament SEM. if the vacuum system is upgraded. Field emission guns (FEG) of the cold-cathode type using tungsten single crystal emitters or the thermally-assisted Schottky type, using emitters of zirconium oxide can also be used. The electron beam, which typically has an energy ranging from a few hundred eV to 40 keV, is focused by one or two condenser lenses to a

spot about 0.4 nm to 5 nm in diameter. The beam passes through pairs of scanning coils or pairs of deflector plates in the electron column, typically in the final lens, which deflect the beam in the x and y axes so that it scans in a raster fashion over a rectangular area of the sample surface. The size of the interaction volume depends on the electron's landing energy, the atomic number of the specimen and the specimen's density. The energy exchange between the electron beam and the sample results in the reflection of high-energy electrons by elastic scattering, emission of secondary electrons by inelastic scattering and the emission of electromagnetic radiation, each of which can be detected by specialized detectors. The beam current absorbed by the specimen can also be detected and used to create images of the 42 distribution of specimen current. Electronic amplifiers of various types are used to amplify the signals which are displayed as variations in brightness on a cathode ray tube. The raster scanning of the CRT display is synchronized with that of the beam on the specimen in the microscope, and the resulting image is therefore a distribution map of the intensity of the signal being emitted from the scanned area of the specimen. The image may be captured by photography from a high resolution cathode ray tube, but in modern machines is digitally captured and displayed on a computer monitor and saved to a computer's hard disc [9].

Figure II.5: Scanning electron microscope with EDS set up

In this work, a thermal field emission gun scanning electron microscope (FEG-SEM) of model JEOL JSM-7600F is used (Figure II.5). It has an ultrahigh resolution for fine surface morphology of nanostructures (secondary electron image resolution 1.0 nm at 15 kV). It contains built-in r-filter enabling user selectable mixture of the secondary electron (SE) and backscattered electron (BSE) images. It has Gentle Beam (GB) mode for accelerating voltage in kV, top-surface imaging, reduced beam damage and charge suppression allows examination of charging specimens without additional coating. New low-angle backscattered electrons detector allows imaging of specimens at extremely low accelerating voltage (kV) with high spatial resolution. Scanning transmission electron microscopy detector allows both 43 bright-field and dark-field imaging of thin, electron transparent samples with sub 0.8 nm resolution. For EDS this field emission SEM (FESEM) set up is connected to an Aztec Synergy system (Oxford AZtec energy/AZtec HKL) with X-MAX50 silicon drift detector which provides high counts rate and allows Nanoanalysis, Mapping, and Crystal Orientation.

II.3.3. Energy dispersive spectroscopy (EDS)

EDS is an analytical technique used for the chemical characterization of a sample. It is one of the variants of X-ray fluorescence (XRF) analysis. As a type of spectroscopy, it relies on the investigation of a sample through interactions between electromagnetic radiation and matter, analyzing X-rays emitted by the matter in response to being hit with charged particles. Its characterization capabilities are due in large part to the fundamental principle that each element has a unique atomic structure allowing x-rays that are characteristic of an element's atomic structure to be identified uniquely from each other. To stimulate the emission of characteristic X-rays from a specimen, a high energy beam of charged particles such as electrons or protons (see PIXE), or a beam of X-rays, is focused on the sample being studied. At rest, an atom within the sample contains ground state (or unexcited) electrons in discrete energy levels or electron shells bound to the nucleus. The incident beam may excite an electron in an inner shell, ejecting it from the shell while creating an electron hole where the electron was. An electron from an outer, higher-energy 44 shell then fills the hole, and the difference in energy between the higher-energy shell and the lower energy shell may be released in the form of an X-ray. The number and energy of the X-rays emitted from a specimen can be measured by an EDS. As the energy

of the X-rays are characteristic of the difference in energy between the two shells, and of the atomic structure of the element from which they were emitted, this allows the elemental composition of the specimen to be measured [10] .

II.3.4. Atomic Force Microscope (AFM)

AFM is a very high resolution type of scanning probe microscopy; its optical diffraction limit is 1000 times better. The AFM is one of the most important equipment for imaging the material at the nanoscale. The information on surface morphology is gathered by scanning the surface with the mechanical probe. The mechanical probe is made from piezoelectric element so it gives very accurate and precise movement on (electronic) command. In some variation, electric potential can also be scanned using conducting cantilevers. In more advanced versions, currents can be passed through the tip to probe the electrical conductivity or transport the underlying surface. Traditionally, the sample is mounted on a piezoelectric tube, that can move the sample in the Z-direction for maintaining a constant force and the X and Y direction for scanning the sample. Alternatively, a 'tripod' configuration of three piezocrystal is also used to scan X, Y and Z directions. This eliminates the distortion effect of the tube scanning system [11].
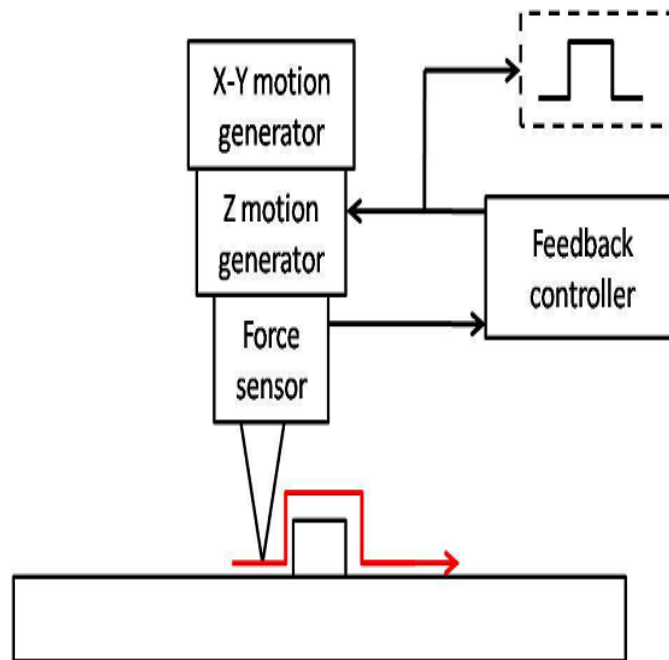
Figure II.6: Basic block diagram of an AFM
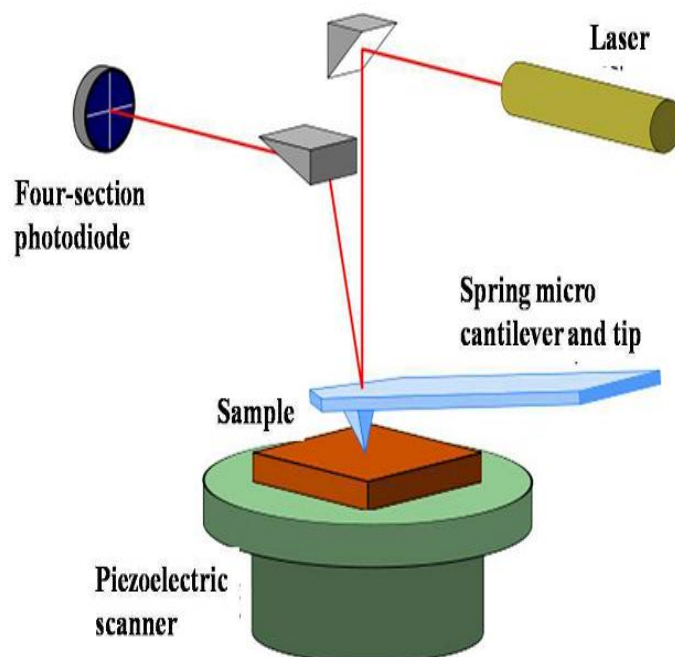
Figure II.7: Illumination of light lever force sensor

II.3.5. Infrared spectrometers (FTIR)

Fourier-transform infrared spectroscopy (or FTIR, for short) is a method of exploring the physical properties of solids, liquids, and gases. More specifically, it allows the study of the absorptive and emissive properties of materials. The choice of IR wavelengths in FTIR method is particularly useful for studying chemical bonds that connect atoms. It turns out that these bonds tend to vibrate with frequencies that correspond to infrared-wavelength light, and hence can easily be excited with such radiation. Commonly, IR wavelength spectroscopy covers wavenumbers ranging from 400 to 4000 cm^{-1} [12].

Thin layers, usually powders, require a special preparation, which consists of intimately grinding a few tens of mg of KBr (1 mg of solid in 100 mg of KBr, note that potassium bromide does not absorb in the infrared). The mixture, which must be as homogeneous as possible, is placed in a mold and pressed under vacuum at high pressure so as to obtain pellets that are as transparent as possible to IR radiation. The pellet is placed on a sample holder and subjected to a beam of infrared radiation (of hv energy), the interaction of which with a substance leads to excited vibrational states of the molecules, reflected by the appearance of a signal or absorption band.

> **Operation of the FTIR spectrometer.**

An FT-IR spectrometer consists essentially of five parts (Figure II. 6):

1. A light source.

2. A device to generate interference.

3. A sample compartment that can accommodate several types of accessories (sample holder) depending on the measurement mode used (reflection or transmission).

4. A photosensitive detector or sensor: the FTIR spectrometer may include one or more or several detectors, which may be of the type :

> Pyroelectric (generating a current proportional to the temperature differential between the 2 faces of the detector) such as DTGS (Deuterated Tri-glycine Sulphate Detectors),

> Photoelectric (generating a potential difference by the absorption of photons) such as MCT (Mercury Cadmium Tellurium) detectors, which consist of a single crystal made of a mercury-cadmium-tellurium alloy deposited on an inert support.

5. Finally, the analog-to-digital converter interrogates the detector at regular intervals and transforms the analog signal into a digital signal that can be manipulated by the computer system.
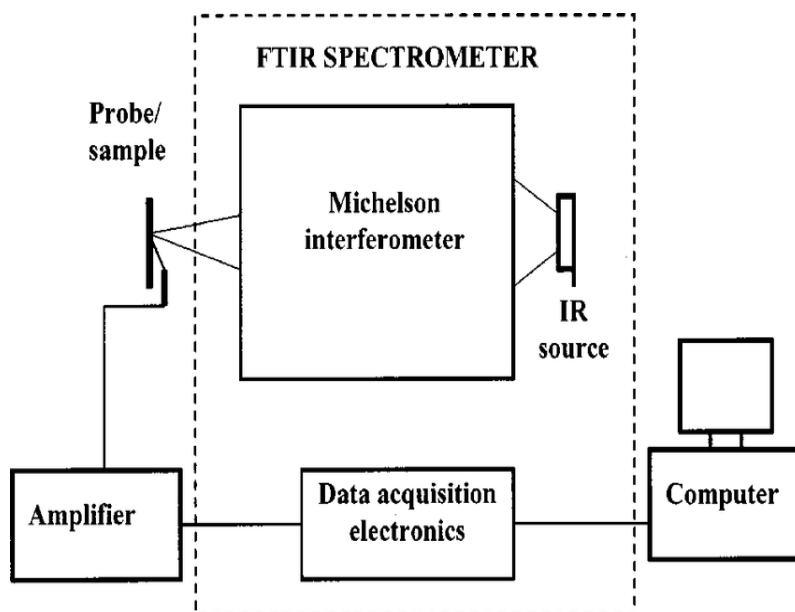
Figure II.8: Schematic diagram of an FTIR spectrometer.

> ➢ **FTIR Spectrum Generation**

The sample spectrum generation process consists of 4 steps.

1. Recording of a single-beam reference interferogram on the carrier medium sample.
2. Recording of a single-beam interferogram of the sample.
3. Inverse Fourier Transform of interferograms and post-Fourier operations.
4. Calculation of the absorbance (or transmittance) spectrum from the single-beam spectra.

II.3.6. UV-Visible Spectroscopy

In this work a dual-beam UV-Visible of the spectrophotometer is used and a schematic diagram of the dual-beam UV-Visible of the spectrophotometer is given in Figure II.9. The functioning of this instrument is relatively straightforward. A beam of light from a visible and/or UV light source is separated into its component wavelengths by a prism or diffraction grating. Each monochromatic (single wavelength) beam in turn is split into two equal intensity beams by a half-mirrored device. One beam, the sample beam (colored magenta), passes through a small transparent container (cuvette) containing a solution of the compound being studied in a transparent solvent. The other beam, the reference (colored blue), passes through an identical cuvette containing only the solvent. The intensities of these light beams are then measured by electronic detectors and compared. The intensity of the reference beam, which should have suffered little or no light absorption, is defined as I0. The intensity of the sample beam is defined as I. Over a short period of time, the spectrometer automatically scans all the component wavelengths in the manner described. The ultraviolet (UV) region scanned is normally from 200 to 400 nm, and the visible portion is from 400 to 800 nm [13].
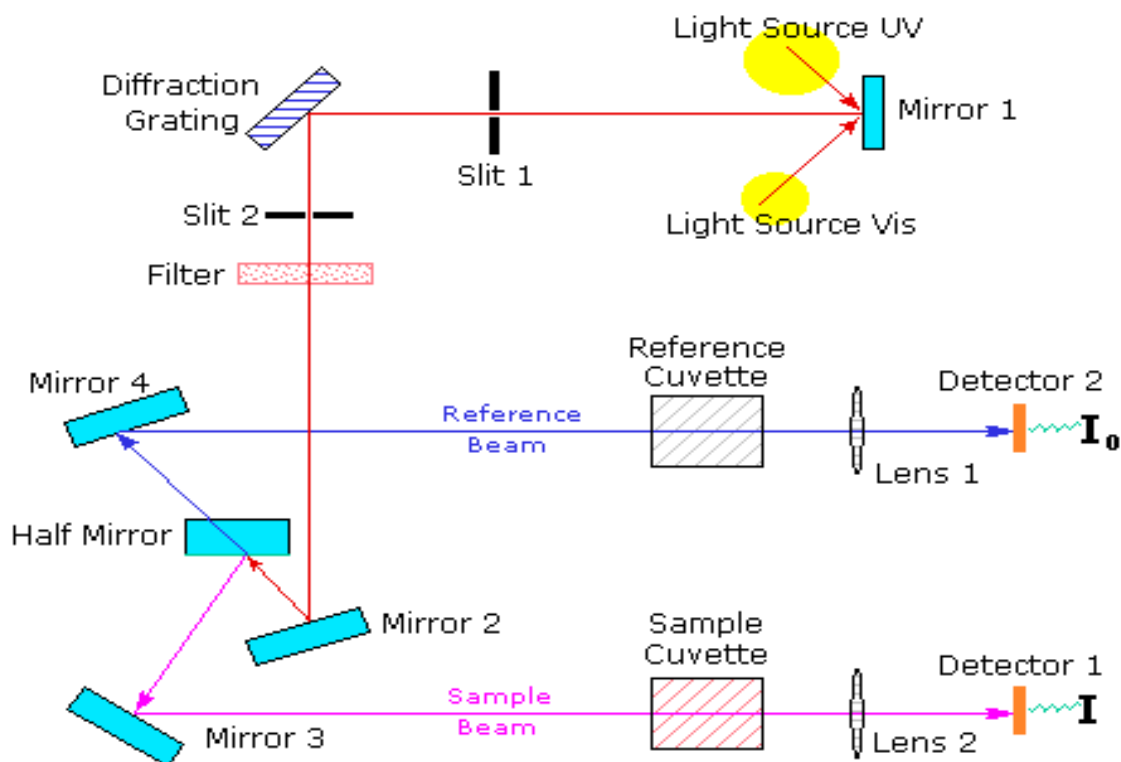
Figure II.9: Schematic diagram of the spectrophotometer [13].

If the sample compound does not absorb light of a given wavelength, $I = I_0$. However, if the sample compound absorbs light then I is less than I0, and this difference may be plotted on a graph versus wavelength, as shown on the right. Absorption may be presented as transmittance or absorbance. If no absorption has occurred, $T = 1.0$ and $A = 0$. Most of the sample compound does not absorb light of a given wavelength, $I = I0$. However, if the sample compound absorbs light then I is less than I0, and this difference may be plotted on a graph versus wavelength, as shown on the right. Absorption may be presented as transmittance or absorbance. If no absorption has occurred, $T = 1.0$ and $A = 0$. Most spectrometers display absorbance on the vertical axis, and the commonly observed range is from 0 (100% transmittance) to 2 (1% transmittance). The wavelength of maximum absorbance is a characteristic value, designated as λmax.

Different compounds may have very different absorption maxima and absorbances. Intensely absorbing compounds must be examined in dilute solution, so that significant light energy is received by the detector, and this requires the use of completely transparent (non-absorbing) solvents. The most commonly used solvents are water, ethanol, hexane and cyclohexane.

II.3.7. Electrical conductivity measurement

The tendency of a material is to resist the flow of an electrical current through it and to convert the electrical energy into heat energy is called resistance. According to Ohm's law:

$$R = \frac{V}{I} \dots \dots (II.2)$$

where R is the resistance of a material, V is the potential difference and I is the current flow through the material. The resistance per unit length of the unit cross section is called resistivity. It is denoted by ρ and mathematically defined as [14]:

$$\rho = \frac{RA}{L} \dots \dots (II.3)$$

where A is the cross-sectional area and L is the length. The electrical conductivity of a material is reciprocal of the resistivity of the material. It is denoted by σ and mathematically defined as:

$$\sigma = \frac{1}{\rho} \dots \dots (II.4)$$

Resistivity is an intrinsic property of a material and depends only on the crystal structure of the material. The resistivity can be obtained by measuring the resistance of a specimen of the material with well-defined regular geometric shape. There are many methods to measure resistivity. Some of them have been discussed below.

There are four methods commonly used for the measurement of resistivity.

1. Direct method
2. Two point probe method
3. Four point probe method
4. Van der Pauw method

➤ **Four-Probe technique**

Four-probe method is usually used for the determination of low resistivity. For this purpose four metal pins at an equal distance D are pressed by springs against the semiconductor sample as shown in Figure II.10. If the outside pins carry a current of

intensity I, a voltage drop is measured between the inner probes of magnitude V. Assuming the sample to be much thicker than the pin distance D, the resistivity ρ is given by [15].

$$\rho = \frac{2\pi DV}{I} \ldots \ldots \ldots (II.5)$$

The effect of the contact resistance is avoided in Four-probe method.
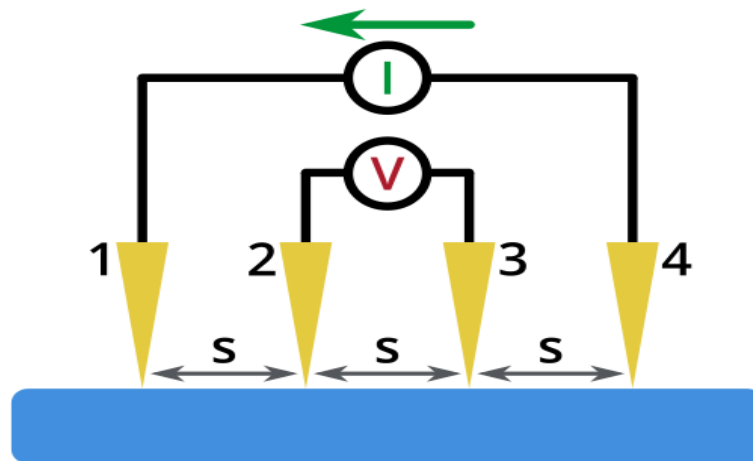
Figure II.10: Circuit arrangement of four probe method

II.3.8. Complex Impedance Spectroscopy

Complex impedance spectroscopy was first applied to solid electrolytes in the late 1960s by J. Bauerle [16]. Obtaining the electrochemical characteristics of the system is based on the point-by-point analysis of the response of the alternating current as a function of the frequency of the excitation signal.

➢ **Principle**

The technique of complex impedance spectroscopy consists of characterizing the response of an electrochemical system to a sinusoidal voltage of variable frequency. It is thus possible to separate physical phenomena. For example, the phenomenon of electrode polarization will occur at a lower frequency (µHz) than the movement of ions (MHz), which in turn will occur at a lower frequency than the movement of electrons (GHz). The use of alternating current and sufficiently high frequencies also avoids the problems of overvoltage's that can be caused by electrode polarization when measuring with DC polarization. This technique makes it possible to measure the impedance of an

electrochemical system and thus the resistance of the constituent material. Especially in ion conductors, the analysis of impedance spectra can provide information on the dynamics of the charge carriers [17, 18].

Fig II.11: GWINSTEK impedance meter, LCR- 821.

I.4. Conclusion

This chapter intends to deal with thin film preparation techniques. Thus we attempted to give a detailed explanation of the spray pyrolysis technique (components of the device, solution preparation method, how to find the optimal conditions for the preparation of the desired films from (solution flow, substrate temperature, solution concentration,…….. etc). Spray pyrolysis technology is also the most used method for depositing metals, alloys and many compounds, due to the ease of use of the device. It is inexpensive and effective. In the second part of this chapter, we described the different characterization of used techniques to analyze and quantify the different optical, structural, morphological and electrical properties of the produced films.

Reference

[1]   A. Jäger-Waldau, "Progress in chalcopyrite compound semiconductor research for photovoltaic applications and transfer of results into actual solar cell production," in Practical Handbook of Photovoltaics, ed: Elsevier, 2012, pp. 373-395.

[2]   M. B. Father, "Late Asaram Mahadu Patil and My Father in Law Late Hindurao Pandurang Patil," BHARATI VIDYAPEETH UNIVERSITY PUNE, 2015.

[3]   A. Moholkar, S. Pawar, K. Y. Rajpure, S. N. Almari, P. Patil, and C. Bhosale, "Solvent-dependent growth of sprayed FTO thin films with mat-like morphology," Solar Energy Materials and Solar Cells, vol. 92, pp. 1439-1444, 2008.

[4]   G. Korotcenkov, "Gas response control through structural and chemical modification of metal oxide films: state of the art and approaches," Sensors and Actuators B: Chemical, vol. 107, pp. 209-232, 2005.

[5]   J. Viguie and J. Spitz, "Chemical vapor deposition at low temperatures," J. Electrochem. Soc, vol. 122, pp. 585-588, 1975.

[6]   S. J. Kang, Y. H. Joung, H. H. Shin, and Y. S. Yoon, "Effect of substrate temperature on structural, optical and electrical properties of ZnO thin films deposited by pulsed laser deposition," Journal of Materials Science: Materials in Electronics, vol. 19, pp. 1073-1078, 2008.

[7]   R. Howland and L. Benatar, "Park scientific instruments," A practical guide to scanning probe microscopy. Park scientific instruments, 1996.

[8]   P. Kumar, A. Misra, D. Kumar, N. Dhama, T. Sharma, and P. Dixit, "Structural and optical properties of vacuum evaporated CdxZn1− xS thin films," Optical Materials, vol. 27, pp. 261-264, 2004.

[9]   A. H. Rubel, "Synthesis and characterization of spray pyrolised al-doped Cds thin films," 2011.

[10] M. Taskin, "Structural, optical and electrical properties of cobalt doped zinc oxide thin films prepared by spray pyrolysis," 2011.

[11] G. Haugstad, Atomic force microscopy: understanding basic modes and advanced applications: John Wiley & Sons, 2012.

[12] A. A. Ismail, F. R. van de Voort, and J. Sedman, "Fourier transform infrared spectroscopy: principles and applications," in Techniques and instrumentation in analytical chemistry. vol. 18, ed: Elsevier, 1997, pp. 93-139.

[13] T. Ahmmed, "Investigation of structural, optical and electrical properties of zinc selenide thin films prepared by chemical bath deposition technique," 2017.

[14] K. Alam, "Study of structural, optical and electrical properties of Zn1-xMnxO thin films deposited by spray pyrolysis technique," 2012.

[15] Y. Zhang, J.-K. Kim, C.-S. Park, and D.-W. Lee, "An investigation of electrical transport properties through a monolithic square-configured micro-four-point probe with ultra-sharp tips," Sensors and Actuators A: Physical, vol. 166, pp. 247-250, 2011.

[16] C. Deportes, M. Duclot, P. Fabry, J. Fouletier, A. Hammou, M. Kleitz, E. Siebert, and J. Souquet, "Electrochimie des solides, Collection Grenoble Sciences," France: Presses Universitaires de Grenoble, 1994.

[17] J. R. Macdonald, "Impedance spectroscopy," Annals of biomedical engineering, vol. 20, pp. 289-305, 1992.

[18] K. Darowicki, "Linearization in impedance measurements," Electrochimica acta, vol. 42, pp. 1781-1788, 1997.
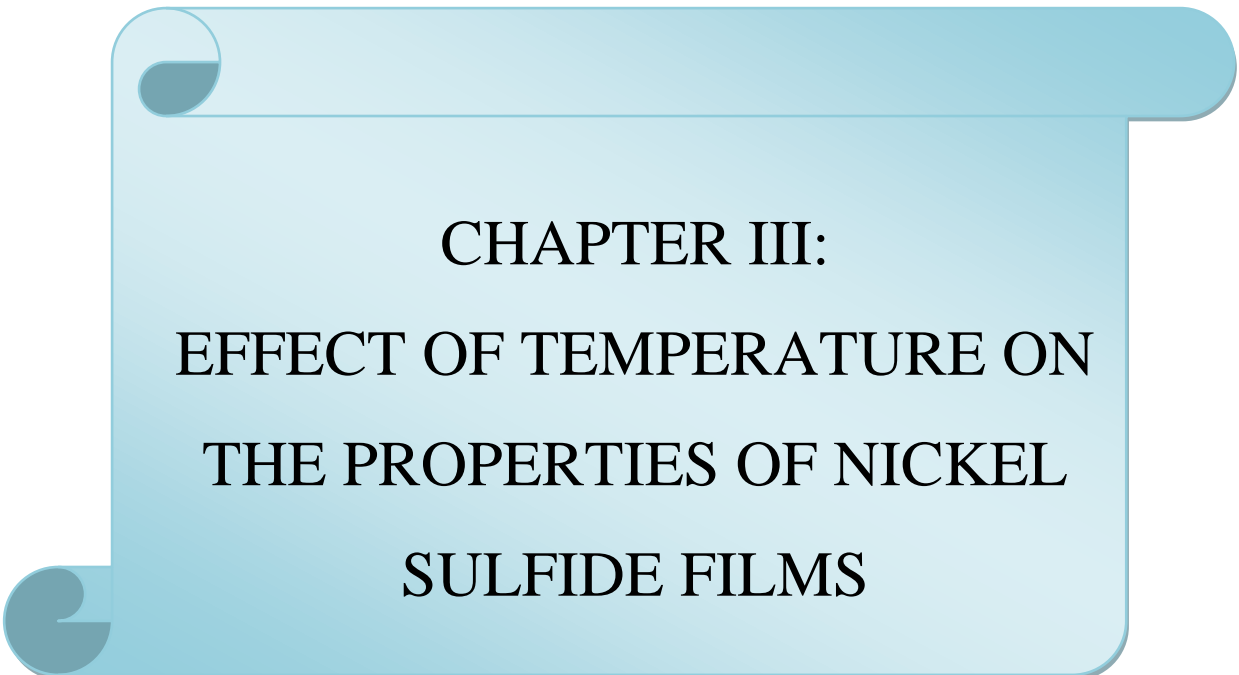
CHAPTER III:

EFFECT OF TEMPERATURE ON THE PROPERTIES OF NICKEL SULFIDE FILMS

III.1. Introduction

The mean object of this research is to study the synthesis of new nickel sulfide thin film by spray technique at different substrate temperatures. These materials can be used as a promising co-catalyst to improve the photocatalytic performance or superconductivity. In this research can be studied the physical properties such as the structural, morphological, optical and electrical characterizations. The effort of this study can be needed to optimize film properties in future investigations. Balayeva et al. [1] prepared nickel sulfide (NiS and Ni_3S_4) nanostructures at different sulfur sources like thiourea and sodium sulfide. However, Shinde et al. [2] investigated the sulfur Source-Inspired Self-Grown 3D Ni_xS_y Nanostructures and their electrochemical supercapacitors by hydrothermal method. Based on the past year, the nickel sulfide thin films can be deposited by various methods such as laser ablation (NiS) [3], successive ionic layer adsorption reaction (SILAR) technique [4], soft solution-processing (Ni_3S_2, NiS_2, and Ni_3S_4) [5], hydrothermal method (Ni_3S_2, NiS) [6] chemical vapor deposition (AACVD) method (NiS and $Ni_{17}S_{18}$) [7], and spray pyrolysis [8]. However, the deposition of nickel sulfide thin films by spray ultrasonic technique has yielded the best results, which is used in this work.

III.2. Material and method

III.2.1. Preparation of thin films

In this work, chloride nickel dehydrates 10^{-2}M ($NiCl_2$, $2H_2O$), and thiourea 2.10^{-2} M ($S=C(NH_2)_2$)) were used as precursors to prepare the nickel sulfide thin films. It was obtained from two solutions with different molarities; the mixture ([S]/[Ni]=2) was stirred for 3 hours at room temperature. The final solution was placed to the heater at 70 °C, in this setup, can be added drops of HCl solution as a stabilized (36%) to the mixture solution

as a stabilized with heating. After this setup, the nickel sulfide solution becomes transparent and clear. The nickel sulfide thin films were performed on glass substrates (2x7 cm^2) by spray pyrolysis method with heating at different substrate temperatures (523, 573 and 623 K). The distance between the substrates and the spray nozzle was fixed at 3.5 cm. The solution and carrier gas flow rate was 4 ml/min, in all cases. We have used Nitrogen gas to avoid chemisorptions of oxygen to obtain the sulfide thin films without NiO films.

Table III.1: Thin film deposition conditions.

Substrate temperature (°k)	Concentration Ni (mol/l)	Concentration S (mol/l)	Distance (cm) (substrate- nozzle)	Flow of the solution (ml/min)
523	0.01	0.02	3.5	4
573	0.01	0.02	3.5	4
623	0.01	0.02	3.5	4

III.2.2. Characterization techniques

The thin layers NiS Prepared at different substrate temperatures 523°K, 573°K and 623°K were characterized by a Bruker-axis diffractometer type D8 Advance using the Brentano Bragg geometry (2θ) of wavelength λ_{ka}(Cu) = 1.5404 Å, with an accelerating voltage of 30 KV and a current of 40 mA for the structural properties (crystallite size, stress), for the optical characteristics of the films such as band gap, refractive index, extinction coefficient, The absorption coefficient and real and imaginary parts of the dielectric constant were calculated using an optical method from the transmittance and reflectance spectra of a Shimadzu 3101PC double-beam UV-VIS-NIR spectrometer, The investigation of nickel sulfide bond formation was obtained by Fourier transform infrared spectroscopy (Shimadzu IR-Infinity1), FT-IR measurements of nickel sulfide for all prepared samples were scanned in the range (400 - 4000 cm^{-1}), The surface morphologies of the nickel sulfide films were observed using a scanning electron microscopy (SEM) coupled with microanalysis (EDX) was used to determine the chemical composition of the samples, the electrical characterization was carried out with the aid of a four-point measuring device.

III.3. Results and discussion

III.3.1. Surface Morphology and Structural Investigation

III.3.1.1. SEM study

Surface morphology of nickel sulfide thin films was observed using SEM under 44300 magnification. Figure III.1 (a, b and c) is shown that all the films are found well covered on the glass substrate. SEM reveals that sprayed particles (cluster of atoms) are adsorbed onto the glass substrate. The porosity and the particle size of the NiS thin films were found as an overgrown cluster of the interconnected nano-flakes characterized via SEM analysis. The SEM image in Figure III.1 shows a highly porous surface comprised of interconnected nano-flakes with sizes less than 100 nm together. It appears to us that the film surface was evenly covered without cracks and holes. Figure III.1c shows an SEM image of deposited NiS thin film at 623 K exhibiting a nanosheet-like structure without cracks. This observation may facilitate the transmission of electrons and keep them with quite easily. SEM photograph reveals that sprayed particles (cluster of atoms) are adsorbed onto the glass substrate.

(a)
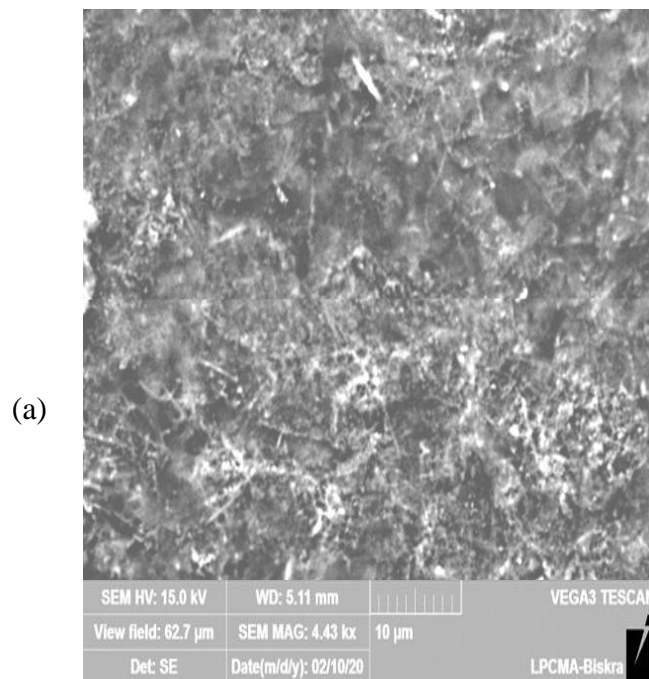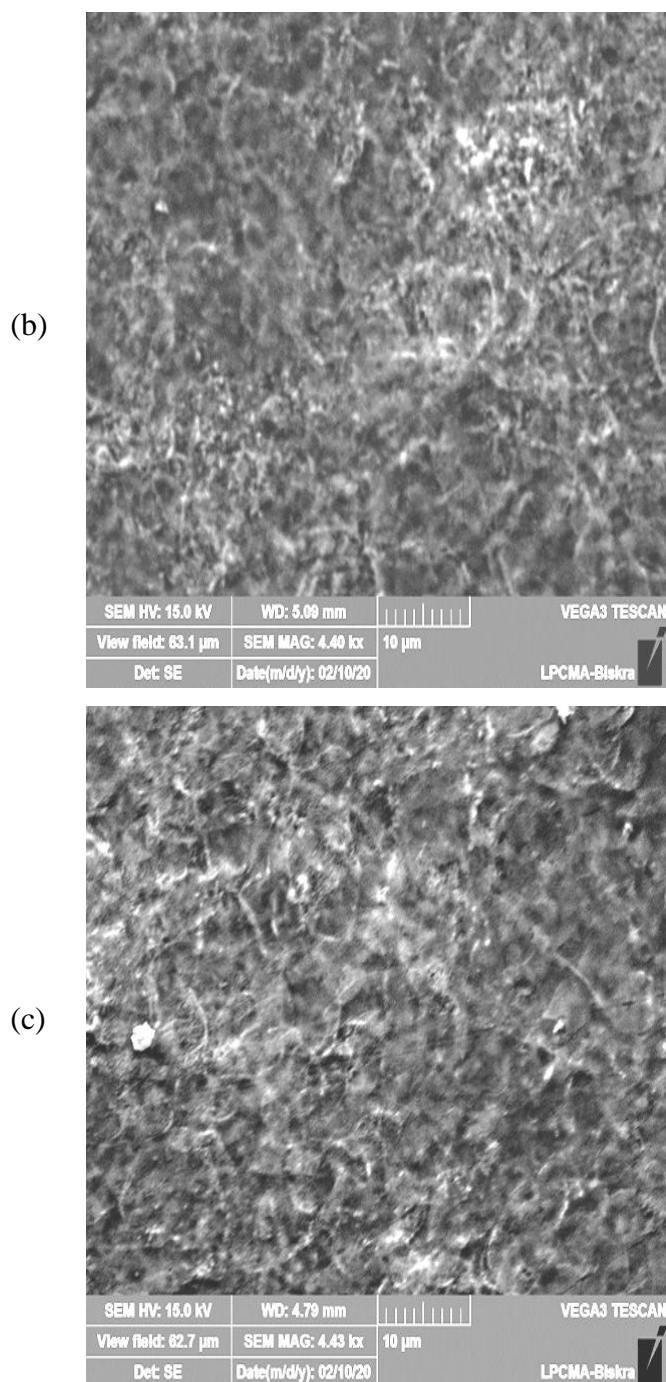
Figure III.1: SEM Image of nickel sulfide prepared at different substrate temperatures a) 523K, b) 573 K and c) 623K

III.3.1.2 EDX studies

The quantitative analysis of the as-deposited nickel sulfide films carried out by EDX is shown in Figure III.2 (a,b and c). Two strong peaks corresponding to Ni and S were found in the spectrum, which confirms the high purity of the Ni_xS_y thin film.
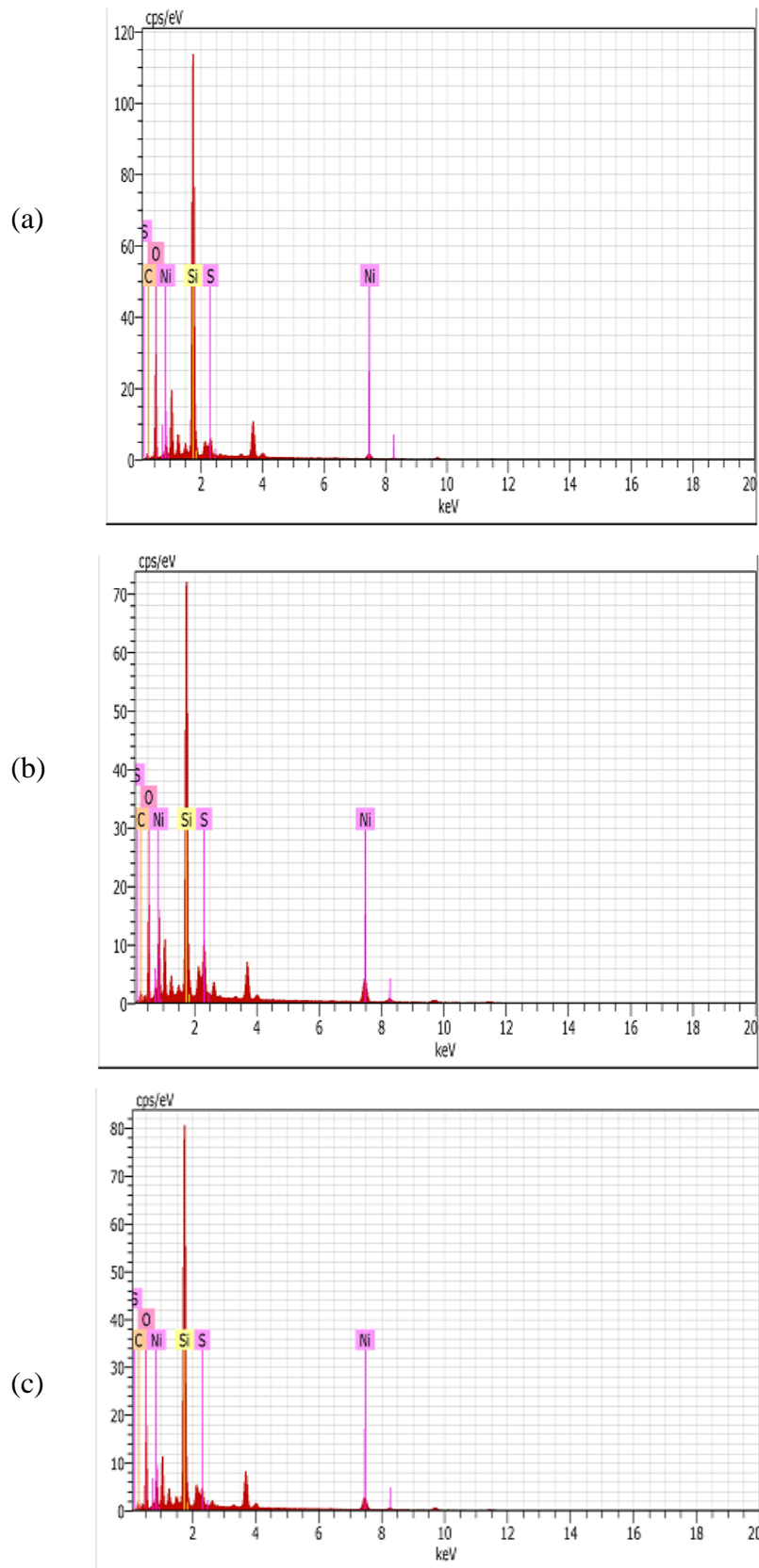
Figure. III.2: EDX spectrum of nickel sulfide thin films prepared at different substrate temperatures a) 523K, b) 573 K and c) 623K

As see, the atomic percentage of Ni and S is 1.57 and 2.31%, respectively, for a deposited film at 523 K. The atomic percentage of Ni and S increased from 1.57 to 5.54% and 2.31 to 5.00%, respectively, with increasing deposition temperature from 523 to 573 K. Moreover, the percentage of Ni and S decreased when the substrate temperature increased to 623K, which is 3.9 and 2.19%, respectively. The decrease of Ni and S at 623K can be explained by the evaporation of S with deposition temperature, this is attributed to the corporation between Ni and S. However, the results EDX suggested that the nickel sulfide was successfully deposited on glass substrates. The other elements present in the spectrum such as oxygen (O) and silicon (Si) come from glass substrate (SiO_2) and precursors used in the deposition bath. From Figure III.2, we cannot observe the NiO phase; this observation indicates that we cannot found a corporation between Ni and O.

III.3.2. X-ray diffraction analysis

To determine the structure of nickel sulfide thin films, samples were deposited on glass substrate by spray pyrolis method at different substrate temperature. The XRD patterns of the films were taken with a diffractometer, using CuK_α radiation (of wavelength, $\lambda = 1.5418$ Å) source. XRD scan was taken in between 20° to 60° of 2θ scale. The XRD patterns of nickel sulfide thin films are shown in Fig. III.3. The XRD diffraction patterns of nickel sulfide thin films deposited at different substrate temperatures by spray pyrolysis technique. The XRD diffraction shows that the prepared nickel sulfide at 523, 573 and 623 K having different phases and structures, which were Ni_3S_2 [9], $Ni_{17}S_{18}$ [10] and NiS_2 [11], respectively (see Table.III.1). As it can be seen the only diffraction peak was observed are (110), (015) and (010) plane at $2\theta = 29,471$ °, 29,351° and 29,309° of the sprayed nickel sulfide thin films at 523, 573 and 623 K, respectively (see Table.III.2). However, all thin films have high then one peak, which confirm that the preferred orientation was confined between these peaks; this observation indicates the polycrystalline in nature. The NiS_2 thin film prepared at 623 K has the two diffraction peaks intensities; this is attributed to the improvement of the crystalline structure of NiS_2 thin films. On the other hand, we cannot observe other diffraction peaks related to the NiO phase.
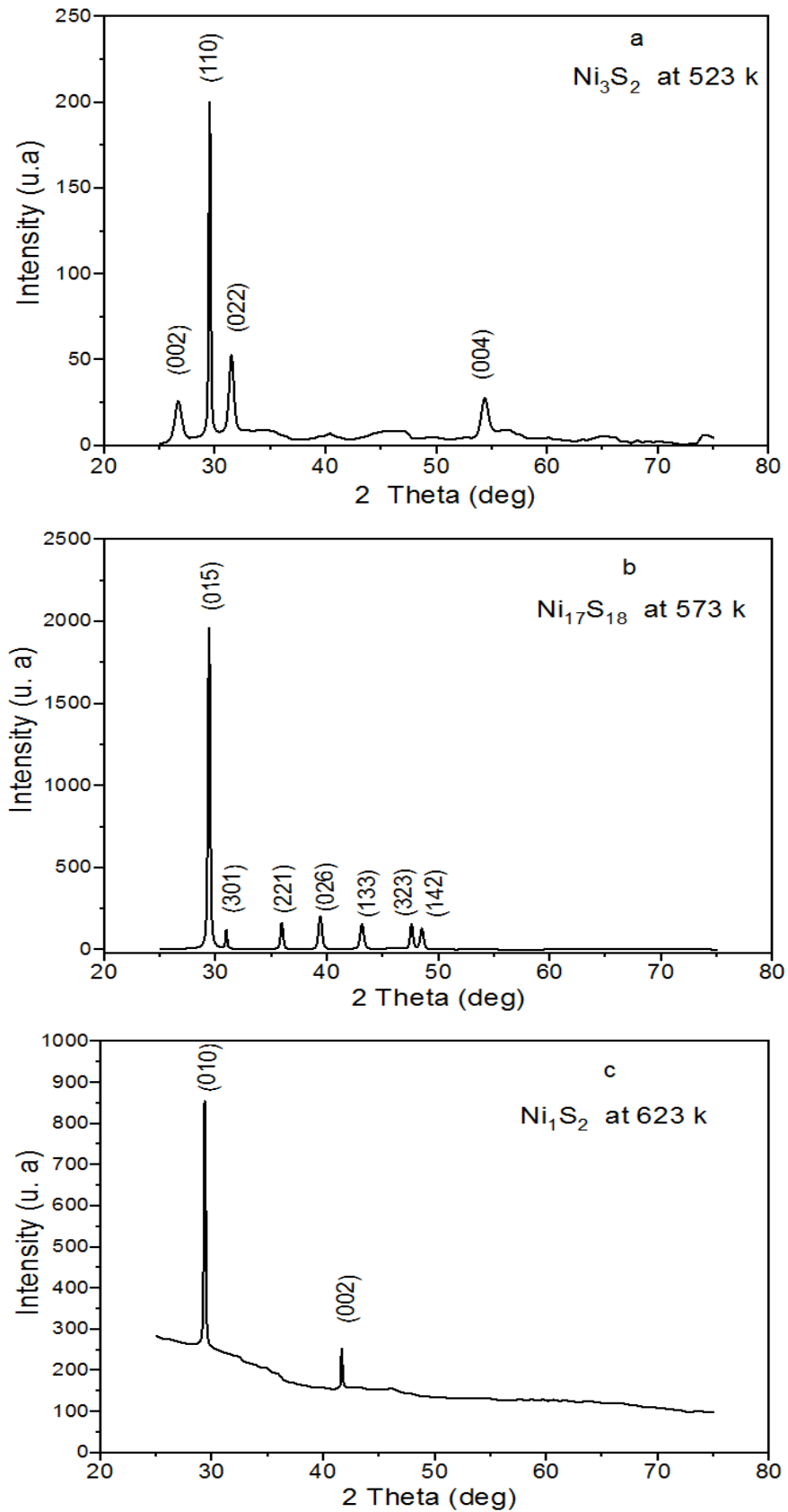
Figure III.3: XRD patterns of nickel sulphide thin films deposited on glass substrate at different substrate temperature: (a) 523 k, (b) 573 k and (c) 623 k.

Table III.2: The phase structure of nickel sulphide thin films at different substrate temperatures.

Substrate temperature (°k)	Name	Chemical formula	Crystal system	Space group	Reference
523	Nickel sulfide 3/2	Ni_3S_2	orthorhombic	Cm Cm 63	98-018-0767
573	Nickel sulfide 17/18	$Ni_{17}S_{18}$	hexagonal	P31 21 152	98-003-7164
623	Nickel sulfide 1/2	Ni_1S_2	hexagonal	P63/m mc 194	98-016-9577

The main strain of the highest peak was calculated by the following relation [12]:

$$\varepsilon = \frac{\beta}{4\tan\theta} \quad \text{………………….(III.1)}$$

where ε is the micro-strain, β is the FWHM and θ is the half diffraction angle. On the other hand, the crystallite size values were estimated using Scherer equation [13]:

$$G = \frac{0.9\lambda}{\beta\cos\theta} \quad \text{…………………....(III.2)}$$

where G is the crystallite size, λ is the wavelength of X-ray (λ = 1.5406 A°). However, the dislocation density δ of nickel sulfide thin films was calculated from crystallite size by following relation [14]:

$$\delta = \frac{1}{G} \quad \text{……………………….(III.3)}$$

Table III.3: Values of Bragg angle 2θ , interplanar spacing d_{hkl}, full width at half maximum $\beta_{1/2}\left(rd\right)$, grain size $G.S$, micro strain ε and dislocation density δ for nickel sulfide thin films deposited on glass substrate at different substrate temperature: 523 °k, 573 °k and 623 °k.

Substrate temp (°K)	2θ (deg.)	hkl	$\beta_{1/2}$ (rad)	G (nm)	ε x10^{-3} (%)	δ x10^{14} (cm^{-1})
Ni_3S_2 at T=523	29.471	110	0,00288	49.785	2.936	4.0383
$Ni_{17}S_{18}$ at T=573	29.351	015	0,00312	45.878	3.197	4.749
Ni_1S_2 at T=623	29.309	010	0,00169	84.567	1.732	1.400

Table.III.2 shows the variation as a substrate temperature of the main strain, crystallite size and dislocation density of nickel sulfide thin films. As see, the lowest crystallite size was found for a deposited film at T=573 K corresponded to $Ni_{17}S_{18}$. As can be seen that the film deposited at 623 K (Ni_1S_2) has a minimum strain due to the equivalent in the number of atoms, also this film has a minimum dislocation density.

III.3.3. Optical Properties

To determine the transmittance and reflectance of thin films, we used a double-beam UV-Visible spectrophotometer of the Shamadzu type (see chapter I).

III.3.3.1. Transmittance and Reflectance

The optical, transmittance and reflectance versus wavelength curves of nickel sulfide deposited onto glass substrates at different substrate temperature were taken in the wavelength range over 300 nm to 1100 nm. The transmittance and reflectance of thin films are shown in Figure III.4 and Figure III.5, respectively.
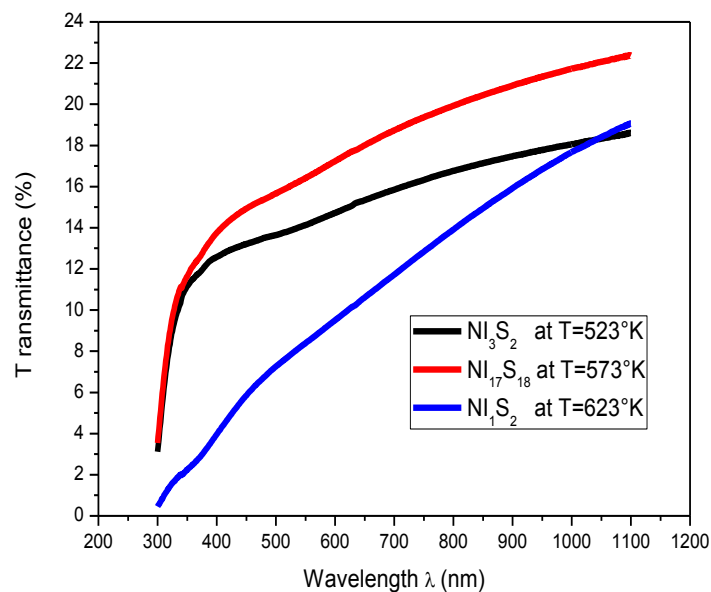
Figure III.4: Transmittance vs. wavelength graph of nickel sulfide thin films deposited at different substrate temperature.

Figure III.4 shows the optical transmittance (T in %) of NiS thin films synthesized at Ts of 523, 573 and 623 °K. The highest value of T, 22.37%, is found for Ts = 350 °C at

1100 nm. A relatively higher T value for the NiS thin film deposited at Ts of 350 °C may be attributed to less scattering due to the decrease of the degree of irregularity in the particle size distribution. In the visible region, T of NiS thin films increases sharply with the increase of wavelength. Boughalmi et al. reported that the highest value of T was about 40% for the NiS thin films grown at Ts = 250 °C [10].
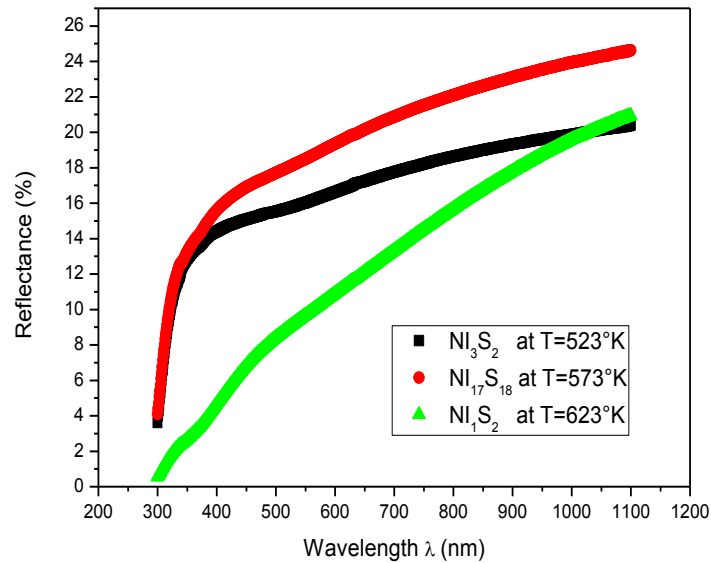
Figure III.5: Transmittance vs. wavelength graph of nickel sulfide thin films deposited at different substrate temperature.

Figure III.5 shows the optical reflectance (R) curves for the thin films of nickel sulfide deposited at different temperatures of the substrate 523°K, 573°K and 623°K. The reflectance of the nickel sulfide thin film increases with the wavelength and reaches 25%.

We also notice on the transmittance and reflectance spectra that the reflectance value is always higher than the transmittance value; this phenomenon can be linked to a metallic behavior, which reflects the absorbent character of the nickel sulfide film [12].

III.3.2.2. Absorption coefficient

The spectrum of the optical absorption coefficient α as a function of photon energy hν is shown in Figure III. 6 for nickel sulfide prepared at different substrate temperatures, the data from the transmittance (T) and reflectance (R) spectra are used to calculate the absorption coefficient using equation (III.4) [15]:

$$\alpha = \frac{1}{d} Ln\left(\frac{(1-R)^2}{T}\right) \quad \ldots\ldots\ldots\ldots\ldots\ldots\ldots\ldots(III.4)$$

where d is the film thickness, α is the absorption coefficient, T is the transmittance, R is the reflectance.

The variation of α with photon energy (hν) for nickel sulfide thin films deposited at different substrate temperature is shown in Figure III.6. This figure shows the distinction of α with photon energy for substrate temperatures. The α is of the order of 10^4 cm^{-1} which may also be suitable for a transparent conducting film. From the figure it is observed that α first increases slowly in the low energy region i.e. in the high wavelength region and then increases sharply near the absorption edge. The value of α depends on substrate temperatures.
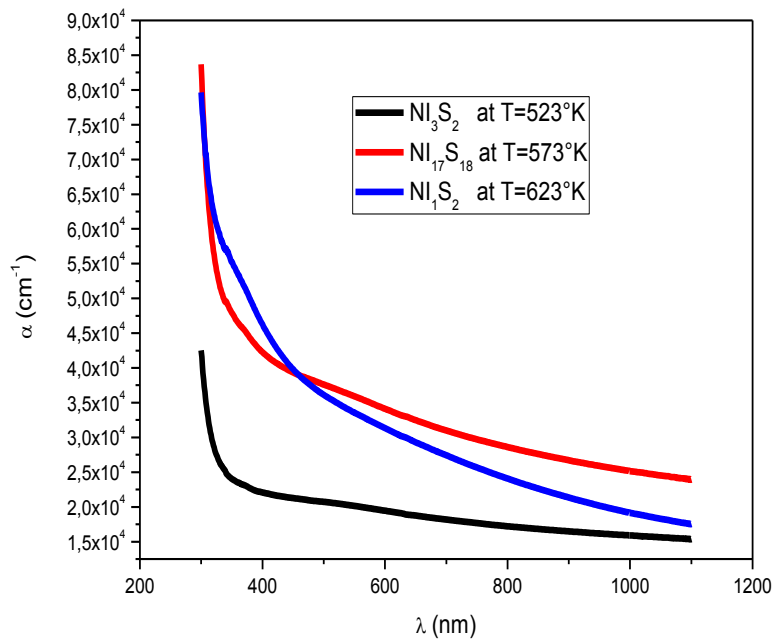
Figure III.6: Variation of the absorption coefficient α with wavelength for nickel sulfide thin films deposited at different substrate temperature.

III.3.3.3. Gap energy

The energy gap in a semiconductor is responsible for the fundamental optical absorption edge. The fundamental absorption process is one in which a photon is absorbed

and an electron is excited from an occupied valance band state to an unoccupied conduction band state. If photon energy is less than the gap energy, such process is impossible and photon energy will not be absorbed. Such inter band absorption process are possible only if the photon energy is higher than the gap energy. Since α is used to describe the reduction in intensity of light in a medium as a function of distance, therefore higher values of α is an indication of more reduction in intensity. Figure III.7 shows the plots of $(\alpha h\mathbf{v})^2$ vs. photon energy ($h\mathbf{v}$) for direct transition. The optical band gap (Eg) is determined from the plots of $(\alpha h\mathbf{v})^2$ vs. photon energy ($h\mathbf{v}$) for direct transition for NiS thin films. The direct band gap energy of the films have been obtained from the intercept on the energy axis after extrapolation of the straight line section of $(\alpha h\mathbf{v})^2$ vs. $h\mathbf{v}$ curve. The energy of the band gap decreases from 3.7 to 2.36 eV when the deposition temperature is increased from 523 to 623°K, and these values are close to those in the literature [11]. This reduction is probably due to the increase in grain size, as it has been shown that the increase in crystallite size reduces the optical gap [16]. The nature of this variation in the band gap energy may be useful to design a suitable window material in fabrication in super capacitor.

Figure III.7: Variation of the curve $(\alpha h v)^2 = f(h v)$ as a function for nickel sulfide thin films deposited at different substrate temperature.

III.3.3.4. Optical and dielectric constants

III.3.3.4.1. Extinction coefficient k

The extinction coefficient (K) represents the amount of absorption energy in the thin film material, which means the attenuation of an electromagnetic wave propagating in a material. The values of (K) depend on the density of free electrons in the material as well as on structural defects. The extinction coefficient was calculated using the relation (III.5) [17].

$$K = \frac{\alpha \times \lambda}{4\pi} \dots\dots\dots\dots\dots\dots(III.5)$$

where R is expressed as reflectance, α is the absorption coefficient and λ is wavelength.

The variation of extinction coefficient with wavelength is shown in Figure III.8. It is observed that the extinction coefficient increases with the increase of substrate temperature. The change in the extinction coefficient is directly related to the absorption of light. The fall in the extinction coefficient may be due to the absorption of light at the grain boundaries. From figure it is clear that k decreases rapidly with increasing wavelength from 400 to 500 nm.
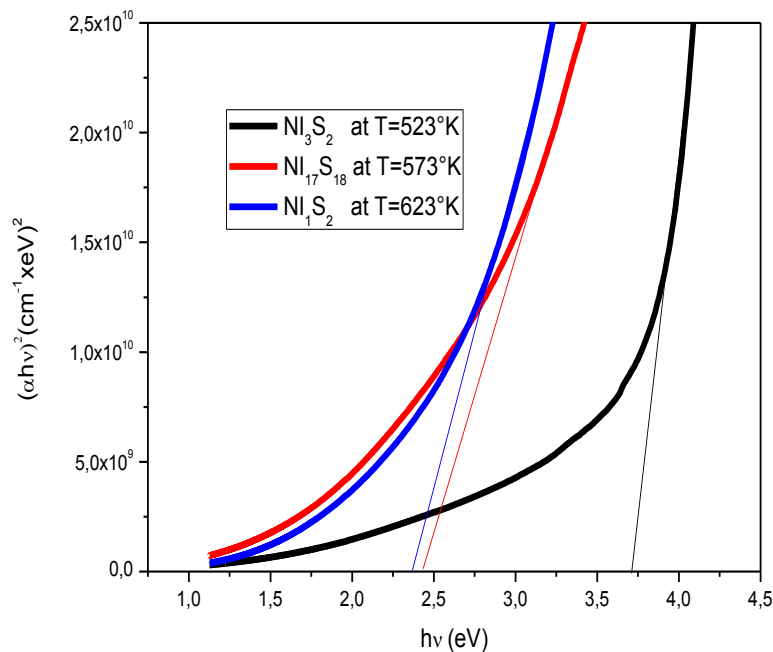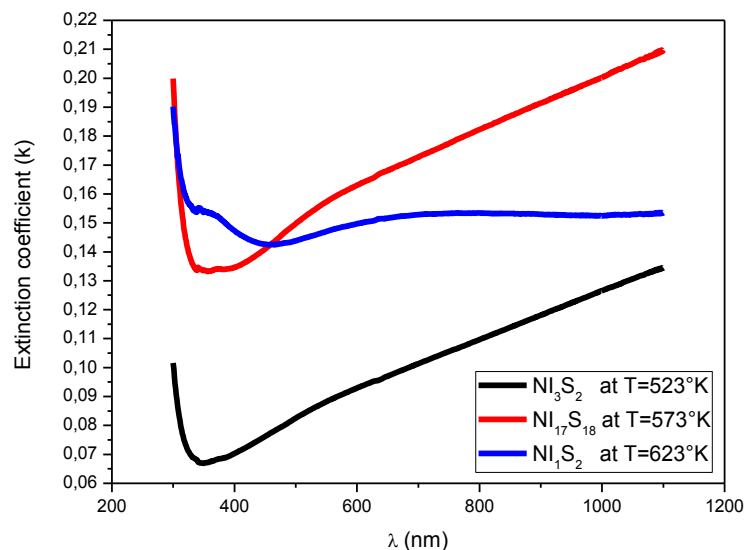

Figure III.8: Variation of extinction coefficient with wavelength for nickel sulfide thin films deposited at different substrate temperature.

III.3.3.4.2. Refractive index n

The refractive index is the ratio between the speed of light in a vacuum and the speed of light in a material. The values of the refractive index (n) were calculated using equation (III.8) as a function of the reflectance (R) and absorption coefficient (k) values [18].

$$n = \frac{1+R}{1-R} + \sqrt{\frac{4R}{(1-R)^2} - k^2} \quad \ldots\ldots\ldots\ldots\ldots\ldots\ldots\ldots(III.6)$$

where, n is the refractive index, k is the extinction and R is the optical reflectance.

The variation of refractive index with wavelength for various temperature of deposition is shown in Figure III.9. From this Figure, it is observed that the refractive index increases rapidly in between 300 to 400 nm wavelength region and then increases slowly with increasing wavelength from 400 to 1100 nm.
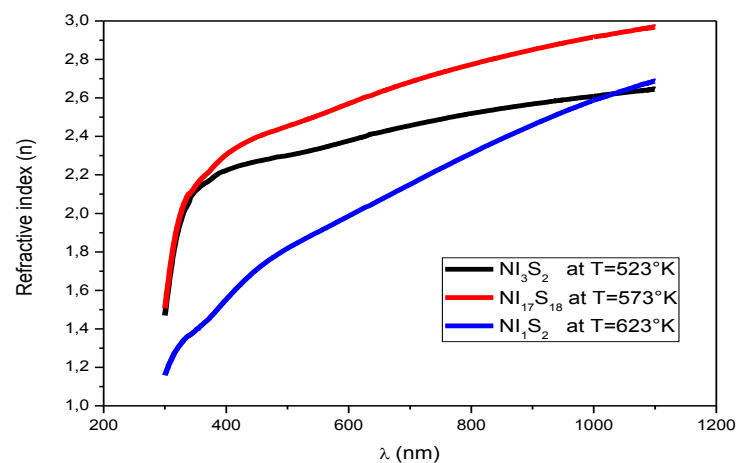
Figure III.9: Variation of refractive index as a function of wavelength of nickel sulfide films deposited at different substrate temperatures.

III.3.3.4.3. Dielectric constant

The variation of the complex electronic dielectric constant has been used to describe the fundamental electronic excitation spectrum of films. The complex dielectric function can be described as equation (III.7) [19].

$$\varepsilon = (n^2 - k^2) + (2n \times k)i \ldots\ldots\ldots\ldots\ldots\ldots(III.7)$$

where: the first term of equation (III.7) is the real part of the dielectric constant (ε_1).

$$\varepsilon_r = n^2 - k^2 ....(III.8)$$

And the second term in equation (III.7) is the imaginary part of the dielectric constant (ε_r).

$$\varepsilon_i = 2n \times k ....(III.9)$$

Real and imaginary parts of dielectric constants (ε_r and ε_i) are calculated using the equation (III.8) and (III.9), respectivily. The variation of the real (ε_r) and imaginary (ε_i) parts of the dielectric constant for different film concentrations are illustrated in Figure III.10 and Figure III.11. The complex dielectric constant is fundamental intrinsic material property. The real part of it is associated with the term that how much it will slow down the speed of light in the material and imaginary part gives that how a dielectric absorb energy from electric field due to dipole motion. The real part ε_r is the normal dielectric constant and imaginary part ε_i represents the absorption associated of radiation by free energy. It is seen that both (ε_r) and (ε_r) increases with increasing wavelength. The figures imply that the values of the real part are higher than that of the imaginary part and follow the almost same pattern.
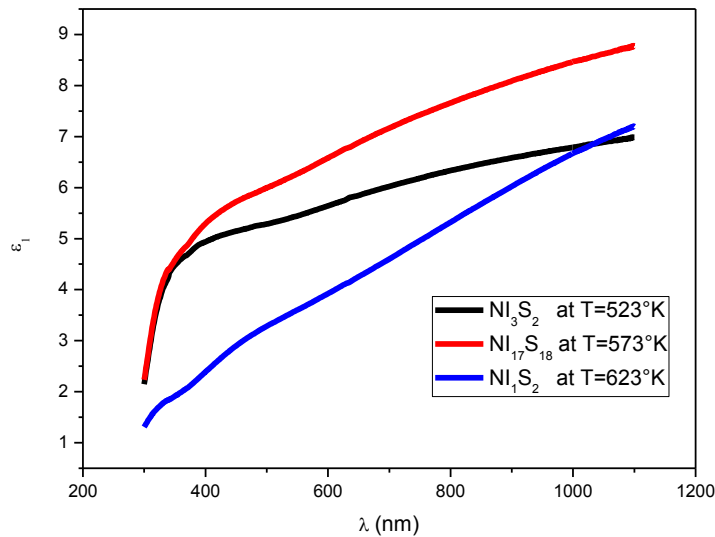
Figure III.10: Variation of real part of dielectric constant ε_r as a function of wavelength of nickel sulfide thin films.
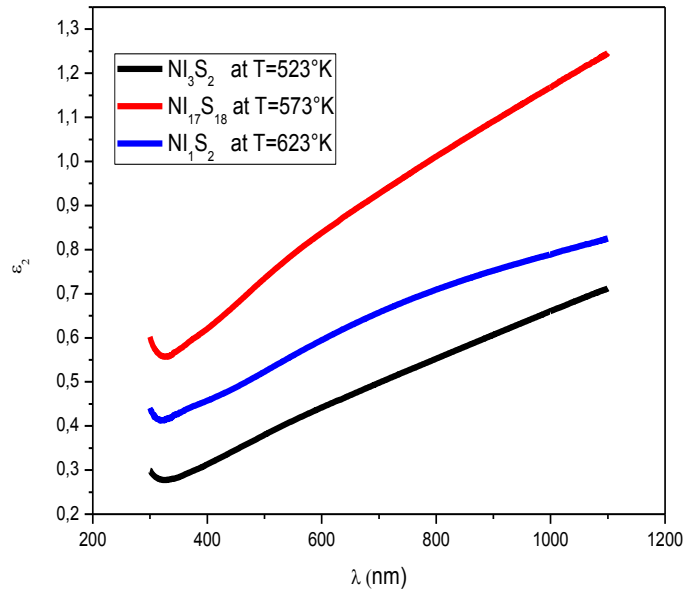
Figure III.11: Variation of imaginary part of dielectric constant ε_i as a function of wavelength of nickel sulfide thin films.

III.3.3.5. Urbach tailing energy calculation

For hν less but so near the band gap energy, the values of the absorption coefficient α are different to zero. Its behavior in terms of the energy of incident photon can be determined using [20]:

$$\alpha = \alpha_0 \exp\left(\frac{hv}{E_u}\right) ....(III.10)$$

where E_u is the Urbach energy. This energy confines the shape of the fundamental absorption edge in the exponential (Urbach) region and gives information on the structural disorder in the material. According to the urbach rule, the presence of defects and lack of crystalline long-range order results in tailing of density of states.

The width of the localized states (band tail energy or urbach energy E_u) has been estimated from the slope of the plot of $\ln(\alpha)$ vs hv. Energy hν near Eg at room temperature (Figure.III.12).
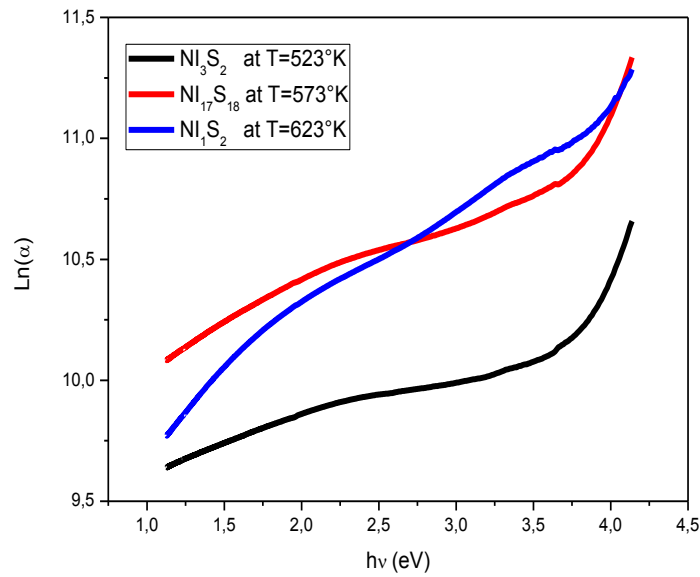
Figure III.12: $\ln(\alpha)$ vs $h\nu$ for nickel sulfide prepared at different substrate temperatures.

Figure III.12 show the variation of $Ln\alpha$ as a function $h\nu$ for estimated the Urbach energy (see Table.III.3). From Table.III.1, we have found that the minimum optical band gap and Urbach energy were obtained for sparing Ni_1S_2 at T=623 K. This is confirmed that the temperature of 623 K is suitable for preparing the Ni_1S_2 thin film with good optical gap energy and less disorder.

III.3.3.6. Optical conductivity

Optical conductivity is defined as the increase in the number of charge carriers (electrons or hole) resulting from the fall of a light beam on a semiconductor. Optical conductivity can be calculated using the relation (III.11) [21]:

$$\sigma_{opt} = \frac{\alpha\eta C}{4\pi} ....(III.11)$$

where c is the velocity of light, α is absorption coefficient and n is refractive index.

Figure.III.13 shows that the optical conductivities are increases with photon energy and it is also observe that conductivities are increases with the different substrate temperatures. This means that photons having lower energy are absorbed while photon having higher energy can transmit through the thin films. [22]. The optical conductivity

increases at high photon energies (3.5 eV to 4.25eV) is may be due to the high absorbance of thin films.
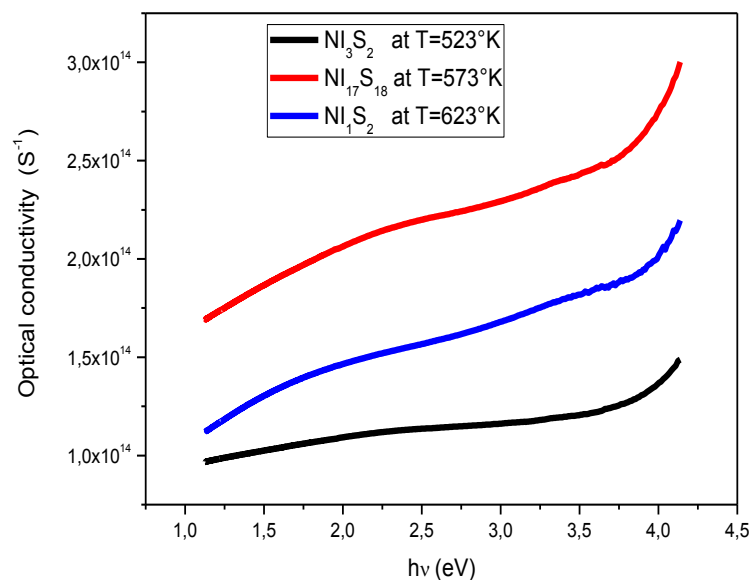
Figure.III.13: Variation of optical conductivity as a function of wavelength of nickel sulfide films deposited at different substrate temperatures.

Table III.4. Optical properties of nickel sulphide thin films at different substrate temperatures

Substrate temp (K)	E_g (eV)	E_u (meV)	σ_{opt} x10^{14} (S)
Ts=523	3.70	155.043	1.071
Ts=573	2.39	245.952	1.871
Ts=623	2.36	36.114	1.301

III.3.4. Fourier Transform Infra-Red Spectroscopy (FTIR)

Fourier transforms infrared spectra (FTIR) is a technique which is used to obtain information about the chemical bonding in a material by producing an infrared absorption spectrum. It can be used to determine the nature and the structure of compounds. In this work it is used to identify the chemical reactions leading to the formation of the NiS thin film. FTIR spectra, in 500 – 4000 cm^{-1} range, of residual products and solutions by using KBr as support were released.

To further support the XRD results, the quality and composition of nickel sulphide thin films were investigated by FTIR spectroscopy. FT-IR is known as one of the very useful method to find out information about chemical bonding and identification of material elemental constituents. FT-IR spectra in of the nickel sulphide thin films prepared at different substrate temperatures a) 523°K, 573°K and 623°K by the pyrolysis spray technique are shown in Figure.III.14.
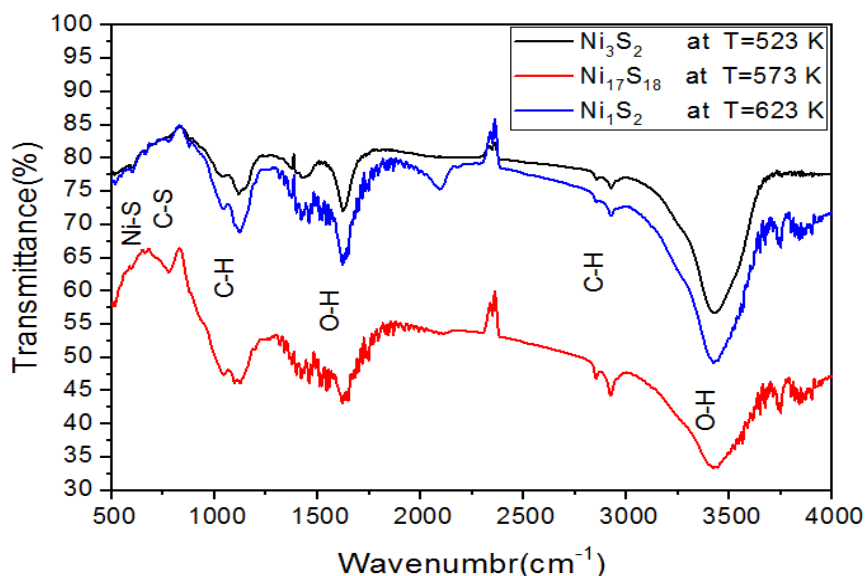
Figure III.14: FTIR spectrum of nickel sulfide prepared at different substrate temperatures 523 K, 573 K and 623 K.

The FTIR spectrum of the nickel sulfide is shown in Figure III.14, the peak at 601.79 cm^{-1} was attributed to the stretching vibration of Ni-S in the nickel sulfide phases [23]. The band at about 667.36 cm^{-1} and 875.68 cm^{-1} and 1037.7 cm^{-1} is attributed to the asymmetric stretching vibration of the C-S bond from the precursors [23]. The 1114.86 cm^{-1} band denotes the bending vibration of the sulfide functional group [24]. The bands observed at 2854.65 cm^{-1} and 2924.09 cm^{-1} were attributed to the C-H extension vibration of the precursor [25]. The broad peak at 3400 cm^{-1} corresponds to the N–H stretching of free amines. The presence of peaks around 1645 cm^{-1} corresponds to O-H stretching and bending vibrations [23- 25]. Whereas band at around 601 cm^{-1} is resulting from the nickel sulfide lattice vibration [24]. It worth noting that absorption band at 601cm^{-1} appears in all spectra; this bond is evaluated using Hook's law giving by the following formula (III.12) [23]:

$$\bar{v} = \frac{1}{2\pi c} \sqrt{\frac{k}{\mu}} \qquad (III.12)$$

where c is the light velocity, k is the bond force constant and μ is the reduced mass of nickel and sulfide. Thus the position of specific band absorption of nickel sulfide powders is determined with the basis of the 5.10^5 dynes/cm and the reduced mass $\mu = 1/m_{Ni} + 1/m_S$ which leads to an absorption bond at 601 cm^{-1} closely to the observed one in all spectra of Figure.III.14.

III.3.5. Electrical properties

The electrical measurements of these films were made using the four-point technique (see Chapter I). The electrical conductivity of NiS films is important for their application in supercapacitors.

In table III.5, we have reported the values of square resistance (Rsh), resistivity (ρ) and conductivity (σ) measured using the four-point technique under the following conditions.

✓ Plate shape: square, Insert size: 76.1 mm, Edge exclusion: 20 mm, Number of points: 4 points, Current used: 2.5312 mA

The electrical conductivity of NiS thin films is based on the measured resistance of the film layer as expressed [26].

$$\sigma = \frac{1}{d \times R_{sh}} \qquad (III.13)$$

Table III.5: The film thickness and electrical properties of nickel sulphide thin films at different substrate temperatures.

Substrate temp (°K)	d(nm)	$R_{sh}(\Omega)$	Resistivity(Ω.cm)	Conductivity(Ω.cm)$^{-1}$
Ts=523°K	797,903	0,201	1,60E-05	6,24E+04
Ts=573°K	389,246	0,0599	2,33E-06	4,29E+05
Ts=623°K	681,424	155	1,06E-02	9,47E+01

Table III.5 presented the variation of the film thickness, electrical resistance, resistivity and conductivity of nickel sulfide thin films at different substrate temperatures. As shows that the electrical conductivity increased directly to sprayed thin film at 573 K then decreases with 623 K due to the high transmission and defects. The maximum electrical conductivity is $4{,}29 \times 10^5$ $(\Omega.cm)^{-1}$, the reason to have a high electrical conductivity can be shown in the speed of the displacement of the electrons in the surface of a thin film with deposition temperature to the diffusion of S^{2-} donors and the substitutional sites of Ni^{2+}.

III.4. Summary of results of the prepared thin films and the reported NiS thin films

Table III.6: The comparative study of the structural, optical and electrical properties of nickel sulfide thin films at different conditions

Ts (K)	Phase	Deposition method	Film thickness (nm)	Crystallite size G (nm)	Optical energy E_g (eV)	Activation energy E_a (eV)	Electrical conductivity σ ($\Omega.cm$)	Rf.
473	NiS	SESP		53	0.56		10^4	[1]
498-673	Ni_3S_2	PVD	-	90.8	2.1	-	-	[10]
	6%Cu doped Ni_3S_2		-	90.8	1.89	-	-	
	10%Cu doped Ni_3S_2		-	90.8	1.63	-	-	
300	NiS	SILAR	20-100	-	0.45	0.15	10	[21]
-	NiS	Spray	-	13-22	0.55	-	-	[27]
523	Ni_3S_2	Spray pyrolysis	798	49.8	3.70		$6.24.10^4$	This work
573	$Ni_{17}S_{18}$		390	45.9	2.39		$4.29.10^5$	
673	Ni_1S_2		681	84.5	2.36		$9.47.10^1$	

III.5. Conclusion

In the chapter, nickel sulfide (Ni_xS_y) thin films were prepared by spray pyrolysis method. Films were deposited on glass the substrates at different substrate temperature. Different physical properties such as structural, optical and electrical properties as well as surface morphology have been studied. In this work, it is observed that the deposition of Ni_xS_y films depends on various parameters such as substrate temperature, concentration of the solution used, spray rate and deposition time.

The SEM micrograph shows that films are uniform and smooth, compact, continuous and uniform. There are some spheroid shape appears as the creation of nucleation centre on the film surfaces. Energy dispersive X-ray (EDX) is used for the elemental analysis of the films. By studying the EDX data we also get the information about the elements in the Ni_xS_y thin films.

X-ray diffraction (XRD) study was taken to identify the structure of the deposited films. Lattice constant and grain size are calculated from XRD. The grain size is found in the range of 22.23- 28.93 nm. Lattice constant calculated for hexagonal lattice are a = 3.3570 to 3.8952 Å and c = 6.7062 to 6.7405 Å. These values are quite close to the reported value.

Optical measurements were made on Ni_xS_y films. It is observed that absorbance in the ultraviolet region is high. Absorption coefficient has been calculated from transmission spectra taken within the wavelength of 300 to 1100 nm. The absorption coefficient obtained is of the order of $10^4 cm^{-1}$ in the higher energy region and the rate of absorption is maximum near the absorption edge, which is around 500 nm. The band gap was evaluated from the transmission data. The obtained direct band gap of Ni_xS_y is varied from 3.25eV to 2.48 eV.

FTIR spectrums of the nickel sulfide have various bands such as Ni-S, C-H, O-H, N–H and C-S. The maximum electrical conductivity is $4,29x10^5$ $(\Omega.cm)^{-1}$ was obtained at 573 K of the $Ni_{17}S_{18}$. The nickel sulfide thin films sprayed at 573 K have good structural, optical and electrical properties, this thin film can be used a promising co-catalyst to improve the photocatalytic performance or superconductivity.

References

[1] O. O. Balayeva, A. A. Azizov, M. B. Muradov, A. M. Maharramov, G. M. Eyvazova, R. M. Alosmanov, Z. Q. Mamiyev, and Z. A. Aghamaliyev, "β-NiS and Ni3S4 nanostructures: Fabrication and characterization," Materials Research Bulletin, vol. 75, pp. 155-161, 2016.

[2] N. M. Shinde, Q. X. Xia, P. V. Shinde, J. M. Yun, R. S. Mane, and K. H. Kim, "Sulphur Source-Inspired Self-Grown 3D Ni x S y Nanostructures and Their Electrochemical Supercapacitors," ACS applied materials & interfaces, vol. 11, pp. 4551-4559, 2019.

[3] H. Lee, M. Kanai, T. Kawai, and S. Kawai, "Growth of oriented NiS films on Si (111) and Al2O3 (012) substrate by pulsed laser ablation," Japanese journal of applied physics, vol. 32, p. 2100, 1993.

[4] S. Sartale and C. Lokhande, "Preparation and characterization of nickel sulphide thin films using successive ionic layer adsorption and reaction (SILAR) method," Materials Chemistry and Physics, vol. 72, pp. 101-104, 2001.

[5] S. H. Yu and M. Yoshimura, "Fabrication of Powders and Thin Films of Various Nickel Sulfides by Soft Solution-Processing Routes," Advanced Functional Materials, vol. 12, pp. 277-285, 2002.

[6] L. Zhang, J. C. Yu, M. Mo, L. Wu, Q. Li, and K. W. Kwong, "A general solution-phase approach to oriented nanostructured films of metal chalcogenides on metal foils: The case of nickel sulfide," Journal of the American Chemical Society, vol. 126, pp. 8116-8117, 2004.

[7] M. Akhtar, N. Revaprasadu, M. A. Malik, and J. Raftery, "Deposition of phase pure nickel sulfide thin films from bis (O-alkylxanthato)–nickel (II) complexes by the aerosol assisted chemical vapour deposition (AACVD) method," Materials Science in Semiconductor Processing, vol. 30, pp. 368-375, 2015.

[8] A. Mahadik, S. Khalate, R. Kate, and R. Deokate, "Chemical Spray Deposited Nickel Sulphide Thin Films for Supercapacitor applications, I," Res. J. Sci. Eng. Special, pp. 195-198, 2017.

[9] Z. Cheng, H. Abernathy, and M. Liu, "Raman spectroscopy of nickel sulfide Ni3S2," The Journal of Physical Chemistry C, vol. 111, pp. 17997-18000, 2007.

[10] S. Saeed and N. Rashid, "Growth and characterization of semiconducting nickel sulfide nanocrystals from air-stable single-source metal organic precursors," Cogent Chemistry, vol. 1, p. 1030195, 2015.

[11] F. Chen, H. Yang, X. Wang, and H. Yu, "Facile synthesis and enhanced photocatalytic H2-evolution performance of NiS2-modified g-C3N4 photocatalysts," Chinese Journal of Catalysis, vol. 38, pp. 296-304, 2017.

[12] S. Benramache, Y. Aoun, S. Lakel, B. Benhaoua, and C. Torchi, "The calculate of optical gap energy and urbach energy of Ni 1− x Co x O thin films," Sādhanā, vol. 44, p. 26, 2019.

[13] H. P. Klug and L. E. Alexander, X-ray diffraction procedures: for polycrystalline and amorphous materials, 1974.

[14] T. A. Ho, C. Bae, H. Nam, E. Kim, S. Y. Lee, J. H. Park, and H. Shin, "Metallic Ni3S2 films grown by atomic layer deposition as an efficient and stable electrocatalyst for overall water splitting," ACS applied materials & interfaces, vol. 10, pp. 12807-12815, 2018.

[15] J. Dias da Silva, R. Campomanes, D. Leite, F. Orapunt, and S. K. O'Leary, "Relationship between the optical gap and the optical-absorption tail breadth in amorphous GaAs," Journal of applied physics, vol. 96, pp. 7052-7059, 2004.

[16] J. Tauc and A. Menth, "States in the gap," Journal of non-crystalline solids, vol. 8, pp. 569-585, 1972.

[17] F. Urbach, "The long-wavelength edge of photographic sensitivity and of the electronic absorption of solids," Physical Review, vol. 92, p. 1324, 1953.

[18] S. Benramache and M. Aouassa, "Preparation and characterization of p-type semiconducting NiO thin Films Deposited by Sol-Gel Technique," Journal of Chemistry and Materials Research, vol. 5, pp. 119-122, 2016.

[19] V. Schmachtenberg, G. Tontini, J. Koch, G. Semione, and V. Drago, "Low temperature solventless syntheses of nanocrystalline nickel sulfides with different sulfur sources," Journal of Physics and Chemistry of Solids, vol. 87, pp. 253-258, 2015.

[20] A. J. Reddy, M. Kokila, H. Nagabhushana, S. Sharma, J. Rao, C. Shivakumara, B. Nagabhushana, and R. Chakradhar, "Structural, EPR, photo and thermoluminescence

properties of ZnO: Fe nanoparticles," Materials Chemistry and Physics, vol. 133, pp. 876-883, 2012.

[21] R. Boughalmi, A. Boukhachem, M. Kahlaoui, H. Maghraoui, and M. Amlouk, "Physical investigations on Sb2S3 sprayed thin film for optoelectronic applications," Materials Science in Semiconductor Processing, vol. 26, pp. 593-602, 2014.

[22] M. Caglar, S. Ilican, and Y. Caglar, "Influence of dopant concentration on the optical properties of ZnO: in films by sol–gel method," Thin Solid Films, vol. 517, pp. 5023-5028, 2009.

[23] L. Zhang, D. Shi, T. Liu, M. Jaroniec, and J. Yu, "Nickel-based materials for supercapacitors," Materials Today, vol. 25, pp. 35-65, 2019.

[24] S. Slama, M. Bouhafs, and K. B. Mahmoud, "A boubaker polynomials solution to heat equation for monitoring A3 point evolution during resistance spot welding," International Journal of Heat and Technology, vol. 26, pp. 141-146, 2008.

[25] J. Pankove, "Optical processes in semiconductors Prentice-Hall," New Jersey, vol. 92, 1971.

[26] S. Majid and K. S. Ahmad, "Analysis of dopant concentration effect on optical and morphological properties of PVD coated Cu-doped Ni3S2 thin films," Optik, vol. 187, pp. 152-163, 2019.

[27] H.-C. Tao, X.-L. Yang, L.-L. Zhang, and S.-B. Ni, "One-step synthesis of nickel sulfide/N-doped graphene composite as anode materials for lithium ion batteries," Journal of Electroanalytical Chemistry, vol. 739, pp. 36-42, 2015.

CHAPTER IV:
EFFECT OF MOLAR CONCENTRATION ON THE PHYSICAL PROPERTIES OF NiS THIN FILMS

IV.1. Introduction

Nickel sulfide is one of the most attractive material due to its high electron mobility, a high reflection in the infrared range, an ease of production and low toxicity. As one of the main classes of transition metals, Chalcogénures, nickel sulfides exists in different phases, such as NiS, NiS_2, Ni_3S_2, Ni_7S_6 and Ni_9S_8. Among these phases, NiS exhibits an excellent capacity performance, high redox activity, which should satisfy the growing need of energy storage systems [1]. This material is an important and challenging material to scientists. In general, NiS exists in two phases, hexagonal and rhombohedral [2]; both phases exhibit many applications. Different methods such as: spray-pyrolysis [3], chemical bath deposition (CBD) [4], hydrothermal [5], Successive ionic layer adsorption and reaction (SILAR) [6], thermal evaporation [7], electro-deposition [8] and sol-gel [9], have been used to deposite NiS thin films. Given the importance of thin films in industrial production, an easy and inexpensive method should be sought among these methods. The spray-pyrolysis technique has proven to be effective, since it did not require an advanced technology and complex devices. The films deposited via this technique are characterized by their strong adhesion to the substrate, the ability to prepare a film with surfaces relatively large and the ability to obtain films with the required specifications, which is done by mixing a solution of two or more materials and changing the proportions involved in the composition of the film.

In this chapter, we describe the preparation procedure, experimental details and the technique used for the synthesis of NiS films. The effect of precursor concentration on physical properties of the samples will be discussed.

IV.2. Methodology

IV.2.1. Preparation of nickel sulfide NiS thin films

NiS films were deposited on well-cleaned glass substrates using spray-pyrolysis technique. The precursor solution consisted of nickel nitrates hyxahydrate $(Ni(NO_3)_2.6H_2O)$ and thiourea $[CS(NH_2)_2]$ with a molar ratio of 1:3, dissolved in 150 ml of ionized water. A few drops of acitic acid were added for complete dissolution. The substrate temperature was fixed at 300 ± 5 °C, prior to deposition. Compressed air was used as vector gas to produce aerosol particles; the flow rate was maintained at 0.5 bar. The distance between the nebulizer and the substrate was set at 40 cm. The precursor concentration was varied as: 0.03, 0.05 and 0.07 M. In order to achieve uniform deposits, the spray gun of the nebulizer is connected to a manually operated stepper motor to control the position of the spray in the plane (X,Y). After deposition, the films were slowly cooled down to room temperature under ambient air, and then the samples were removed for processing or packaging. The characterization was conducted on the film without thermal treatment. The film thickness was estimated using the weight method, which yields the thickness according to the formula [10]:

$$e = \frac{m}{\rho \times S} ....(IV.1)$$

where e is the film thickness; m the mass deposited onto substrate; S the area of the film and ρ is the density of NiS (5.50 g/cm^3 [11]).

Table IV.1: Thin film deposition conditions.

Precursor Concentration (mol/l)	molar ratio Ni/S	Substrate temperature (°)	Distance (cm) (substrate- nozzle)	Flow of the solution (ml/min)
0.03	3	300	25	15
0.05	3	300	25	15
0.07	3	300	25	15

IV.2.2. Characterization

The structural study was carried out using an X-ray diffractometer (DRX, Mini Flex-Rigaku) with a Cu-K$_\alpha$ radiation (λ= 1.5418 Å) in the range of 20 – 60°, using the Brentano Bragg geometry. A dual-beam UV-visible spectrophotometer (UV-3101; Shimadzu), was used to measure the transmittance and reflectance in the wavelength range of 300 – 1100 nm with a resolution of 5 nm. The morphology of the surface was analyzed using an electron microscopy scanning (SEM; Qanta 350) equipped with an energy dispersive spectrometer (EDS) for elementary analysis. The type of chemical bonds present in the samples was identified using an infrated transmission spectrometer (FTIR; Shimadzu, model IR Affinity-1) in the range of 400-4000 cm^{-1}. The surface roughness of the films was analyzed using an atomic microscopic force (AFM; SPI 3800N). The electrical measurements were recorded using the two-probe method with GW-Instek 821-LCR Meter in the temperature range of 300–380 K. For the high frequency impedance measurements, we used Agilent 4284A LCR-meter.

IV.3. Results and Discussion

IV.3.1. Structural analysis

Figure IV.1 shows the X-ray diffraction diffractograms (XRD) of NiS films deposited with different molar concentrations (0.03, 0.05 and 0.07 M). The data reveals that the obtained films are polycrystalline and crystalize in a hexagonal structure strongly oriented along [010]. The intensity of the reflections on these planes are greater than the other diffraction peaks corresponding to (011), (012) and (110) plans. The X-ray patterns obtained in this study are also in a good agreement with the previous reports reported in the literature on NiS films prepared by spray-pyrolysis technique [3]. The X-ray patterns of films were indexed according to the JCPDS card #98-064-6340. We observed an increase in the intensity of the diffraction peak with increasing the precursor concentration; thus, suggesting an improved crystal growth and orientation of the film. On the other hand, we noticed a shift of the reflection peak (010), towards small angles followed by a shift towards large values as the concentration increases. This indicates that the precursor concentration has an effect on the structural parameters of the films.
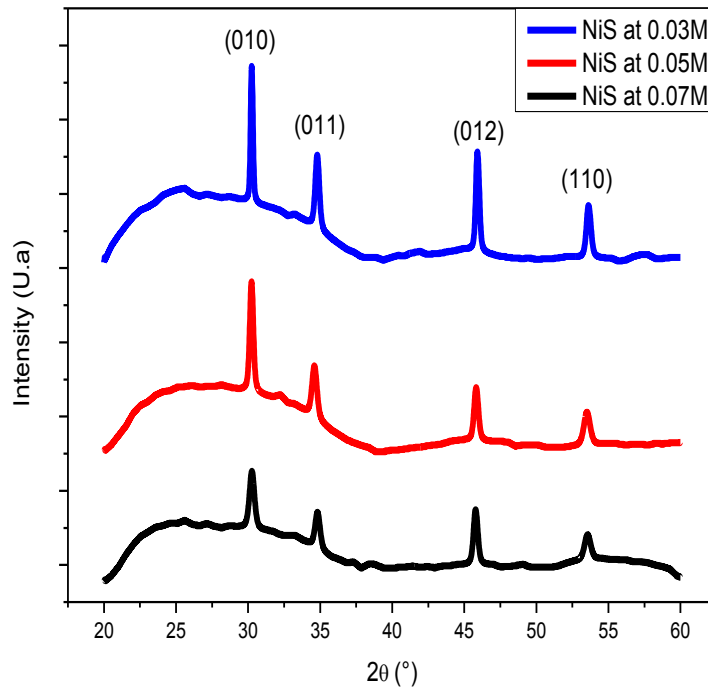
Figure IV.1: XRD patterns of NiS thin films prepared with various concentration.

The unit cell parameters a, b and c of hexagonal NiS were determined using the following formula [12]:

$$\frac{1}{d_{hkl}^2} = \frac{3}{4}\left(\frac{h^2+k^2+hk}{a^2}\right)+\frac{l^2}{c^2}\ldots\ldots\ldots\ldots\ldots(IV.2)$$

The inter-plans distance (d_{hkl}) was calculated by Bragg formula [13]:

$$2d_{hkl}\sin\theta = n\lambda\ldots\ldots\ldots\ldots\ldots(IV.3)$$

Table IV.2 resumes the obtained values of the structural parameters compared to those of the corresponding JCPDS card. It is observed that the reported values of the films are very close to each others. Furthermore, the unit cell volume increases with the increase in the concentration, owing to an improved crystal growth in the films [14]. Table IV.3 summarizes the inter-plans distances determined from the XRD patterns. The observed mismatch between the inter-plans distances indicates the formation of strained lattice with the development of micro-stress during crystallization of the films.

Table IV.2: Lattice parameters (a, b and c) and the unit cell volume V compared to those values of the JCPDS card #98-064-6340.

| Precursor concentration | Latice parameters | | | | | | Unit cell volume ($\mathring{A}^3$) |
| | Our data | | | JCPDS card | | | |
	a=b ($\mathring{A}$)	c ($\mathring{A}$)	c/a	a=b ($\mathring{A}$)	c ($\mathring{A}$)	c/a	
0.03 M	3.403	5.305	1.559				53,239
0.05 M	3.417	5.314	1.554	3.420	5.300	1.55	53,769
0.07 M	3.422	5.312	1.552				53,906

Table IV.3: Inter-planar distances (d_{hkl}) of NiS thin films.

Precursor concentration	0.03 M	0.05 M	0.07 M
d_{010} ($\mathring{A}$)	2.953	2.956	2.954
d_{011} ($\mathring{A}$)	2.577	2.592	2.578
d_{012} ($\mathring{A}$)	1.982	1.980	1.976
d_{110} ($\mathring{A}$)	1.711	1.713	1.709

The texture coefficient (TC_{hkl}), which is calculated in terms of the intensity of each orientation (I_{hkl}) to the corresponding intensity of the JCPDS card (I_{0hkl}), gives information on the probability of the growth according to an orientation [hkl]. The coefficient (TC_{hkl}) is given by the following relation [14]:

$$TC_{hkl} = \frac{I_{hkl} / I_{0hkl}}{N^{-1}\left(\sum_{i=1}^{n} \frac{I_{hkl}}{I_{0hkl}}\right)} \dots\dots\dots\dots\dots(IV.4)$$

where: N is the number of diffraction peaks. The obtained values of TC_{hkl} are gathered in Table IV.4. As we can see, the value of the largest texture coefficient with respect to all the films corresponds to the peak (010), which indicates that it is the preferred orientation.

Hence, the peak (010) has the highest intensity when compared to the other peaks. The crystallites are predominantly parallel to the plane of the substrate.

Table IV.4: Texture coefficient (TC_{hkl}) of NiS thin films prepared with various concentration.

Precursor concentration	0.03 M	0.05 M	0.07 M
TC_{010}	1.428	1.683	1.623
TC_{011}	1.084	0.818	0.705
TC_{012}	0.978	0.803	1.028
TC_{110}	0.508	0.695	0.642

The crystallite size (D_{hkl}) was estimated for all diffraction peaks using Scherer formula [15]:

$$D_{hkl} = \frac{k \times \lambda}{\beta_{1/2} \, COS\theta} \dots\dots\dots\dots\dots (IV.5)$$

where: k is a constant (k = 0.90), $\beta_{1/2}$ the full width at half maximum of the diffraction peak, θ is the Bragg angle and λ= 1.5406 Å is the wavelength of the X-ray radiation used.

Table IV.5: The crystallites size (D_{hkl}) *of NiS thin films.*

Precursor concentration	0.03 M	0.05 M	0.07 M
D_{010} (nm)	22.4	32.0	56.0
D_{011} (nm)	22.7	22.6	28.3
D_{012} (nm)	29.3	29.3	39.1
D_{110} (nm)	20.2	20.2	30.3

The dislocation density (δ_{hkl}), which measures the amount of defects in a crystal is defined by the length of dislocation lines per unit volume. It was determined using the following formula [16]:

$$\delta_{hkl} = \frac{1}{D_{hkl}^2} \dots\dots\dots\dots\dots\dots(IV.6)$$

Table IV.6: Dislocation density (δ_{hkl}) of NiS thin films.

Precursor concentration	0.03 M	0.05 M	0.07 M
δ_{010} (10^{15} lines/ m^2)	1.989	0.974	0.318
δ_{011} (10^{15} lines/ m^2)	1.944	1.946	1.244
δ_{012} (10^{15} lines/ m^2)	1.160	1.159	0.652
δ_{110} (10^{15} lines/ m^2)	2.451	2.452	1.089

On the other hand, the microstrain (ε_{hkl}), was estimated using the following formula [17]:

$$\varepsilon_{hkl} = \frac{\beta_{1/2}}{4 \tan \theta} \dots\dots\dots\dots\dots\dots(IV.7)$$

where: $\beta_{1/2}$ the full width at half maximum of the diffraction peak, θ is the Bragg angle.

Table IV.7: Micro-stress values (ε_{hkl}) of NiS thin films.

Precursor concentration	0.03 M	0.05 M	0.07 M
ε_{010} (10^{-3})	6.355	4.452	2.542
ε_{011} (10^{-3})	5.481	5.517	4.388
ε_{011} (10^{-3})	3.256	3.253	2.434
ε_{110} (10^{-3})	4.088	4.091	2.721

The average crystallites size $\prec D \succ$, average micro-stress $\prec \varepsilon \succ$ and the average dislocation density $\prec \delta \succ$ of the films, can be determined using the following formulas [17-19]:

$$\begin{cases} \prec D \succ = \dfrac{\sum TC_{hkl} \times D_{hkl}}{n} \quad\text{...........................}(IV.8) \\[3mm] \prec \varepsilon \succ = \dfrac{\sum TC_{hkl} \times \varepsilon_{hkl}}{n} \quad\text{............................}(IV.9) \\[3mm] \prec \delta \succ = \dfrac{\sum TC_{hkl} \times \delta_{hkl}}{\sum TC_{hkl}} \quad\text{...........................}(IV.10) \end{cases}$$

Table IV.8: The average values of $\prec D \succ$, $\prec \varepsilon \succ$ and $\prec \delta \succ$ of NiS thin films.

Precursor concentration	$\prec D \succ$	$\prec \varepsilon \succ \left(10^{-3}\right)$	$\prec \delta \succ$ (10^{15} lines/m^2)
0.03 M	23.903	5.072	1.831
0.05 M	27.519	4.367	1.462
0.07 M	42.687	2.869	0.691

It is evident that the micro-stress and the dislocation density decrease with increasing the precursor concentration, inferring the formation of high quality thin films [20]. Acoordingly, the average crystallites size increases. This may be due to the fact that small crystallites are consumed during crystallization. Whereas, the dislocations acquire more energy and exhibit higher mobility. These activated dislocations segregate towards the grains boundaries and are neutralized as the crystallization of the film proceeds [21].

IV.3.2. Optical properties

Figure IV.2 shows the transmittance spectra of NiS films prepared with various concentrations (0.03, 0.05 and 0.07 M). We observed an enhancement in the transparence of the film above 400 nm owing to a reduced scattering effect and propagation losses. Also, the transmittance decreases with the increase of the precurssor's concentration. This behavior can be correlated with the AFM results (section 3.5); an increase in surface roughness with an increase in the concentration leads to an improvement of the scattering of radiations and hence, a decrease in the optical transmittance of the films [22]. The average optical transmittance is 1.71, 1.56 and 1.26 % for the films prepared with 0.03, 0.05 and 0.07 M, respectively.
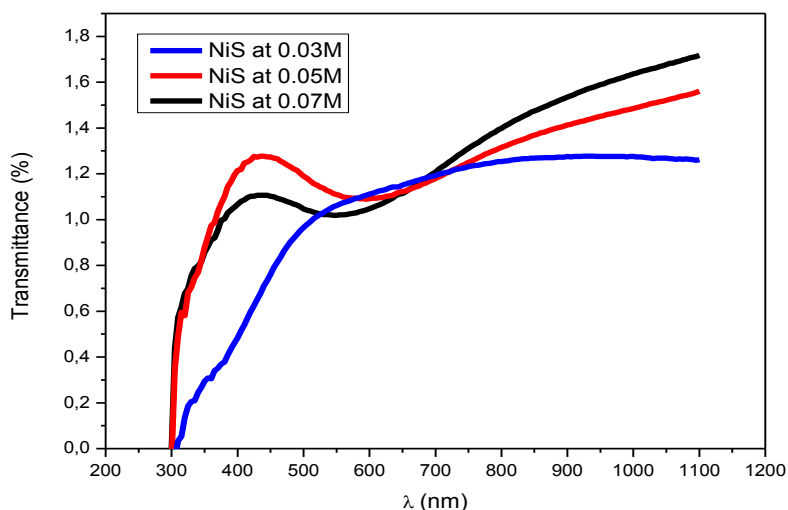
Figure IV.2: UV-visible transmittance spectra of NiS thin films prepared with various concentration.

Figure IV.3 shows the reflectance spectra of NiS films prepared with various concentrations. It is seen that the reflectance decreases with the increase of the precurssor's concentration, owing to an increase in the thickness of the films [23]. The average optical reflectance is 2.69, 1.87 and 1.48 % for the films prepared with 0.03, 0.05 and 0.07 M, respectively. Furthermore, it is observed that the reflectance is higher than the corresponding transmittance of the films. This phenomenon can be related to the oscillation of the free carriers plasma, depicting the metallic behavior of the film [3].
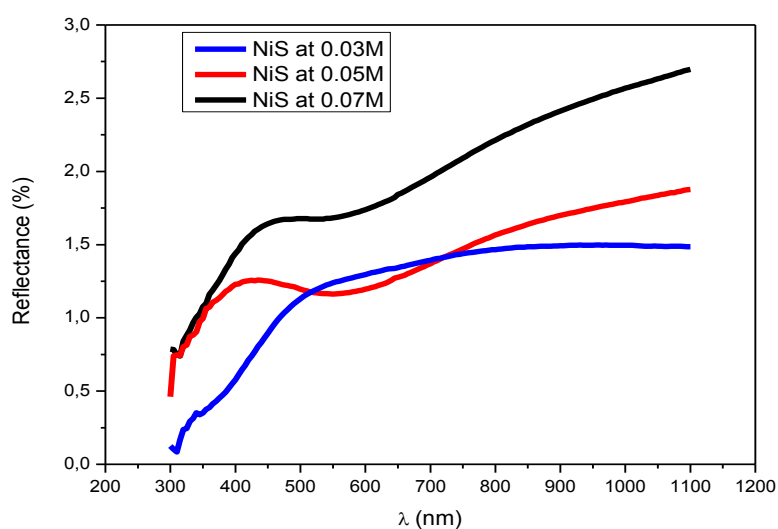
Figure IV.3: Reflectance spectra of NiS thin films prepared with various concentration.

From the transmittance and reflectance spectra, the absorption coefficient (α), is given by the following formula [17]:

$$\alpha = \frac{1}{e}\ln\left(\frac{(1-R)^2}{T}\right) \quad.....................(IV.11)$$

where: e is the film thickness, T the transmittance and R the reflectance. Figure IV.4 presents the variation of the absorption coefficient (α) as a function of wavelength (λ). The average absorption coefficient is 3.70×10^4, 3.11×10^4 and 3.07×10^4 cm^{-1} for the films prepared with 0.03, 0.05 and 0.07 M, respectively. The observed decrease when increasing the precursor concentration is due to the improvement of the cristalinty of the films, removal of defects and the reduction of the grain boundaries density. In addition, the absorption coefficient values are close to those values reported in literature [24].
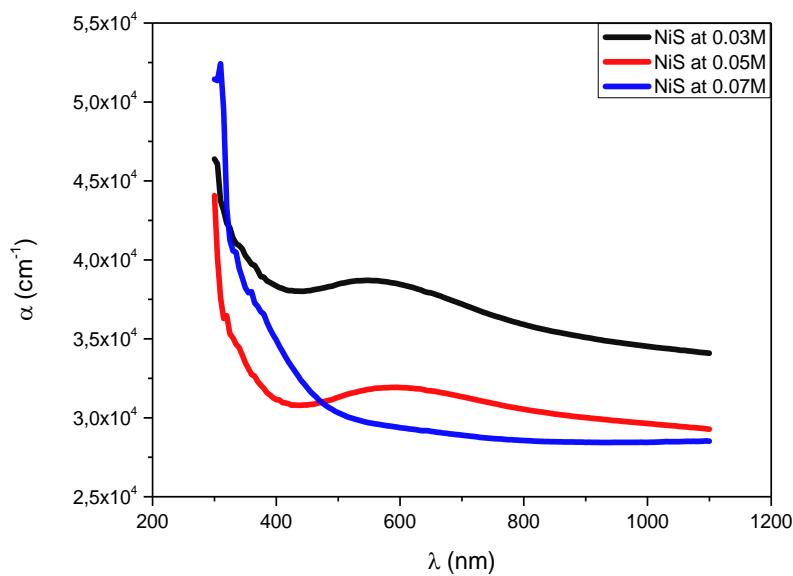
Figure IV.4: Evolution of the absorption coefficient (α) of NiS thin films.

The optical band gap of the material was determined using the following formula [25]:

$$\alpha h\nu = B\left(h\nu - E_g\right)^p \quad.....................(IV.12)$$

where: B is a constant, hv the photon energy, p is an integer that takes the value 1/2 or 2 for direct or indirect transitions, respectively. Figure IV.5 shows the plots $(\alpha h v)^2$ versus energy (hv) of NiS films prepared with various concentration. The linear extrapolation of the curve yields the intersection point with the abscissa axis, which corresponds to the energy of the optical transition.

The optical band gap of the film was found to be 1.07, 1.01 and 0.96 eV for the films prepared with 0.03, 0.05 and 0.07 M, respectively. The observed decrease when increasing the concentration may be due to the enhanced crystallinity and the change in the Ni/S ratio in the film (section 3.3), leading to a change in the density of states (DOS) of the conduction and valence bands [26].
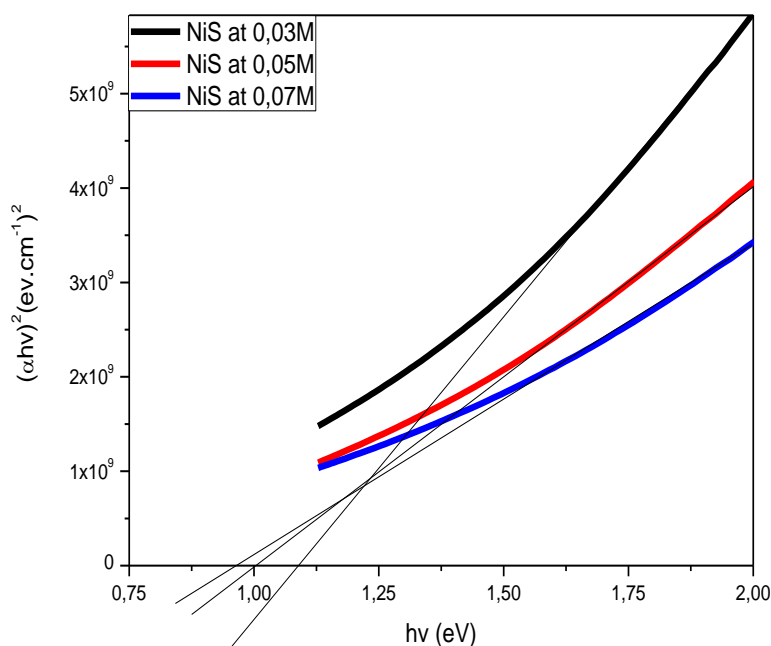
Figure IV.5: $(\alpha h v)^2$ vs. hv of NiS thin films.

IV.3.3. SEM and EDS analysis

The analysis of the morphology with a scanning electron microscope (SEM), allows examining the homogeneity, the grains shape and aggregates, as well as the quantitative analysis of the films using an energy dispersive spectrometer (EDS). Figure IV.6 (a-c) shows the SEM and EDS micrographs of NiS films prepared with various concentrations.

(a)

(b)

(c)
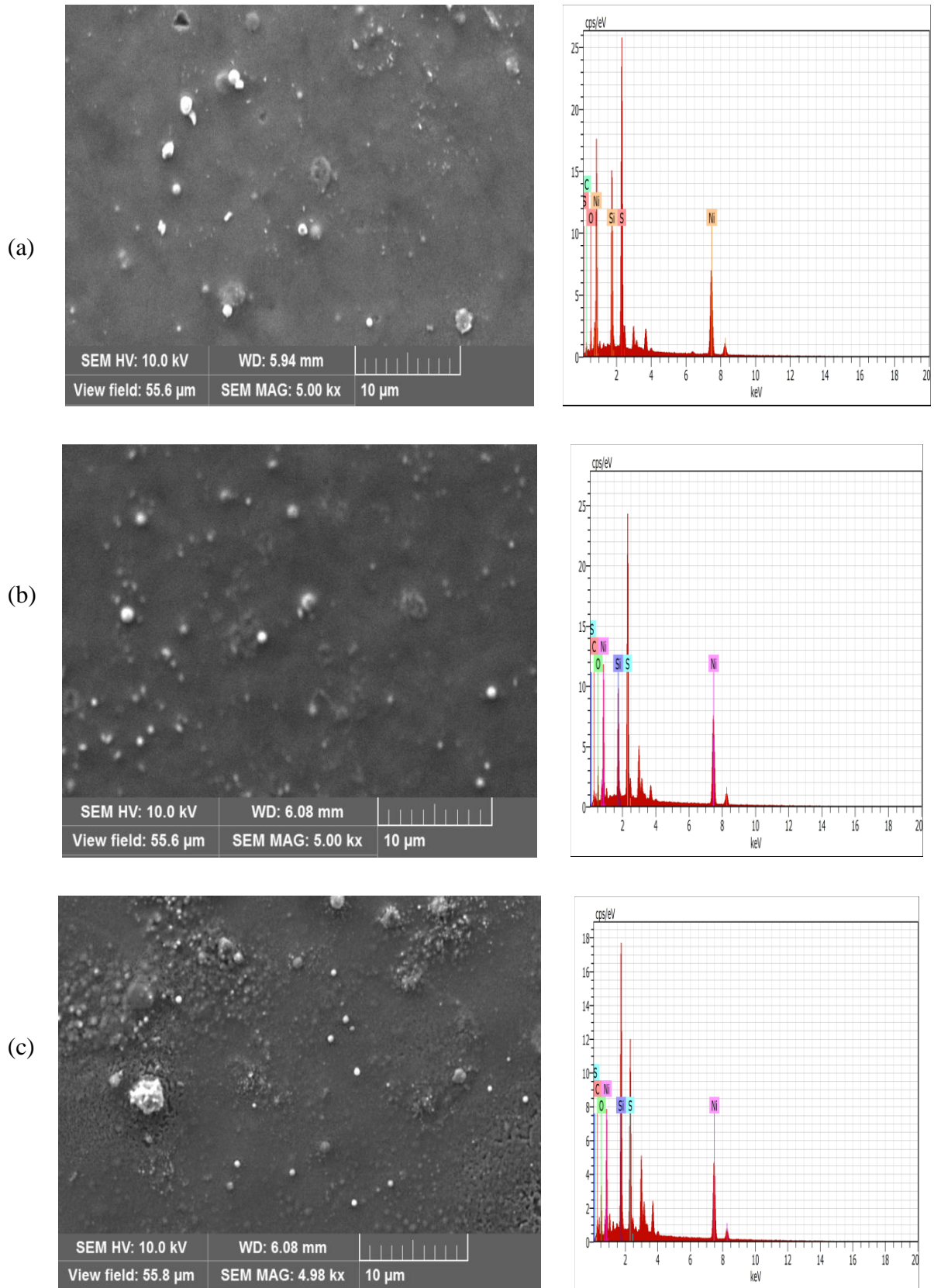
Figure IV. 6: SEM and EDS micrographs of NiS thin films prepared with various concentrations (a): 0.03 M, (b): 0.05M and (c): 0.07 M.

It is observed that the films surface is rough, dense and granular. In addition, it contains protrusions and bubbles with a random distribution. The average bubbles diameter increases when increasing the precursor's concentration. On the other hand, the SEM images also reveal in some areas the presence of bubble explosions accompanied by ejection of matter. This indicates that there was a volume formation of a gas phase during the growth of the film, which causes the emergence of bubbles on the surface.

The EDS spectra of the films confirm the presence of the two elements Ni and S with different concentrations. Furthermore, the analysis showed the presence of other elements in the spectra such as oxygen (O) and silicon (Si) which originate from the SiO_2 glass substrate. While the presence of carbon C is probably due to thiourea ($SC(NH_2)_2$) involved in the synthesis. It is observed that the atomic percentage of sulfur increases with the increase of the precursor's concentration, suggesting that the surfaces of the films are sulfur rich. Table IV.9 summarizes the results of the elementary analysis. Also, it is pertinent to note that the sulphur concentration increases when the oxygen concentration decreases.

Table IV.9: Elementary analysis of NiS thin films.

Precursor concentration	Ni (at. %)	S (at. %)	C (at. %)	O (at. %)	Si (at. %)	(Ni/S)
0.03 M	18.15	24.31	31.58	13.27	12.68	0.74
0.05 M	19.34	20.48	35.49	17.04	7.66	0.94
0.07 M	15.82	11.47	38.88	20.19	13.64	1.37

IV.3.4. FTIR analysis

The Fourier transform infrared spectroscopy (FT-IR), is known as one of the useful methods to get insights on the chemical bonding and identify the material elemental constituents. Figure IV.7 shows the FT-IR spectra of NiS films prepared with 0.03, 0.05 and 0.07 M. The peak observed at 665 cm^{-1} is attributed to Ni-S stretching vibration [27-30]. The bands nearby 881 and 1037 cm^{-1} are attributed to C-S bonds vibrations [18, 28, 29]. The band at 2363 cm^{-1} is due to C=O stretching vibration of adsorbed CO_2 from

ambient atmosphe [31]. The bands observed at 1454 and 2922 cm^{-1} are assigned to C-H vibrations [27, 31, 32]. The absorption bands observed at 1615 and 3430 cm^{-1} corresponding to the vibration of O-H bonds indicate the presence of adsorbed H_2O molecules [33].
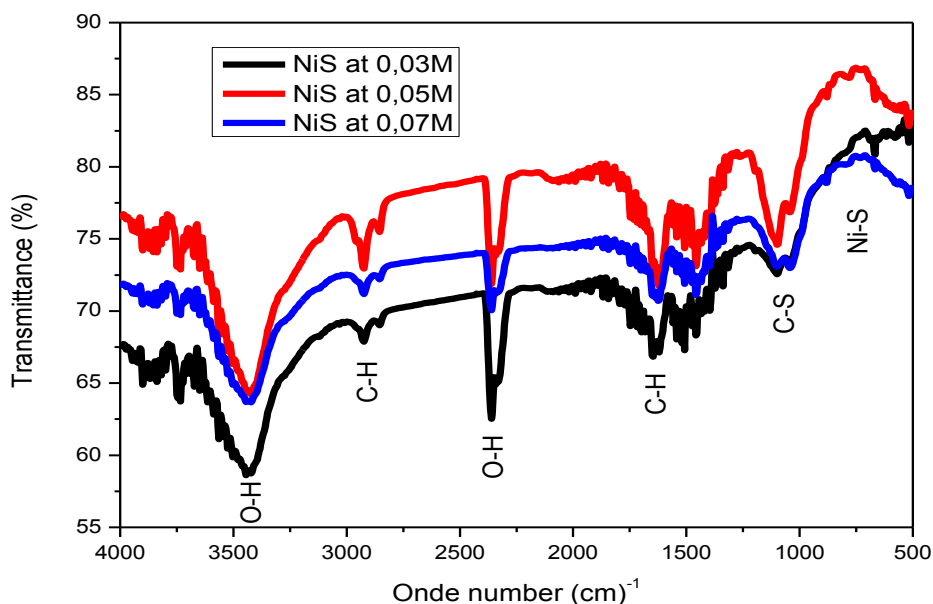
Figure IV.7: FTIR spectra of NiS thin films prepared with various concentrations.

IV.3.5. AFM analysis

The surface roughness is an important physical parameter in some properties, especially optical scattering. Figure IV.8 (a-c) shows 2D and 3D micrographs of the NiS surface, recorded in a scanning area of 1×1 µm². It is observed that the film was homogenously deposited without micro-cracks. The surface depicts a granular morphology with the formation of clusters of spherical shaped crystallites.
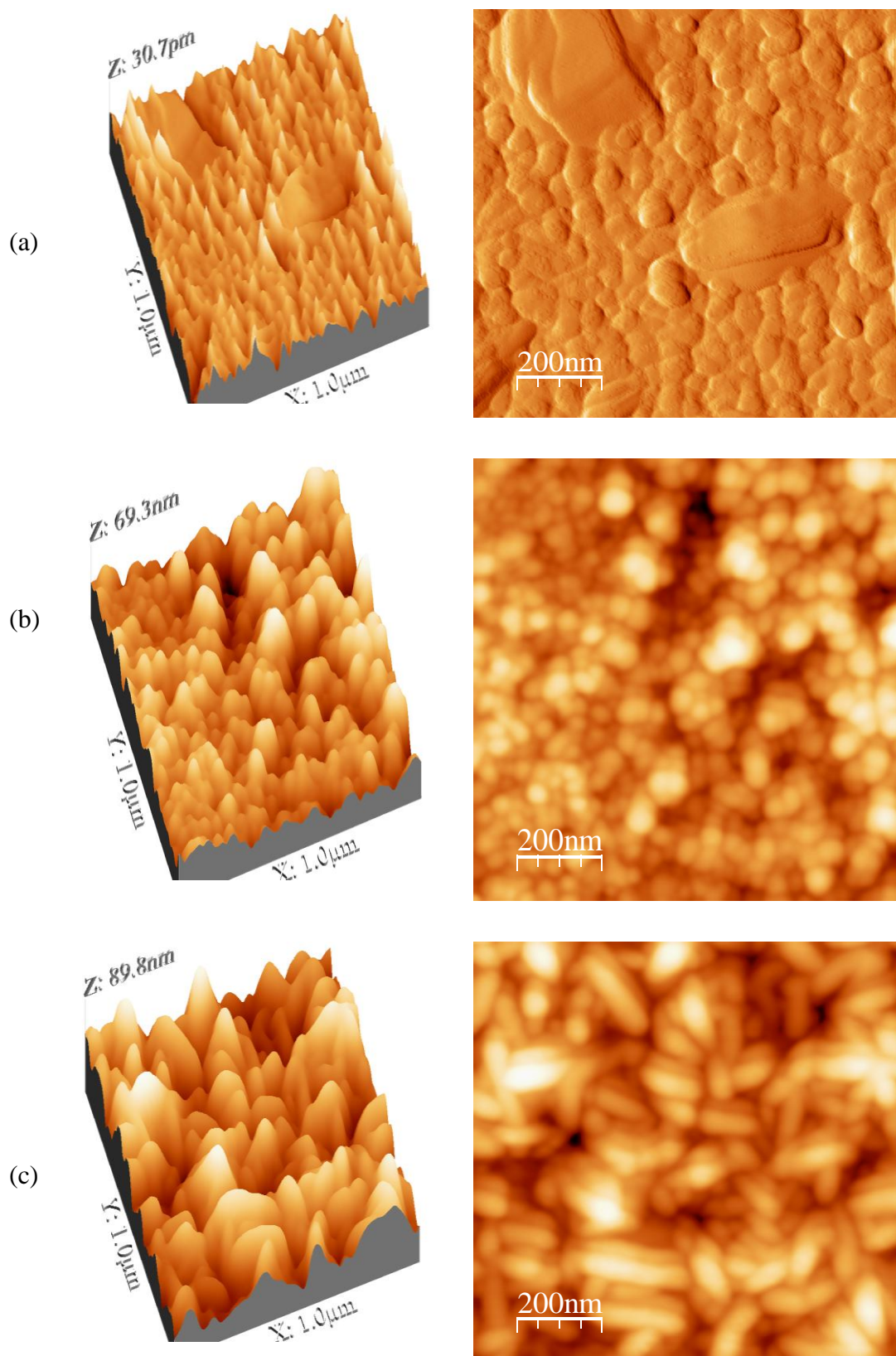
Figure IV.8: AFM micrographs of NiS thin films prepared with various concentrations (a): 0.03 M, (b): 0.05M and (c): 0.07 M.

Figure IV.8 (a-b) show clusters having a spherical shape on the surface of NiS films prepared with 0.03 M and 0.05 M. In addition, Figure IV.8-c shows the 2D and 3D micrographs of the NiS film prepared with 0.07 M; the grains are arranged like nanowires. This is compatible with the structural study. In fact, the XRD analysis showed that the films crystallize in a hexagonal structure; where the growth occurs along the c-axis. This can be at the origin of the formation of these nanowires.

The analysis of the surface profile yields the average roughness (R_a) and root mean square roughness (R_{RMS}). These parameters are defined as follows [14]:

$$\begin{cases} R_a = \frac{1}{l}\int_0^l |Z - Z_i|\,dx \dots\dots\dots\dots\dots\dots\dots(IV.13) \\ R_{RMS} = \sqrt{\frac{1}{l}\int_0^l |Z - Z_i|^2\,dx} \dots\dots\dots\dots\dots(IV.14) \end{cases}$$

where: l is the length of the sample, Z_i is the height reference and Z the profile value. Table IV.10 resumes the obtained values. It is clear from AFM analysis that particle size and surface roughness depend on the precursor's concentration.

Table IV.10: Morphology parameters (R_a: average roughness, R_{RMS}: root mean square roughness) of NiS thin films.

Precursor concentration	R_{RMS} (nm)	R_a (nm)
0.03 M	3.5	2.5
0.05 M	9.5	7.5
0.07 M	13.9	11.2

IV.3.6. Electrical studies

The electrical measurements were conducted only on the film prepared with 0.05 M. It seems that the electrical current in the films perpared with the two other concentration was very high and exeeds the limit of the instrument used in our study. Therfore, no data

were recorded for these two samples. Figure IV.9 depicts the temperature dependence of the ac-conductivity (σ_{ac}). As can be seen, σ_{ac} increases with the increase in the temperature from 1.97×10^3 S/cm (at 310 K) to 2.24×10^3 S/cm (at 378 K). This behavior is typical in semiconducting materials according to Arrhenius law. The ac-conductivity is expressed by:

$$\sigma = \sigma_0 \, Exp\left(-\frac{E_a}{kT}\right) \dots\dots\dots\dots\dots\dots\dots(IV.15)$$

where k is the Boltzmann constant and T the absolute temperature. The linear fit of the curve of log (σ_{ac}) vs. 1000/T, yields an activation energy (E_a) of 26.7 meV.
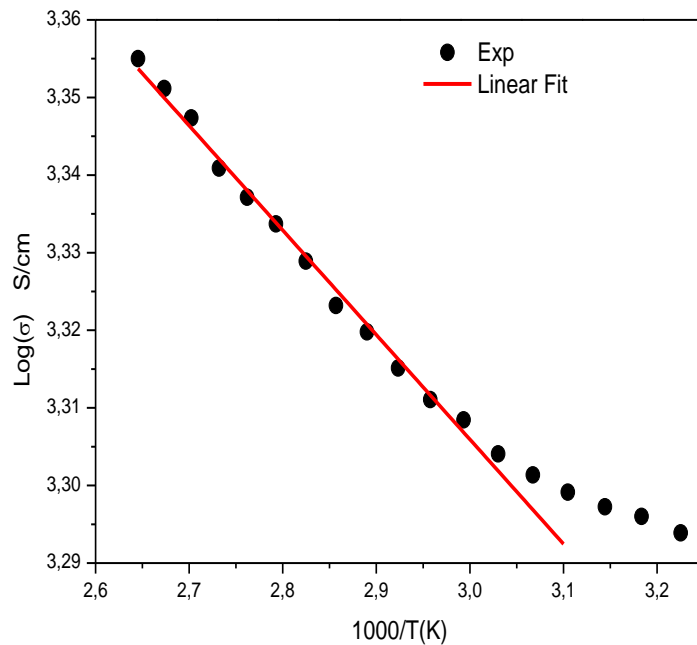
Figure IV.9: Temperature dependence of the ac-conductivity of the NiS film prepared with 0.05 M.

The deviation at low temperatures from the linear behavior is correlated with the extrinsic conductivity in the film [34]. Furthermore, the observed values of electrical conductivity agree well with the reported values in literature [35, 36].
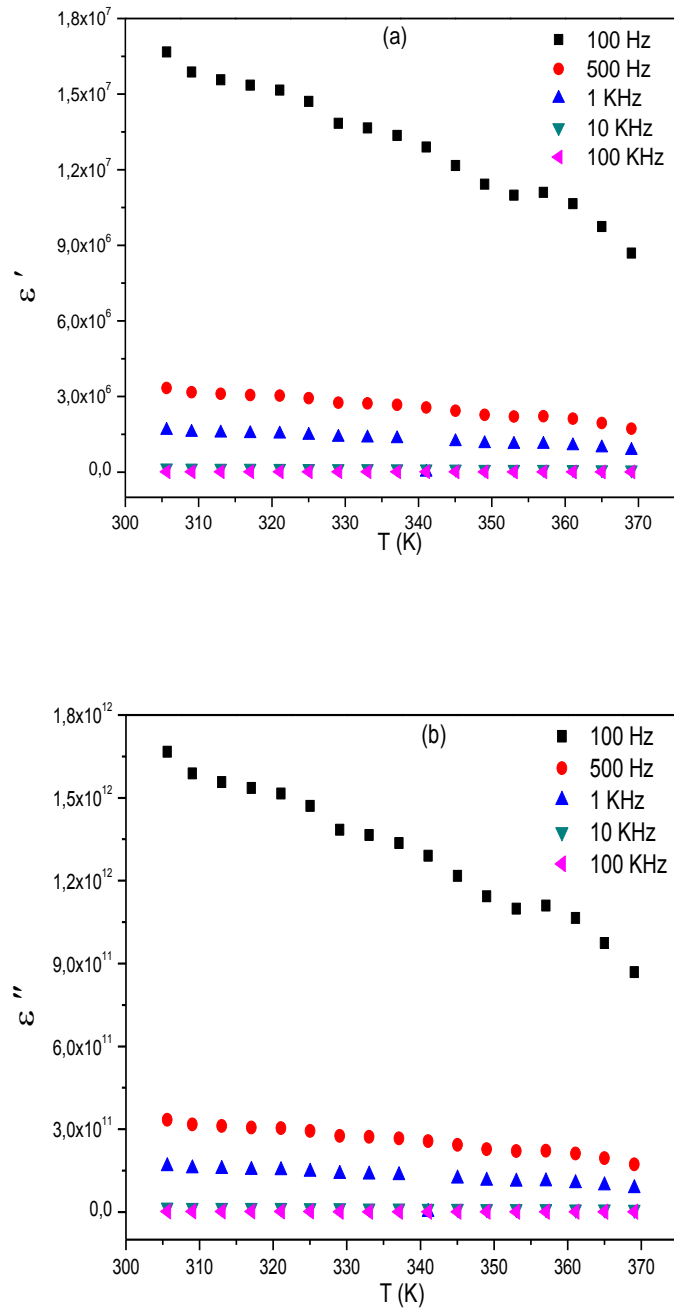
Figure IV.10: Temperature dependence of the dielectric constant components, (a) real part (ε') and (b) imaginary part (ε") of the NiS film prepared with 0.05 M.

Figure IV.10 (a) and (b) present the temperature dependence of the real (ε') and imaginary (ε'') parts of the dielectric constant, recorded at fixed frequencies. The constant (ε') decreases with the increase of the temperature and frequency. The higher values of the

dielectric constant can be explained on the basis of an interfacial space-charge polarization due to inhomogeneous dielectric structure grains/grains boundaries. The resulting polarization is expected to promote the depletion layer at the inter-granular contact [37].

On the other hand, the observed decease with the increase in the frequency is because that the dipoles are no longer being able to rotate as rapid as needed. Therefore, their oscillation begins to lay behind the frequency of the applied field [38].
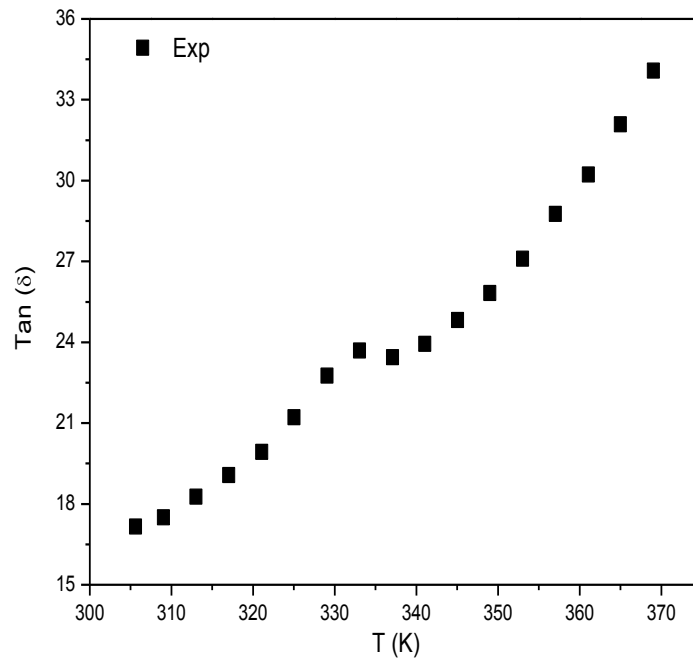
Figure IV.11: Dielectric loss tangent recorded at 100 KHz of the NiS film prepared with 0.05 M.

Figure IV.11 shows the temperature-frequency dependence of the dielectric loss tangent $\left(\tan(\delta) = \dfrac{\varepsilon''}{\varepsilon'} \right)$, recorded at 100 KHz. The dispersion exhibits a relaxation process induced by thermal dipoles polarization. This relaxation is due to space-charge polarization coming from the electrically heterogeneous microstructure grains/grain boundaries of the film. Figure IV.12 presents the variation of the capacitance of the film as a function of temperature. It is observed that the capacitance deceases from 115 to 29 mF/cm² with increasing temperature.
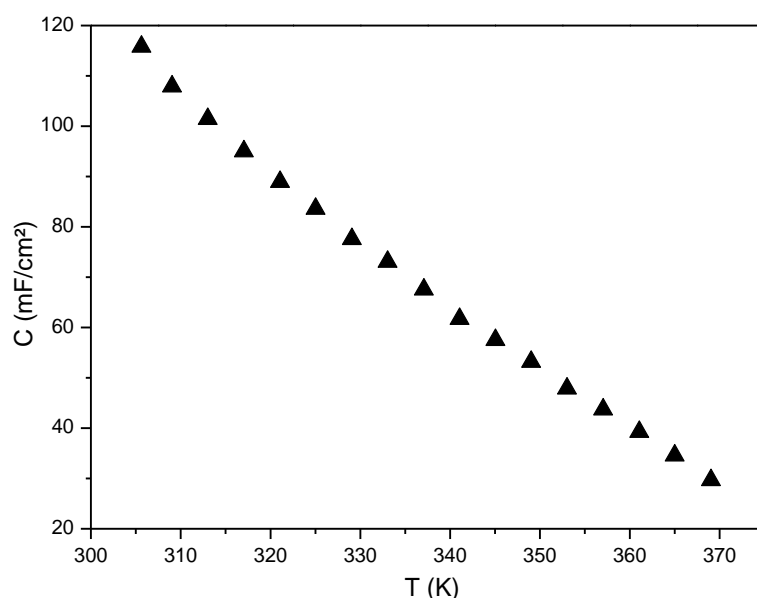
Figure IV.12*: Capacitance of the NiS film prepared with 0.05 M recorded as a function of temperature.

Figure IV.13 depicts the room temperature impedance diagram (imaginary part *vs.* real part : $Z'' = f(Z')$). The analysis of the impedance data reveals two distinct behaviors strongly related to the microstructure of the film. The fitting parameters of the equivalent circuit used to depict the behavior of the film as summarized in Table IV.11.
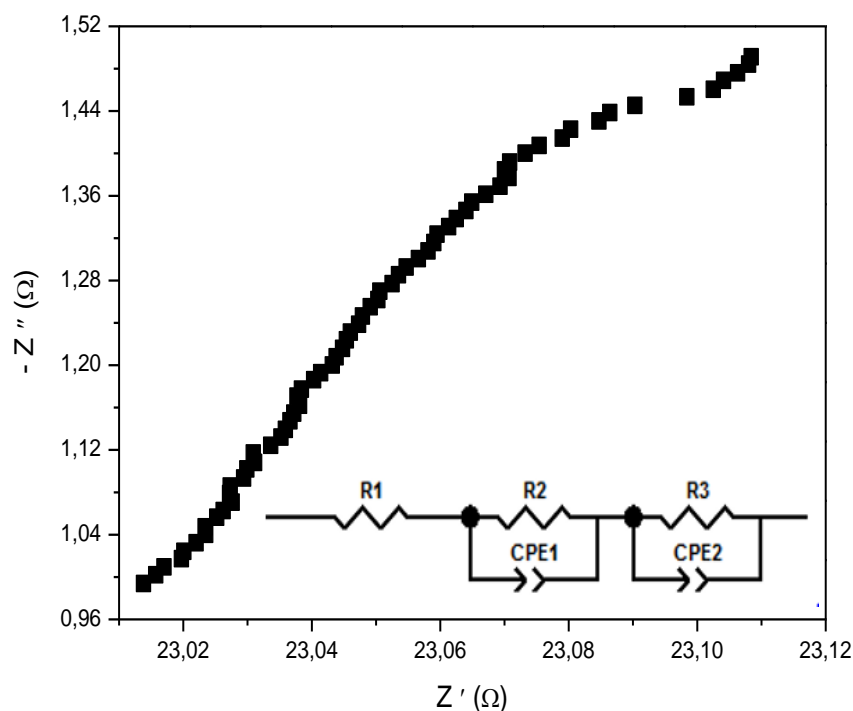
Figure IV.13*: Impedance diagram of the NiS film prepared with 0.05 M.

The following formulas give the electrical equivalent circuit used to model the measured impedance (Z) depending on the frequency:

First behavior: Observed in the frequency range above 69.5 KHz.

$$Z_{HF}(f) = R1 + \frac{R2}{1 + R2 \times \left(CPE_1\right) \times (2\pi jf)^{\beta_1}} \quad \text{..................}(IV.16)$$

where: f is the frequency of the external field, CPE_1 the capacitance of the constant phase element (CPE) and β_1 the phase angle. The resistance R_1 is ascribed to the resistance of the charge transfer at the ohmic contact while R_2 is ascribed to the bulk resistance. Moreover, the ideal capacitive behavior is commonly given by:

$$Z_{HF}(f) = R1 + \frac{R2}{1 + (2\pi jf)\ R2.C} \quad \text{.............................}(IV.17)$$

The deviation from the pure capacitor behavior in the bulk is related to localized states, which mediates the charge transfer at the semiconductor interface [39].

Second behavior: Observed in the range of the frequency below 69.5 KHz.

$$Z_{MF}(f) = \frac{R3}{1 + R3 \times \left(CPE_2\right) \times (2\pi jf)^{\beta_2}} \quad \text{.............................}(IV.18)$$

where β_2 is the angle of the phase, CPE_2 is the capacitance of the element of the constant phase, R_1, R_2 and R_3 are the resistances in sequences. The element of the constant phase CPE $\left(const.(j.\omega)^{-n}\right)$ where the homogeneity factor n ($0 < n \leq 1$) depends to the phase angle (φ = n. $\pi/2$), represents the contribution of the grains boundaries with non-ideal capacitive behavior induced most likely, by the surface states and the porous nature of the film [40].

Table .IV.11. Circuit parameters of the NiS film prepared with 0.05 M, where: R_1, R_2 and R_3 are the resistances in sequences, CPE_1 *and* CPE_2 the constant phase elements capacitance, β_1 and β_2 the phase angles.

Element	R1 (Ω)	R2 (Ω)	$CPE_1\left(mF.s^n\right)$	$\beta_1(°)$	R3 (Ω)	$CPE_2\left(mF.s^n\right)$	$\beta_2(°)$
Value	21.5	0.5	13	22.9	3.5	29.8	48.7

IV.4. Conclusion

In this work, we have investigated the effect of the precursor concentration on the morphological, optical and structural properties of NiS films deposited by spray-pyrolysis technique.

The XRD results showed that the deposited films are single-phase and polycrystalline, having the hexagonal structure with high intense peaks along [010] direction. The crystallite size was found to increase when increasing the precursor's concentration to reach 42.7 nm in the film prepared with 0.07 M. In addition, the data revealed that the structural parameters depend also on the concentration.

The analysis of the optical properties showed that the optical band gap decreases from 1.07 to 0.96 eV when increasing the concentration.

The FTIR analysis showed the characteristic vibrationel bands of NiS. The elemental composition analysis revealed that the atomic ratio Ni/S increases in the film when increasing the precursor's concentration from 0.94 to 1.37.

The AFM analysis revealed that nanometer-sized spherical grains cover the entire surface of the films prepared with 0.03 and 0.05 M; while the film prepared with 0.07 M depicted the formation of nanowires.

The SEM images revealed that it is possible to obtain NiS films, which are dense, homogeneous and granular under the synthesis conditions used.

The electrical conductivity of the film prepared with 0.05 M, is 1.97×10^3 S/cm and the capacitance is about 115 $\mu F/cm^2$ at room temperature.

The NiS thin films prepared in this study are a good candidate as an electrode material for application in supercapacitors.

References

[1]   S. H. Yu and M. Yoshimura, "Fabrication of Powders and Thin Films of Various Nickel Sulfides by Soft Solution Processing Routes," Advanced Functional Materials, vol. 12, pp. 277-285, 2002.

[2]   Y. Zhang, Z. Peng, S. Guan, and X. Fu, "Data on the synthesis processes optimization of novel beta-NiS film modified CdS nanoflowers heterostructure nanocomposite for photocatalytic hydrogen evolution," Data Brief, vol. 16, pp. 828-842, Feb 2018.

[3]   R. Boughalmi, R. Rahmani, A. Boukhachem, B. Amrani, K. Driss-Khodja, and M. Amlouk, "Metallic behavior of NiS thin film under the structural, optical, electrical and ab initio investigation frameworks," Materials Chemistry and Physics, vol. 163, pp. 99-106, 2015.

[4]   S. Suresh, S. S. Anand, R. Arul, and D. Isha, "Structural, morphological, optical and electrical properties of Nickel Sulphide Thin Films," Chalcogenide Letters, vol. 13, pp. 291-299, 2016.

[5]   A. Patil, A. Lokhande, P. Shinde, J. Kim, and C. Lokhande, "Vertically aligned NiS nano-flakes derived from hydrothermally prepared Ni (OH) 2 for high performance supercapacitor," Journal of energy chemistry, vol. 27, pp. 791-800, 2018.

[6]   S. Sartale and C. Lokhande, "Preparation and characterization of nickel sulphide thin films using successive ionic layer adsorption and reaction (SILAR) method," Materials Chemistry and Physics, vol. 72, pp. 101-104, 2001.

[7]   R. K. Singh and J. Narayan, "Pulsed-laser evaporation technique for deposition of thin films: Physics and theoretical model," Physical review B, vol. 41, p. 8843, 1990.

[8]   H. Ruan, Y. Li, H. Qiu, and M. Wei, "Synthesis of porous NiS thin films on Ni foam substrate via an electrodeposition route and its application in lithium-ion batteries," Journal of Alloys and Compounds, vol. 588, pp. 357-360, 2014.

[9]   P. Yang, M. Lü, C. F. Song, G. Zhou, D. Xu, and D. R. Yuan, "Photoluminescence characteristics of NiS nanocrystallites embedded in sol–gel silica xerogel," Journal of Physics and Chemistry of Solids, vol. 63, pp. 2047-2051, 2002.

[10]   V. P. Patil, S. Pawar, M. Chougule, P. Godse, R. Sakhare, S. Sen, and P. Joshi, "Effect of Annealing on Structural, Morphological, Electrical and Optical Studies of

Nickel Oxide Thin Films," Journal of Surface Engineered Materials and Advanced Technology, vol. 01, pp. 35-41, 2011.

[11]   R. Karthikeyan, "Synthesis of Phase Controlled Nickel Sulfide Nanostructures and their Catalytic Applications," 2015.

[12]   B. Bharathi, S. Thanikaikarasan, P. Chandrasekar, P. Kollu, T. Mahalingam, and L. Ixtlilco, "Studies on electrodeposited NiS thin films," Journal of New Materials for Electrochemical Systems, vol. 17, pp. 167-171, 2014.

[13]   M. Patel, I. Mukhopadhyay, and A. Ray, "Molar optimization of spray pyrolyzed SnS thin films for photoelectrochemical applications," Journal of Alloys and Compounds, vol. 619, pp. 458-463, 2015.

[14]   A. Boukhachem, M. Mokhtari, N. Benameur, A. Ziouche, M. Martínez, P. Petkova, M. Ghamnia, A. Cobo, M. Zergoug, and M. Amlouk, "Structural optical magnetic properties of Co doped α-MoO3 sprayed thin films," Sensors and Actuators A: Physical, vol. 253, pp. 198-209, 2017.

[15]   A. Gahtar, A. Rahal, B. Benhaoua, and S. Benramache, "A comparative study on structural and optical properties of ZnO and Al-doped ZnO thin films obtained by ultrasonic spray method using different solvents," Optik, vol. 125, pp. 3674-3678, 2014.

[16]   M. Riahi, C. Martínez-Tomás, S. Agouram, A. Boukhachem, and H. Maghraoui-Meherzi, "The effects of thermal treatment on structural, morphological and optical properties of electrochemically deposited Bi2S3 thin films," Thin Solid Films, vol. 626, pp. 9-16, 2017.

[17]   R. Boughalmi, A. Boukhachem, M. Kahlaoui, H. Maghraoui, and M. Amlouk, "Physical investigations on Sb2S3 sprayed thin film for optoelectronic applications," Materials Science in Semiconductor Processing, vol. 26, pp. 593-602, 2014.

[18]   C. Buchmaier, M. Glänzer, A. Torvisco, P. Poelt, K. Wewerka, B. Kunert, K. Gatterer, G. Trimmel, and T. Rath, "Nickel sulfide thin films and nanocrystals synthesized from nickel xanthate precursors," Journal of Materials Science, vol. 52, pp. 10898-10914, 2017.

[19]   A. Ammari, M. Trari, and N. Zebbar, "Transport properties in Sb-doped SnO2 thin films: Effect of UV illumination and temperature dependence," Materials Science in Semiconductor Processing, vol. 89, pp. 97-104, 2019.

[20] W. Eidelloth and R. Sandstrom, "Wet etching of gold films compatible with high T c superconducting thin films," Applied physics letters, vol. 59, pp. 1632-1634, 1991.

[21] N. K. Reddy, K. Ramesh, R. Ganesan, K. R. Reddy, K. Gunasekhar, and E. Gopal, "Synthesis and characterisation of co-evaporated tin sulphide thin films," Applied Physics A, vol. 83, pp. 133-138, 2006.

[22] F. Hashim and B. Kahdum, "effect of li doping on the structural and some optical studies of cds thin films fabricated by sol–gel technique"," International Journal of Research in Applied, vol. 4, pp. 155-164, 2016.

[23] K. Z. Yahiya, A. H. Jraiz, and U. M. Nayef, "Preparation and the study optical and electrical properties of thin films for optoelectronic applications," Engineering and Technology Journal, vol. 26, pp. 824-828, 2008.

[24] A. Hammad, Z. Elmandouh, and H. Elmeleegi, "Structure and some physical properties of chemically deposited nickel sulfide thin films," Acta Physica Polonica A, vol. 127, pp. 901-903, 2015.

[25] A. Gahtar, S. Benramache, B. Benhaoua, and F. Chabane, "Preparation of transparent conducting ZnO: Al films on glass substrates by ultrasonic spray technique," Journal of Semiconductors, vol. 34, p. 073002, 2013.

[26] S. Gedi, V. R. M. Reddy, C. Park, J. Chan-Wook, and R. R. KT, "Comprehensive optical studies on SnS layers synthesized by chemical bath deposition," Optical Materials, vol. 42, pp. 468-475, 2015.

[27] S. Nandhini and G. Muralidharan, "Facile microwave-hydrothermal synthesis of NiS nanostructures for supercapacitor applications," Applied Surface Science, vol. 449, pp. 485-491, 2018.

[28] O. O. Balayeva, A. A. Azizov, M. B. Muradov, A. M. Maharramov, G. M. Eyvazova, R. M. Alosmanov, Z. Q. Mamiyev, and Z. A. Aghamaliyev, "β-NiS and Ni3S4 nanostructures: Fabrication and characterization," Materials Research Bulletin, vol. 75, pp. 155-161, 2016.

[29] K. S. Ahmad, Z. Hussain, and S. Majid, "Synthesis, characterization and PVD assisted thin film fabrication of the nano-structured bimetallic Ni3S2/MnS2 composite," Surfaces and Interfaces, vol. 12, pp. 190-195, 2018.

[30] Y. Fazli, S. M. Pourmortazavi, I. Kohsari, and M. Sadeghpur, "Electrochemical synthesis and structure characterization of nickel sulfide nanoparticles," Materials Science in Semiconductor Processing, vol. 27, pp. 362-367, 2014.

[31] A. Ghezelbash, M. B. Sigman, and B. A. Korgel, "Solventless synthesis of nickel sulfide nanorods and triangular nanoprisms," Nano Letters, vol. 4, pp. 537-542, 2004.

[32] R. Karthikeyan, D. Thangaraju, N. Prakash, and Y. Hayakawa, "Single-step synthesis and catalytic activity of structure-controlled nickel sulfide nanoparticles," CrystEngComm, vol. 17, pp. 5431-5439, 2015.

[33] M. Kristl, B. Dojer, S. Gyergyek, and J. Kristl, "Synthesis of nickel and cobalt sulfide nanoparticles using a low cost sonochemical method," Heliyon, vol. 3, p. e00273, 2017.

[34] K. Aboulkacem, A. Abdelkader, B. Bediaf, B. Amar, K. Abdelmalek, and B. Hadj, "Thermally activated charge transport in modified tetragonal zirconia thin films prepared by sol–gel method," Japanese Journal of Applied Physics, vol. 57, p. 045801, 2018.

[35] J. Ray, M. Patel, P. Ghediya, and T. K. Chaudhuri, "Preparation and characterization of chemically deposited nickel sulphide film and its application as a potential counter electrode," Materials Research Express, vol. 3, p. 075906, 2016.

[36] J. T. Sparks and T. Komoto, "Metal-to-semiconductor transition in hexagonal NiS," Reviews of Modern Physics, vol. 40, p. 752, 1968.

[37] A. Ammari, B. Bellal, N. Zebbar, B. Benrabah, and M. Trari, "Thermal-frequency dependence study of the sub-band localized states effect in Sb-doped SnO2 based sol-gel thin films," Thin Solid Films, vol. 632, pp. 66-72, 2017.

[38] N. Makrani, A. Ammari, N. Benrekaa, D. Rodrigue, and Y. Giroux, "Dynamics of the α-relaxation during the crystallization of PLLA and the effect of thermal annealing under humid atmosphere," Polymer degradation and stability, vol. 164, pp. 90-101, 2019.

[39] O. Mahroua, B. Alili, A. Ammari, B. Bellal, D. Bradai, and M. Trari, "On the physical and semiconducting properties of the crednerite AgMnO2 prepared by sol-gel auto-ignition," Ceramics International, vol. 45, pp. 10511-10517, 2019.

[40] G. Rekhila, Y. Bessekhouad, and M. Trari, "Visible light hydrogen production on the novel ferrite NiFe2O4," International journal of hydrogen energy, vol. 38, pp. 6335-6343, 2013.
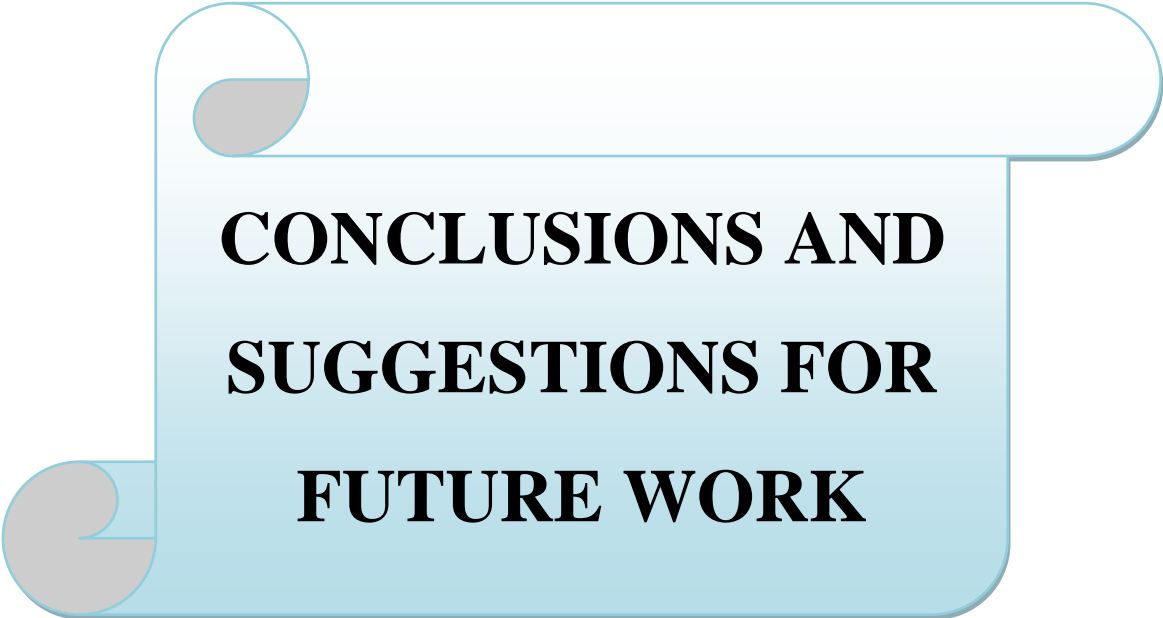
CONCLUSIONS AND SUGGESTIONS FOR FUTURE WORK

<u>Conclusions</u>

The objective of this thesis is the elaboration and characterization of nickel sulfide thin films with a simple technique, which is the spray pyrolysis technique. The work undertaken in this framework contains two parts:

In the first part of our work, we created a pyrolysis spray deposition system. The principle of deposition is based on the transport of the starting solution by means of an air jet over a hot surface at controlled temperature. This method is somewhat difficult in the deposition of this type of material due to the oxygen presence in the composition of the precipitating substance. For this reason, some researchers use nitrogen gas during the deposition process, but it is very economical because it requires only a few simple tools and produces homogeneous layers. In our deposition system, several tests have been carried out to find optimal conditions such as (air pressure, flow speed of the solution, substrate temperature, deposition time, ...etc.) for the deposition of thin layers of nickel sulphide (NiS).

In the second part of the work, we developed two series of thin-film deposits. The first one: We prepared thin layers of nickel sulphide depending on the substrate temperature 250°C, 300°C, 350°C, using, respectively thiourea ($CS(NH_2)_2$, (0.02 mol/l)) and nickel chloride ($Nicl_2$, $6H_2O$), (0.01 mol/l)) as a source of sulphur and nickel.The second one: We prepared thin layers of nickel sulphide with a nickel precursor concentration of 0.03, 0.05 and 0.07 mol/l with an S/Ni molar ratio equal to 3 at the substrate temperature of 300°C. Knowing that we have used, respectively thiourea ($CS(NH_2)_2$) and nickel nitrate ($Ni(NO_3)_2.6H_2O$) as a source of sulfur and nickel.

For each series, the thin films obtained were characterized by (DRX, Mini Flex-Rigaku) Advance using Brentano Bragg geometry (2θ) of wavelength λ_{ka} (Cu) = 1.5404 Å, with an acceleration voltage of 30 KV and a current of 40 mA for the structural properties (crystallite size, stresses, ...), for the optical characteristics of the films such as band gap, refractive index, extinction coefficient, absorption coefficient. The real and imaginary parts of the dielectric constant were calculated using an optical method from the transmittance and reflectance spectra of a Shimadzu 3101PC double-beam UV-VIS-NIR spectrometer.

The surface morphologies of the film were determined by scanning electron microscopy (SEM, Qanta 350). Energy dispersive x-ray spectrometry (EDS) was used to determine the chemical composition of the samples. The surface roughness of the films was analyzed using an atomic force microscope (AFM type SPI 3800N). The phase of the film was determined using FTIR spectrometers (FTIR; Shimadzu, model IR Affinity-1). The electrical characterization was measured by the four-tip method. The electrical measurements were recorded using the two-probe method with GW-Instek 821-LCR Meter in the temperature range of 300–380 K. For the high frequency impedance measurements, we used Agilent 4284A LCR-meter.

As for the first series results (substrate temperature effect). XRD diffraction shows that the nickel sulphide prepared at 523, 573 and 623 K has an orthorhombic and hexagonal structures, which were Ni_3S_2, $Ni_{17}S_{18}$ and NiS_2 respectively. The minimum crystallite size (45.885 nm) was measured from the deposited film at 573 K. The thin films prepared at 523 and 573 K have a good transmittance of about 20%. The Ni_1S_2 thin film has a minimum optical band gap and Urbach's energy was obtained at T=623 K. The nickel sulphide thin films have a good refractive index and extinction coefficient. The FTIR spectra of nickel sulphide have different bands such as Ni-S, C-H, O-H, N-H and C-S. The maximum electrical conductivity is $4.29x10^5$ (Ω.cm)-1 was obtained at 573 K of Ni17S18. Nickel sulphide thin films sputtered at 573 K have good structural, optical and electrical properties, and can be used as a promising co-catalyst to improve photocatalytic performance or superconductivity.

The effect of concentration: DRX results have shown that the deposited NiS thin films are single-phase or all films are composed of one phase of NiS of polycrystalline nature that have a hexagonal structure with a preferential orientation (010). It appeared that the crystallite size increased with increasing molar concentration and was about 42.7 nm for the 0.07 M concentration. In addition, the results revealed that the quality of the crystals depends on the concentration of the preparation. The optical characterization showed a band gap variation of 2.6 to 1.6 eV for a precursor concentration of 0.025 M to 0.075 M, respectively, and had a high optical absorption. The FTIR analysis conformed to the NiS thin film formation. From EDX, the atomic composition was found to increase with increasing molar concentration from 0.03 M to 0.07 M. The spherical, nano-sized

grains covering all films were confirmed by SEM analysis. The AFM images conclude that it is possible to obtain a regular, homogeneous and rough thin layer of NiS under these conditions.

Finally, we performed a NiS thin film test at 0.05 mol/l by complex impedance spectroscopy, and found that the electrical conductivity was $1.97 \times 10^{+3}$ S/cm at room temperature. The difference in conductivity temperature reveals the thermally active transport of conveyors with an activation energy of 0.026 V at (310-378 K). The interfacial capacitance is 115 $\mu F/cm^2$ at room temperature.

Suggestions for future work

NiS thin films have been deposited in MC and Ts variants on glass substrate by SPT and some of their structural, optical and electrical properties have been studied. To better understand these films, the characterization of the details is necessary. Therefore, to obtain better performance from the thin layers deposited by the spray pyrolysis technique, the following research works can be extended:

1. We want to work on thin nickel sulfide layers to deposit these layers on nickel or steel substrates by spray pyrolysis method and perform electrochemical measurements through a 3-electrode cell: the working electrode (sample), the reference electrode (Ag/AgCl (KCl)) and the reference electrode (Pt wire). The latter collects data using an electrochemical workstation (Autolab) equipped with a frequency response analyzer. We carry out periodic measurement tests in the possible range of Ag / AgCl at test rates of 5 mV s-1 to 100 mV s-1. We perform galvanostatic discharge tests with different current densities (0.25 - 1 g-1). We carry out impedance measurements in the possible frequency range with an open circuit voltage (OCP) with an AC capacitance of 10 mV. All electrochemical measurements were carried out in a KOH solution as electrolyte.

2. Characterization and analysis of the prepared sample after annealing at different temperatures,

3. Characterization and analysis of thin films prepared of more than Co doped.

4. Optimization of film growth condition like as thickness and deposition time.

5. Investigation of the magnetic properties.

6. Measurements of Hall Effect and temperature dependence of Hall Effect, etc.

ABSTRACTS

Abstract

The aim of this thesis is to prepare and characterize nickel sulfide films for application in supercapacitors. We used the spray pyrolysis technique to prepare these films because of its simplicity and low cost. In this work, we prepared two series of thin nickel sulfide films.

➢ In the first serie, chloride nickel dehydrates 10^{-2}M ($NiCl_2$, $2H_2O$), and thiourea 2.10^{-2} M ($S=C(NH_2)_2$)) were used as precursors to prepare the nickel sulfide thin films. It was obtained from two solutions with different molarities; the mixture ([S]/[Ni]=2) was stirred for 3 hours at room temperature. The nickel sulfide thin films were performed on glass substrates ($2x7$ cm^2) by spray pyrolysis method with heating at different substrate temperatures (523, 573 and 623K). The effect of deposition temperature (523, 573 and 623K) on structural, optical and electrical properties was investigated. The XRD diffraction shows that the prepared nickel sulfide at 523, 573 and 623K having an orthorhombic, hexagonal and hexagonal structure, which were Ni_3S_2, $Ni_{17}S_{18}$ and NiS_2, respectively. The minimum value of crystallite size (45,9 nm) was measured of deposited film at 573K. The thin films prepared at 523 and 573K have an average transmittance about 20 %. The prepared Ni_1S_2 thin film at T=623 K has the lowest calculated optical band gap and Urbach energy. The Ni_1S_2 thin film also has the best calculated of the refractive index and the extinction coefficient. The FTIR spectrums of the nickel sulfide have various bands such as Ni-S, C-H, O-H, N–H and C-S. The maximum electrical conductivity is $4,29x10^5$ $(\Omega.cm)^{-1}$ was obtained at 573K of the $Ni_{17}S_{18}$. The nickel sulfide thin films sprayed at 573K have good structural, optical and electrical properties.

➢ The second serie: We prepared thin layers of nickel sulfide with a nickel precursor concentration of 0.03, 0.05 and 0.07 mol/l at the substrate temperature of 300°C. We used thiourea ($CS(NH_2)_2$) and nickel nitrate ($Ni(NO_3)_2.6H_2O$) as a source of sulfur and nickel, respectively. After their elaboration, the films underwent various characterizations: structural, morphological, optical and electrical. The structural characterization shows that all the prepared thin films are poly crystalline and have a hexagonal structure according to ASTM sheet N°. 98-064-6340 with preferential

orientation on the plane (012). The crystallites size varied from 23.9 to 42.7 nm with an increase in the precursor's concentration. Furthermore, the optical bandgap decreases from 1.07 to 0.96 eV. The elementary composition analysis confirmed the presence of Ni and S elements in the samples. Both scanning electron microscopy (SEM) and atomic force microscopy (AFM), revealed a homogenous crack-free and compact appearance in all scanned areas with spherical grains. In addition, the roughness of the films significantly increases with the increase of the precursor's concentration. Finally, the film prepared with 0.05 M exhibits a high electrical conductivity and capacitance ca. 1.97×10^3 S/cm and 115 $\mu F/cm^2$, respectively, at room temperature.

The above results showed that the films prepared in this study are very attractive as an electrode material for supercapacitors application.

Key words: Nickel Sulfide, Pyrolysis Spray, Thin Films, Supercapacitors.

<u>الملخص</u>

الهدف من هذه المذكرة هو تحضير وتشخيص أغشية كبريتيد النيكل لتطبيقها في المكثفات الفائقة. استخدمنا تقنية الرش الكيميائي الحراري لتحضير هذه الطبقات بسبب بساطتها وتكلفتها المنخفضة. في بداية عملنا هذا ، قمنا بتركيب نظام ترسيب بتقنية الرش الكيميائي الحراري حيث يعتمد مبدأ الترسيب فيه على نقل محلول عن طريق نفاثة هوائية على سطح ساخن عند درجة حرارة مضبوطة. في نظام الترسيب لدينا تم إجراء العديد من الاختبارات للحصول على الظروف المثلى لترسب طبقات رقيقة لكبريتيد النيكل (الضغط، سرعة تدفق المحلول، درجة حرارة الركيزة و وقت الترسيب،....... الخ).

قمنا بإعداد سلسلتين من طبقات الرقيقة من كبريتيد النيكل بتقنية الرش الكيميائي الحراري.

➢ السلسلة الأولى: قمنا بإعداد طبقات رقيقة لكبريتيد النيكل، باستخدام الثيوريا $CS(NH_2)_2$ بتركيز 0,02 مول/ل وكلوريد النيكل ($NiCl_4.6H_2O$) بتركيز 0.01 مول/ل كمصدر للكبريت والنيكل على التوالي. تم ترسيب الأغشية الرقيقة لكبريتيد النيكل على ركائز زجاجية (2 × 7 سم^2) بتقنية الرش الكيميائي الحراري عند درجات حرارة مختلفة لركيزة الزجاجية (523، 573 و 623 كلفن). تم دراسة تأثير درجة حرارة الترسيب (523، 573 و623 كلفن) على الخواص التركيبية والبصرية والكهربائية للأفلام المحضرة. حيث يُظهر حيود الاشعة السينية XRD أن كبريتيد النيكل المحضر عند 523، 573 و 623 كلفن له بنية مختلفة ذو الاطوار Ni_3S_2، $Ni_{17}S_{18}$ و NiS_2 على الترتيب وفقًا للملف ASTM. تم الحصول للحد الأدنى لقيمة الحجم البلوري (45,9 نانومتر) للفيلم المرسب عند 573 كلفن. الأغشية الرقيقة المحضرة عند 523 و 573 كلفن لها متوسط نفاذية في حدود 20٪. يحتوي الفيلم الرقيق Ni_1S_2 المحضر عند 623 كلفن على أدنى فجوة نطاق ضوئي محسوبة وطاقة اورباخ. يحتوي الفيلم الرقيق Ni_1S_2 أيضًا على أفضل حساب من حيث معامل الانكسار ومعامل الخمود. تحتوي أطياف FTIR لكبريتيد النيكل على نطاقات مختلفة مثل Ni-S و C-H و O-H و N –H و C-S . تم الحصول على الحد الأقصى للتوصيلة الكهربائية $4.29x10^5$ S /سم عند 573 كلفن للطور $Ni_{17}S_{18}$ حيث تتمتع الأغشية الرقيقة المرسبة لكبريتيد النيكل عند درجة حرارة 573 كلفن بخصائص هيكلية وبصرية وكهربائية جيدة.

➢ السلسلة الثانية : قمنا بإعداد طبقات رقيقة من كبريتيد النيكل بتركيز مختلف لنترات النيكل 0.03، 0.05 و 0.07 مول/لتر مع تثبيت نسبة التركيز بين الكبريت والنيكل عند القيمة 3 عند كل الطبقات وتم الترسيب بطريقة الر ش الكيميائي الحراري عند درجة حرارة الركيزة 300 درجة مئوية مع العلم أننا قمنا باستخدام الثيوريا $CS(NH_2)_2$ ونترات النيكل ($Ni(NO_3)_2.6H2O$) كمصدر للكبريت والنيكل على التوالي. و بعد الانتهاء من تحضير الأغشية ، قمنا بعملية التشخيص بعدة تقنيات مختلفة : هيكلية، مورفولوجية، بصرية وكهربائية. من خلال نتائج حيود الأشعة السينية تبين أن جميع الطبقات الرقيقة المحضرة ذات تركيب متعدد التبلور ذات بنية سداسية وفقًا للملف ASTM n° 98-064-6340 مع الاتجاه المفضل للنمو هو(012). كما

أظهرت نتائج MEB & EDS أن الطبقات المحضرة مغطاة بالكامل وموحدة ومتجانسة مع فقاعات على سطح الأغشية المحضرة. وتمت دراسة الخواص البصرية من خلال تسجيل طيف النفاذية و الانعكاسية لمدى الأطوال الموجية من 300 إلى 1100 ننومتر ووجد أن الطبقات المحضرة ذات فجوة طاقة بصرية مباشرة قريبة جدا من 1 الكتروفولت بالنسبة لكل الشرائح المحضرة. كما بينت قياسات الموصلية الكهربائية للطبقات الرقيقة أن هذه الافلام المحضرة بطريقة الرش الكيميائي الحراري باستخدام ظروف التحضير المذكورة أعلاه لها موصلات جيدة حيث تتجاوز الموصلية الكهربائية 1.97 * 10^3 S/سم وقدرة سطحية في حدود 115 ميكرو فراد/سم^2 في درجة حرارة الغرفة بالنسبة للشريحة المحضرة عند تركيز 0.05 مول/لتر.

الكلمات المفتاحية: كبريتيد النيكل، الرش الكيميائي الحراري، الأغشية الرقيقة، المكثفات الفائقة.

APPENDIX

I- JCPDS card used (# 98-064-6340, 98-018-0767, 98-003-7164 and 98-016-9577).

I-1. JCPDS card #98-064-6340 used

Name and formula

Reference code:	6340-064-98
Compound name:	Nickel Sulfide
Chemical formula:	Ni_1S_1

Crystallographic parameters

Crystal system:	Hexagonal
Space group:	P 63/mmc
Space group number:	194
a (A°)	3,4200
b (A°)	3,4200
c (A°)	5,3000
Alpha (°):	90,0000
Beta (°):	90,0000
Gamma (°):	120,0000
Calculated density (g/cm^3):	5,62
Volume of cell (10^6 pm^3):	53,69
Z:	2,00
RIR:	4,82

References

Structure: Schoenberg, N ,.Acta Metallurgica(1954) ,432 - 427 ,2 ,

Peak list

I (%)	2Theta[°]	d [A]	h	k	l	N
52,1	30,149	2,96181	0	1	0	1
4,1	33,797	2,65000	2	0	0	2

38,6	34,667	2,58548	1	1	0	3
100,0	45,915	1,97490	2	1	0	4
44,6	53,547	1,71000	0	1	1	5
6,0	61,021	1,51725	3	1	0	6
4,8	62,685	1,48090	0	2	0	7
2,6	64,839	1,43683	2	1	1	8
4,8	65,378	1,42627	1	2	0	9
5,5	71,092	1,32500	4	0	0	10
19,3	73,149	1,29274	2	2	0	11
3,8	79,119	1,20949	4	1	0	12
2,3	85,489	1,13491	3	2	0	13
2,6	86,960	1,11946	0	2	1	14
4,1	89,382	1,09529	1	2	1	15

Stick Pattern
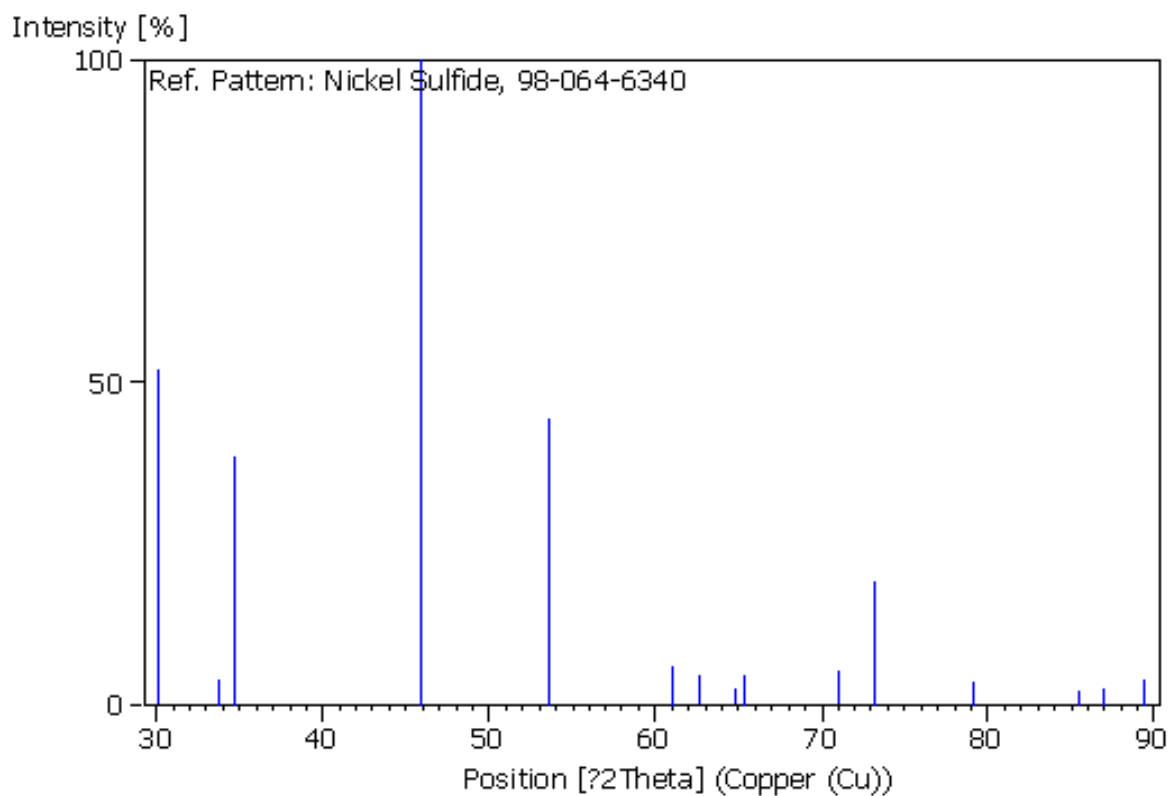
II. Some physical and chemical properties of the solutions used

1. Thiourea SC(NH₂)₂

✓ IUPAC Name: Thiocarbamide; Thiourea; Pseudothiourea; Isothiourea

✓ Appearance: White crystals.

✓ Odor : Odorless

✓ Molecular formula: $CS(NH_2)_2$

✓ Molecular weight: 76.12 g/mol

✓ Density: 1.41 g/cm^3

✓ Melting point: 175 - 177 °C

✓ Boiling point: 150 - 160 °C

✓ Solubility: No information found.

2. Nickel(II) acetate tetrahydrate

✓ Product name : Nickel(II) acetate tetrahydrate

✓ Molecular formula: $C_4H_6O_4Ni . 4 H_2O$

✓ Molar mass: 248.86 g/mol

✓ Appearance: blue-green

✓ Physical State: Solid Powder

✓ Odor: Odorless

✓ Melting point/melting range: 250 °C / 482 °F

✓ Water solubility: 182 g/L (20°C)

✓ Decomposition temperature: > 80°C

✓ Chemical Stability: Stable under normal conditions.

3. Nickel(II) nitrate hexahydrate

✓ Product name : Nickel(II) nitrate hexahydrate

✓ Molecular formula: $(Ni(NO_3)_2, 6 H_2O)$

✓ Molar mass: 290.79 g/mol

✓ Appearance: dark green

✓ Physical State: Solid Powder

✓ Odor: Odorless

✓ Relative density: 2,050 g/L at 25°C

✓ Melting Point: 140 °C

✓ Solubility: 940 g/l at 20 °C

✓ Chemical Stability: Stable under normal conditions.

4. Acetic acid CH_3COOH

✓ IUPAC ID: acetic acid

✓ Molecular formula: $C_2H_4O_2$

✓ Molar mass: 60.05 g/mol

✓ Physical state: liquid 16.64°C

✓ pKa = 4.76 at 25°C

✓ Melting T: 16.64°C

✓ Boiling point: 117.9°C

✓ Solubility: miscible with water, acetone, alcohol

✓ Dynamic viscosity : 1,22 mPa.S (at 25°C)

✓ Density: 1.0492 $g.cm^{-3}$